ARL-TR-8728 ● JUNE 2019

DEVCOM ARMY RESEARCH LABORATORY

Plasmonically Enhanced Photocatalysts for CO_2 to Fuel Applications

by Yusong Choi, Scott D Walck, Jiangtian Li, James M Sands,
Deryn D Chu, and Mark H Griep

Approved for public release; distribution is unlimited.

NOTICES

Disclaimers

ARL-TR-8728 ● JUNE 2019

Plasmonically Enhanced Photocatalysts for CO_2 to Fuel Applications

by Yusong Choi
Engineer and Scientist Exchange Program (ESEP)

Jiangtian Li
Oak Ridge Institute for Science and Education (ORISE)

Scott D Walck
Survice Engineering

Deryn D Chu
Sensors and Electron Devices Directorate, CCDC Army Research Laboratory

James M Sands and Mark H Griep
Weapons and Materials Research Directorate, CCDC Army Research Laboratory

REPORT DOCUMENTATION PAGE	*Form Approved* *OMB No. 0704-0188*

1. REPORT DATE *(DD-MM-YYYY)* June 2019	**2. REPORT TYPE** Technical Report	**3. DATES COVERED (From - To)** 6 August 2017–3 August 2018

4. TITLE AND SUBTITLE Plasmonically Enhanced Photocatalysts for CO_2 to Fuel Applications	**5a. CONTRACT NUMBER**
	5b. GRANT NUMBER
	5c. PROGRAM ELEMENT NUMBER
6. AUTHOR(S) Yusong Choi, Scott D Walck, Jiangtian Li, James M Sands, Deryn D Chu, and Mark H Griep	**5d. PROJECT NUMBER**
	5e. TASK NUMBER
	5f. WORK UNIT NUMBER
7. PERFORMING ORGANIZATION NAME(S) AND ADDRESS(ES) CCDC Army Research Laboratory ATTN: FCDD-RLW-MG Aberdeen Proving Ground, MD 21005-5066	**8. PERFORMING ORGANIZATION REPORT NUMBER** ARL-TR-8728
9. SPONSORING/MONITORING AGENCY NAME(S) AND ADDRESS(ES)	**10. SPONSOR/MONITOR'S ACRONYM(S)**
	11. SPONSOR/MONITOR'S REPORT NUMBER(S)

12. DISTRIBUTION/AVAILABILITY STATEMENT

Approved for public release; distribution is unlimited.

13. SUPPLEMENTARY NOTES

ORCID ID: Mark Griep, 0000-0001-6460-8304; Jiangtian Li, 0000-0002-4607-342X

14. ABSTRACT

The transport, logistics, and deployment of fossil fuel to the front lines has shown to be a primary target for attack, proving to be a highly hazardous job for the Warfighter and a weak link for continuing operations. As such, new technological solutions are required to reduce the Warfighter's dependence on sustained fuel delivery, either through reduced energy consumption or agile, on-site energy production. This work looks to develop light-driven catalytic materials that will facilitate the synthesis of energy-dense hydrocarbons through the solar-driven reduction of CO_2 and hydrogen evolution from water. Metal plasmonic nanomaterials are ideal candidates to simultaneously capture solar energy and couple that power to drive catalytic reactions because of their exceptionally high extinction coefficient and plasmon-energy coupling phenomena. By synthesizing catalytically active oxides onto energy-tuned metal nanoparticles, solar energy can be used to enhance select reactions. This report presents the preliminary results on the synthesis and catalytic activity of cuprous oxide nanocompositions and a multishell material consisting of a gold nanorod core with subsequent layers of reduced graphene oxide and titanium dioxide.

15. SUBJECT TERMS

CO_2 reduction, gold nanorod, plasmonics, graphene, cuprous oxide, titanium oxide, core-shell, dumbbell

16. SECURITY CLASSIFICATION OF:			**17. LIMITATION OF ABSTRACT**	**18. NUMBER OF PAGES**	**19a. NAME OF RESPONSIBLE PERSON**
					Mark H Griep
a. REPORT	**b. ABSTRACT**	**c. THIS PAGE**			**19b. TELEPHONE NUMBER (Include area code)**
Unclassified	Unclassified	Unclassified	UU	99	410-306-4953

Standard Form 298 (Rev. 8/98)
Prescribed by ANSI Std. Z39.18

Contents

List of Figures

List of Tables

Acknowledgments

This research was supported by an appointment to the US Army Combat Capabilities Development Command Army Research Laboratory administered by Exchange Scientists and Engineer Programs between the US Government and South Korea.

Dr Choi would like to deeply thank Dr Joseph P Labukas for his help and support during this research, specifically relating to electrochemical property measurement setup.

1. Introduction

The development of light-driven catalytic materials is a key enabling technology to facilitate the synthesis of energy-dense hydrocarbons through the solar-driven reduction of carbon dioxide (CO_2) and hydrogen (H_2).[1] Metal plasmonic nanomaterials are ideal candidates to harness captured solar energy to power catalytic reactions due to their exceptionally high extinction coefficient and recently discovered plasmon-energy coupling capabilities. By synthesizing catalytically active energy-tuned metal nanoparticles, solar energy can be used to enhance select reactions.[2] In this report, the preliminary results on synthesis and catalytic activity of a multishell material consisting of a gold nanorod (AuNR) core with subsequent layers of reduced graphene oxide (rGO) and titanium dioxide (TiO_2), as well as cuprous oxide (Cu_2O) nanocompositions, will be introduced

To date, a photoelectrocatalytic approach has been proposed as a green and moderate approach to efficient CO_2 resource utilization. It combines the merits of both electrocatalysis and photocatalysis, accelerates the photogenerated electrons for directional migration, and eventually improves the reduction efficiency. However, the CO_2 catalytic efficiency is still low due to the limited light absorption of semiconductors and high CO_2 activation energy. Therefore, an outstanding photoelectrocatalytic interface for CO_2 reduction must be a multifunctional integrated system in which light harvesting, photoinduced charge separation, and CO_2 activation are synergistically combined. In this work, the photoinduced charged separation is driven by a generated plasmonic field within the noble-metal (NM) core. In NM nanostructures, nonradiative decay can occur through intraband excitations within the conduction band or through interband excitations resulting from transitions between other orbital bands (for example*, d* bands) and the conduction band. In plasmonic energy conversion, electrons from occupied energy levels are excited above the Fermi energy. Hot electrons can be injected into a semiconductor by forming a Schottky barrier (Φ_B) with the plasmonic nanostructure. Hot electrons with energies high enough to overcome the Schottky barrier are injected into the conduction band E_c of the neighboring semiconductor. In plasmonic reactions the two main interactions involve improved photoreaction of the localized surface plasmon resonance (LSPR) and the activation of a lower Schottky barrier. LSPR is described as the collective oscillation of free electrons induced by incident light inside NMs. When the frequency of incident light matches the natural frequency of free electrons oscillating against the restoring force of positive nuclei, the oscillation amplitude reaches a maximum. The resonant photon wavelength is called the LSPR wavelength, which is frequency selective for different NMs and is tunable by varying the size and shape of NMs. The formation of a Schottky barrier at the NM-to-molecular oxide (MO) interface is highly dependent on the work function of the NM (Φ_M) and the electron affinity of MO (X_{SM}). Normally, the value of NM (Φ_M) is larger than that of X_{SM} (energy difference between the minimum conduction band and vacuum [V_{ac}] energy).

It is believed that a strong coupling by charge transfer and local electron fields are possible between gold nanoparticles (AuNP) and graphene. The role of graphene is to enhance electron transfer from AuNPs, driving its hydrogen evolution reaction (HER) performance. Here, we applied Cu_2O to rGO-AuNR to enhance HER performance in the near infrared (NIR) frequency, where we can expect HER performance enhancement to occur under direct exposure to sunlight. Additional reports have noted that the photocatalytic efficiency is limited by the fast recombination of the photogenerated charge carriers. To obtain long-lived charge separation, one-dimensional heterostructures have emerged as one of the ideal materials due to their quantum confinement in radial dimensions.[3] To harness these phenomena, the structure schematically represented in Fig. 1 will be developed through synthetic method and reported in this report. The enhancement over the state of the art in this structure is the development of Au-based nanorods versus the academically reported silver (Ag) molecular templates.

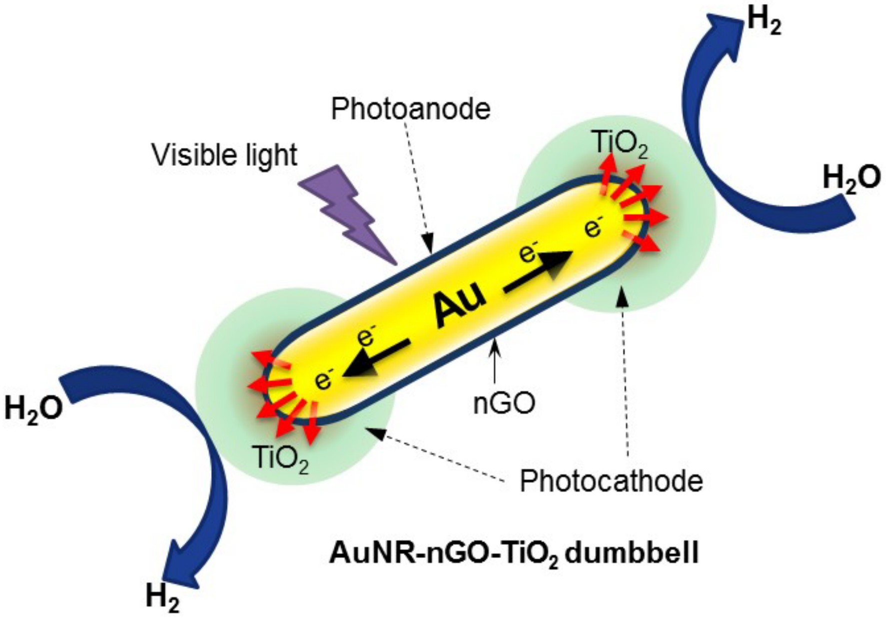

Fig. 1 Target construct for multifunctional synergistic plasmonic catalyst, where core is AuNR and surface treatments include nano-sized graphene oxide (nGO) and TiO_2 localized domains to form the site-selective dumbbell-shaped catalyst

In the case of previously reported Ag-rGO-TiO_2, there remains uncertainty regarding the photocatalytic reaction mechanism with suggestions that hot electrons are generated at TiO_2 and move to rGO and Ag.[4] However, Lang et al.[5]

reported hot electrons are generated at Ag that moved in reverse of the proposed mechanism. In the change of nanorod to Au, a mechanism for AuNR-TiO_2 yolk-shell is proposed, which aligns to Lang's reaction pathway. Hot electrons induced by light migrate from the AuNR to the TiO_2 conduction band, leaving positive charges on the AuNR core. This charge separation results in the simultaneous occurrence of oxidation and reduction reactions at different sites. Substrates (electron donor) are oxidized on the surface of AuNR cores by concentrated positive charges while electrons are consumed by the reduction of O_2 (electron acceptor) on the semiconductor surfaces.[2]

Li et al.[6] conducted an experiment to verify the transfer of electrons from the AuNR surface to the contiguous TiO_2 shell. Ag^+ (from $AgNO_3$) was used as a probe ion and sodium citrate as a positive charge scavenger. As suggested in Fig. 2, Ag particles would form on the TiO_2 shell where electrons are accumulated, indicating the flow direction of electrons. Positive charges were consumed by sodium citrate. It is apparent that Ag particles indeed only form on the TiO_2 shell and not upon the AuNR core, which supports the proposed mechanistic theory.

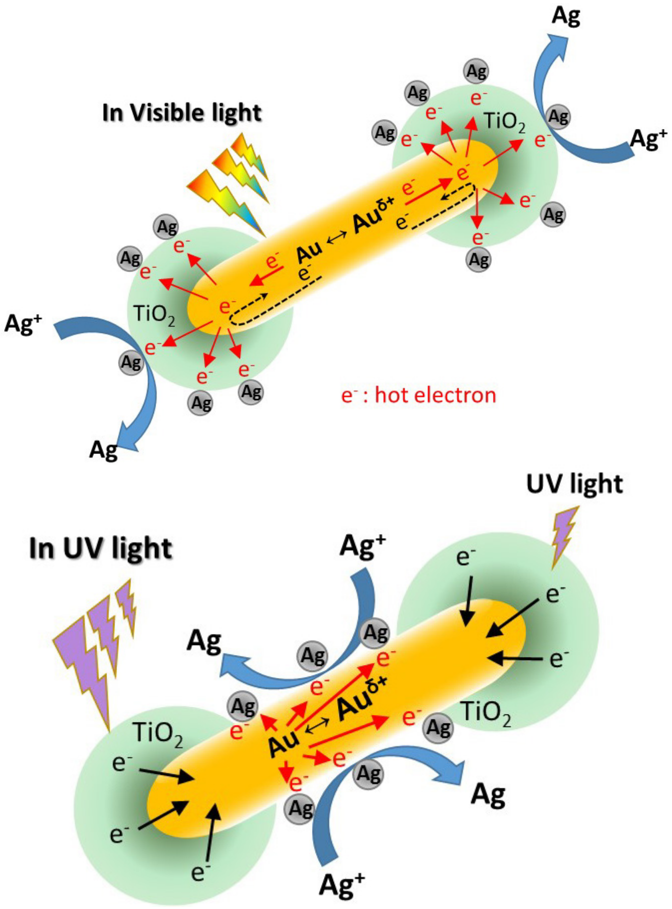

Fig. 2 Plasmonic reaction mechanism proving concept that multiple functional synergistic plasmonic catalyst excitation occurs with visible and ultraviolet light as stimuli

Si et al.[3] reported that in AuNR/TiO_2 nano-dumbbells, the dominant electron transfer direction was from TiO_2 nanoparticles to AuNRs under sunlight irradiation, and AuNR/TiO_2 nano-dumbbell photocatalysts could act as an effective photocatalyst for H_2 generation from water even without an electron donor due to the efficient charge separation and spatial separation of reduction and oxidation reaction sites.

In this report, a theoretically optimum, multifunctional, synergistic, photoelectron catalyst has been proposed as shown in Fig. 1. In this optimum catalyst, graphene (nGO) takes on the role of an efficient electron acceptor, enhances electron mobility, and protects AuNR during the catalytic reaction (especially at high temperature and in strong chemical environments). TiO_2 participates as an inexpensive robust catalyst offering high stability with its high bandgap and when it combines with graphene on an AuNR, synergistic plasmonic reactions can be accomplished. Although AuNRs are well-known plasmonic catalysts in visible light, they are unstable in the photocatalytic reaction. When we make AuNR a component of a dumbbell structure, we can extract the best combination of the components while minimizing drawbacks and increasing catalytic efficiency (by separating oxidation and reduction). For comparison study, we created a model complex with AuNR-nGO-TiO_2 core-shell as shown in Fig. 3. Here, the layered structure of the assembled AuNR creates path restrictions for the electrochemistry and the light-activated processes. The plasmonic particles are developed with a strategic goal and system performance in mind.

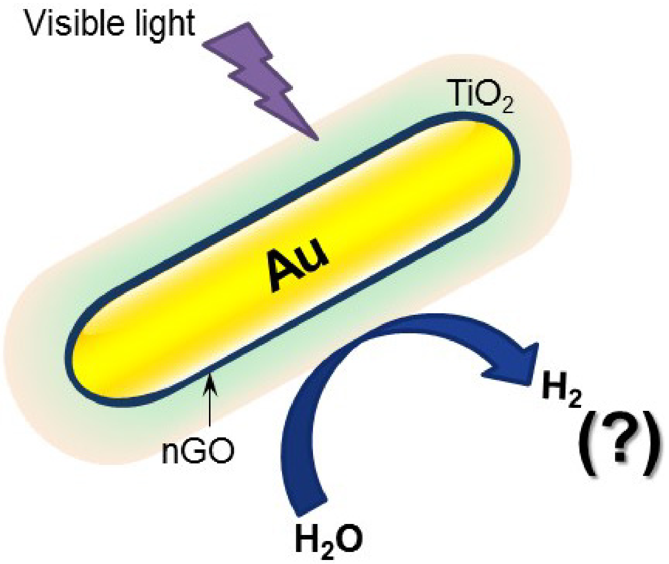

Fig. 3 **AuNR-nGO-TiO_2 core-shell**

2. Experimental Procedure

2.1 Materials

All chemicals were purchased from Sigma-Aldrich (St. Louis, Missouri) and solutions prepared were aqueous, unless otherwise noted:

- Cetyltrimethylammonium bromide (CTAB)
- Sodium hydroxide (NaOH)
- Methanol
- Ethanol
- Isopropanol
- Ammonium hydroxide
- Chloroauric acid ($HAuCl_4$)
- Millipore (18 ohms) water
- Sodium oleate (NaOL)
- Nafion
- Dimethyl formamide (DMF)
- Distilled deionized water (DDI)
- Sulfuric acid
- Hydrochloric acid
- Hexadecyltrimethylammonium bromide ($C_{16}TAB$)
- Sodium borohydride ($NaBH_4$)
- Hydrogen tetrachloroaurate trihydrate ($HAuCl_4 \cdot 3H_2O$)
- Sodium dodecyl sulfate (SDS)
- Titanium trichloride ($TiCl_3$) (15% with 5%–10% excess HCl)
- Silver nitrate ($AgNO_3$)
- L-ascorbic acid (AA)
- Sodium bicarbonate ($NaHCO_3$)

- Hydrochloric acid (HCl)
- Cysteamine (CYS)

2.2 Synthesis

There are four primary methods for precisely tailored AuNR synthesis. These include the template, electrochemical, seed mediation (with silver particles, Ag), and photochemical synthesis methodologies. The amount of Ag ions present during the electrochemical method of synthesizing AuNR controls the aspect ratio of AuNR. Silver ions under-potential deposition on the side [110] facets slows the growth in that direction and promotes the elongation of rods on their tips. Symmetry breaking is induced by the preferential adsorption of CTA^+-$[Br\text{-}Ag\text{-}Br]^-$ ionic complex on the [100] facet of the Au crystal. Silver ions were combined with CTAB and undergo under-potential deposition on either [100] or [110] facets and thus promote anisotropic growth. The presence of Ag also slows the growth process with the aforementioned benefit of a higher AuNR yield and enhances monodispersity. The reduction of the seeds was undertaken exclusively by $NaBH_4$ to ensure quick and complete reduction of $HAuCl_4$ to Au^0, although they can be capped by sodium citrate or CTAB to produce penta-twinned or single-crystal rods, respectively.

2.2.1 AuNR with CTAB

The synthesis of AuNRs via the CTAB approach has been widely published.[7,8] The initial step in preparing AuNRs was to synthesize the Au seed material. First, 0.01 M $NaBH_4$ prepared in 0.01-M NaOH, which after vortexing was cooled to near 0 °C prior to use. A volume of 100 µL of 50 mM $HAuCl_4$ was mixed with 9.9 mL of 0.1-M CTAB and held at 29 °C to keep the CTAB solubilized. With rapid stirring an addition of 0.46 mL of ice cold 0.01-M $NaBH_4$ was inserted dropwise until the solution color changed from light yellow to light brown. The solution was stirred for approximately 30 to 60 s then aged approximately 1 to 4 h to allow the sodium borohydride to completely react.

The AuNR growth step requires the preparation of 0.1 mL of 50-mM $HAuCl_4$ solution added to 9.9 mL 0.1-M CTAB, followed by brief vortexing. To this solution, a total of 40 µL of 0.1-M $AgNO_3$ was added, followed by the addition of 1.0 mL of 0.1-M hydroquinone (HQ). The solution was gently agitated by hand until it became transparent. Finally, a select amount of the prepared Au seed (i.e., 160 µL) was added to solution followed by 10 s of vortexing. The solution was stored at 29 °C in a water bath for 24 h to complete material growth.

2.2.2 AuNR with NaOL

Utilizing the same procedure to prepare Au seeds as outlined in Section 2.2.1, this method deviates at the AuNR growth stage.[9] Stock solution of surfactant was prepared by adding 9.0 g of $C_{16}TAB$ and 1.234 g NaOL into 250 mL DDI at 90 °C with vigorous stirring. The solution was cooled to room temperature before use. A volume of 20 mL of surfactant solution is mixed with 20 mL of DDI and 0.4 mL of 50 mM $HAuCl_4$. After thorough mixing, the solution was kept in a 30 °C water bath for 90 min. Concentrated 156-µL HCl solution (36.5%–38%) was then added to the solution to adjust the solution to an acidic pH level. After 15 min, 0.064 mL of 0.1 M ascorbic acid was injected into the solution, followed by vortexing for 30 s. Then a volume of 0.0768 mL of 0.1-M $AgNO_3$ solution and a select amount of Au seed (i.e., 16 µL) was added to the growth solution. The solution was shaken for 30 s and then left undisturbed in the 30 °C water bath for 12 h. The final product was separated by centrifuging at 8000 rpm for 20 min followed by dispersion and the second centrifuge with 5500 rpm for 20 min. Finally, the AuNRs were dispersed into 10 mL of H_2O as the stock solution.

2.2.3 Massive Synthesis of AuNR with CTAB

This section describes the synthesis of AuNR with CTAB by Lark et al.[10] The scaled up synthesis protocol again requires the same Au seed preparation as described in Section 2.2.1. Scaling of the nanorod growth step was achieved by adding CTAB (364 mg) and HQ (110 mg) to DDI according to the growth ratio as shown in Table 1.

Table 1 Scale-up amount of each reactant for massive AuNR synthesis

Sample	0.1 M AA (µL)	0.1 M HQ (µL)	0.1 M $HAuCl_4$ (µL)	0.1 M $AgNO_3$ (µL)	Au seed to AA (µL)	Au seed to HQ (µL)	DI water volume (mL)
1S1G AA	26.5	. . .	25	8	10	. . .	9.93
25S25G AA	663	. . .	. . .	200	250	. . .	8.262
100S100G AA	2,650	. . .	2,500	800	1,000	. . .	3.05
1S1G HQ	. . .	50	25	8	. . .	10	9.907
25S25G HQ	. . .	1,250	625	200	. . .	250	7.675
100S100G HQ	. . .	5,000	2,500	800	. . .	1,000	0.7

2.2.4 Nano-Sized Graphene Oxide (nGO)

To synthesis nGO, four distinct methodologies were employed. The four methodologies are distinguished by the starting carbon material, which include 1) graphite flakes, 2) micron-sized graphene oxide, 3) nGO, and 4) graphene quantum dots (GQDs).

The first method involves adding H_2SO_4/H_3PO_4 (360:40 mL) (9:1) directly to a mixture of graphite flakes (3.0 g, 1 wt% equiv.). $KMnO_4$ (18.0 g, 6 wt% equiv.) was then slowly added into the reaction mixture with stirring and cooling in an ice water bath.[11,12] The sample was then heated to 50 °C and stirred for 12 h. Finally, the reaction mixture was cooled to room temperature and poured onto ice water (400 mL) containing 3 mL 30% H_2O_2. The final solution was then filtered through a metal US standard testing sieve (W.S. Tyler, 300 μm) to remove larger aggregates and then further purified by centrifugation at 8000 rpm for 30 min, with the pellet collected and the supernatant decanted off. The remaining material was then washed in succession with 200 mL of water, 200 mL of 30% HCL, 200 mL of ethanol and water again until solution pH reached approximately 5.0–6.0. The resulting suspension was filtered with polytetrafluoroethylene membrane with a 0.45-μm pore size and then lyophilized to produce a graphene oxide powder. The graphene oxide powder (5.0 mg) was dissolved in triple distilled water (>18 MΩ, 10 mL) and then exfoliated by prolong sonication (35% amplitude, 500 W, 2 h) until the entire size distribution was below 150 nm, then centrifuged (18,000 rpm, 20 min) to remove precipitates (un-exfoliated large graphene oxide sheets).

The second method, an oxidation method, starts with 20-μm flake-size graphene oxide powder.[13] The prepared graphene oxide (0.05 g) was put into a concentrated H_2SO_4 solution (50 mL), followed by a select amount of $KMnO_4$ (0.05–0.15 g) being slowly added to the prepared solution with vigorous stirring to produce nGO. The resulting mixture was cooled down in an ice bath and 100 mL of H_2O_2 solution (95 mL of water + 5 mL of 30 wt% H_2O_2) was then added very slowly and stirred over 1 h. The resultant mixture solution was ultrasonicated for 30 min to obtain exfoliated final single-layer graphene oxide (SLGO) product.

Combined with the oxidation method, the third method adds an additional sonication step to mechanically reduce the nGO lateral dimensions to the submicron scale. Utilizing SLGO solutions prepared in DDI at 0.5 mg/mL, the materials were probe sonicated at an amplitude of 70% for 1 h in an ice-cooled bath. The treated samples were centrifuged at 10,000 rpm for 1 h, with the supernatant collected for further use. The probe sonication step was explored at multiple sonication power levels and durations, ranging from 50 to 90 W for 3 to 12 h, respectively.

The fourth method utilizes a version of nGO more specifically identified as GQD, where the oxidized graphene oxide was dissolved in DMF to a concentration of 10 mg/mL. The solution was dispersed via ultrasonication for 10 min and then transferred to a Teflon-lined autoclave vessel for hydrothermal treatment at 200 °C for 7 h.[14] The treated samples were centrifuged at 10,000 rpm for 1 h, with the supernatant collected for further use.

2.2.5 Hollow Porous Cu_2O Microsphere

To create the Cu_2O microspheres, 180 mg of SDS is dissolved in 45 mL of DDI and stirred for 20 min. Once fully dissolved, 1 mL of 0.1-M copper(II) chloride ($CuCl_2$) was added, followed by 0.04 mL of 29.5% ammonia. The solution is mixed via vortexing and 0.15 mL of 5-M NaOH was added. After fully stirring, 0.18 mL of $N_2H_4H_2O$ (50 wt%) was added dropwise under constant stirring at 20 °C, followed by continued stirring for 40 min. The solution was purified by centrifugation at 10,000 rpm for 20 min and rinsed with DDI three times with the final pellet resuspended with ethanol.

2.2.6 AuNR-Cu_2O Dumbbells

Cu_2O dumbbell structures, as shown in Fig. 4, were created on AuNRs by first diluting 1 mL of AuNR stock solution with 1.8 mL of H_2O. The solution was then purified of excess CTAB by centrifuging at 12,000 rpm for 10 min. The 2.75 mL of supernatant was extracted and the sedimentary AuNR was redispersed into H_2O to 1 mL for subsequent use. A 1-mL volume of 0.1-M $CuCl_2$ was added to 45 mL of DDI with stirring, followed by the addition of 0.75 mL 0.1-M NaOH with continued stirring. Then 0.18 mL of $N_2H_4H_2O$, (50 wt%) was added dropwise to the prepared solution under stirring and the AuNR solution was immediately injected. The solution was stirred at room temperature for 40 min and purified by centrifugations at 10,000 rpm for 20 min and rinsed with DDI three times. The final pellet was resuspended in ethanol.

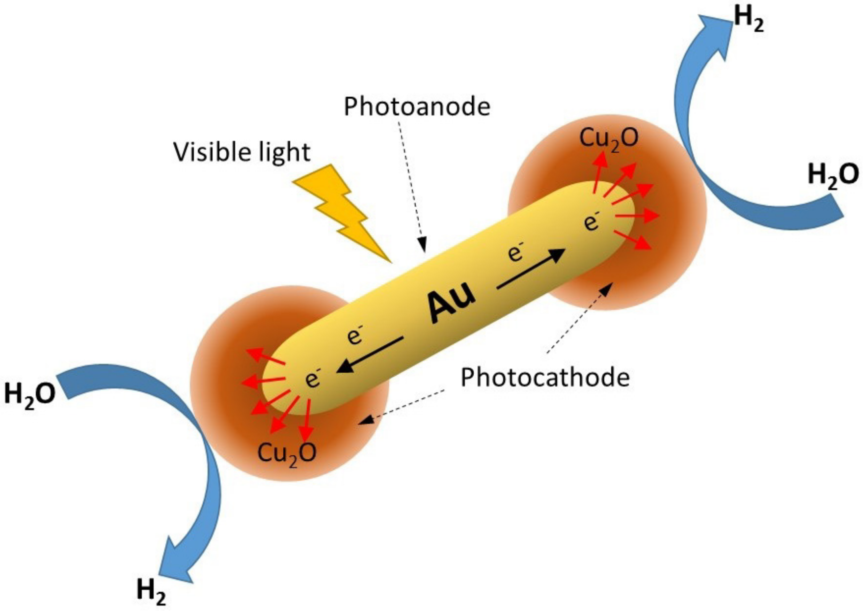

Fig. 4 AuNR-Cu_2O dumbbell

2.2.7 AuNR-TiO_2 Dumbbells (Yuelei Si's Method[3])

Titanium dioxide dumbbells, as shown in Fig. 5 were created on AuNR cores. A volume of 200 μL of AuNR stock solution was diluted with 1.8 mL of H_2O and separated by centrifuging at 12,000 rpm for 10 min. The AuNR pellet was redispersed into H_2O to 1 mL for subsequent use. The reaction solution was created with 100 μL of 15%–20% $TiCl_3$ added to 4 mL of H_2O. Subsequently, 500 μL of $NaHCO_3$ solution (1 M) was added into the $TiCl_3$ solution dropwise under stirring and the AuNR solution was immediately injected. The mixture solution was then stirred for 30 min at room temperature. The prepared Au/TiO_2 nano-dumbbells were washed twice in ethanol and redispersed in ethanol for later use.

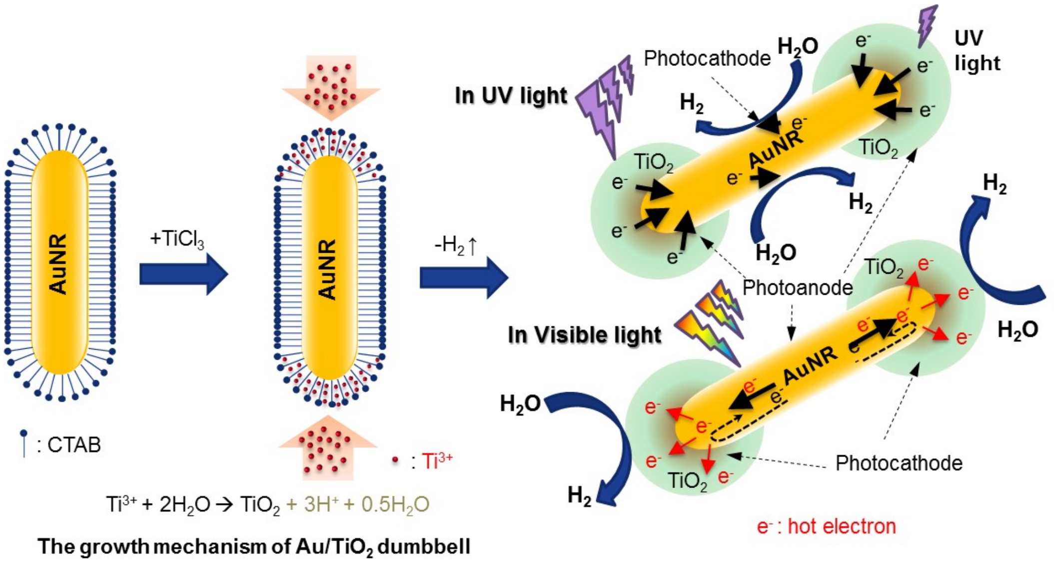

Fig. 5 Growth mechanism of Au/TiO_2 dumbbell

2.2.8 AuNR-TiO_2 Dumbbells (Binghui Wu's Method[9])

A separate methodology to grow TiO_2 dumbbell coating on AuNR cores, as shown in Fig. 6, was achieved by diluting 0.2 mL of (>12%) $TiCl_3$ with 4 mL degassed H_2O in a 10-mL centrifuge tube. A volume of 0.72 mL of 1-M $NaHCO_3$ was added to the solution dropwise under stirring (before the addition of the last two or three drops of bicarbonate, the solution turns into a dark blue solution with a pH of about 2.5).

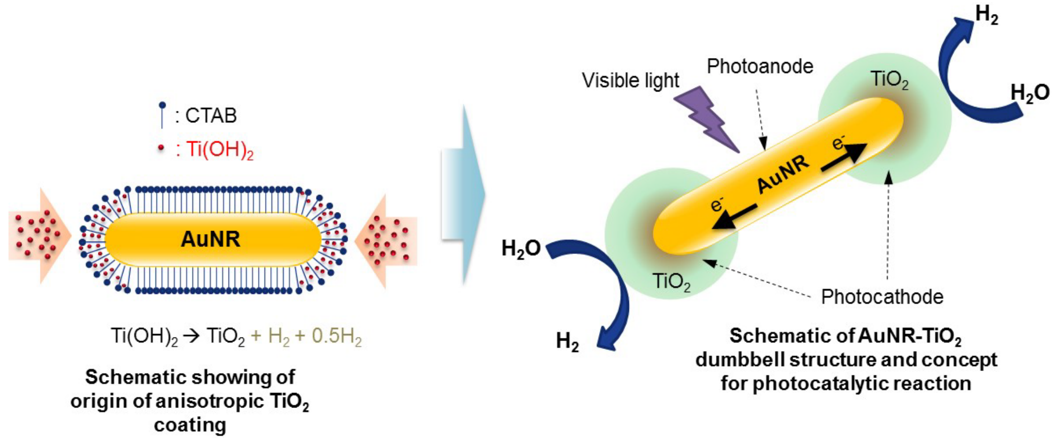

Fig. 6 Schematics showing the origin of anisotropic TiO_2 coating to synthesis of AuNR-TiO_2 dumbbell

A mixture (0.5 mL of AuNR stock solution + 0.5 mL 0.1-M $C_{16}TAB$ solution + 1.3 mL DDI) was added into the prepared solution and was then gently kept stirring/shaking for 60 min. In this step, five different CTAB concentrations of samples have been prepared: 6.93, 12.95, 27.11, 49.17, and 83.76 mM. The solution is centrifuged at 6,000 rpm for 10 min and washed with ethanol twice (most the surfactant CTAB and unreacted Ti^{3+} precursors can be washed away in this step).

2.2.9 AuNR-TiO_2 Core-Shells

To create core-shell structures, as shown in Fig. 7, a volume of 0.2 mL of 15% $TiCl_3$ was diluted with 4 mL of degassed H_2O in a 10-mL centrifuge tube. Following this, 0.72 mL of 1-M $NaHCO_3$ was added to the solution dropwise under stirring (before the addition of last two or three drops of bicarbonate, the solution turns into a dark blue solution, with a pH of about 2.5). The amorphous TiO_2 sample was prepared by reacting the $TiCl_3$-$NaHCO_3$ solution without metal nanoparticles at room temperature for 2 h. When fully reacted, 0.5 mL of AuNR went through an SDS exchange and was then dispersed into the solution for TiO_2 coating and stirred for 60 min. The final solution was centrifuged at 6,000 rpm for 10 min and washed with ethanol twice to remove excess CTAB and unreacted Ti^{3+} precursors.

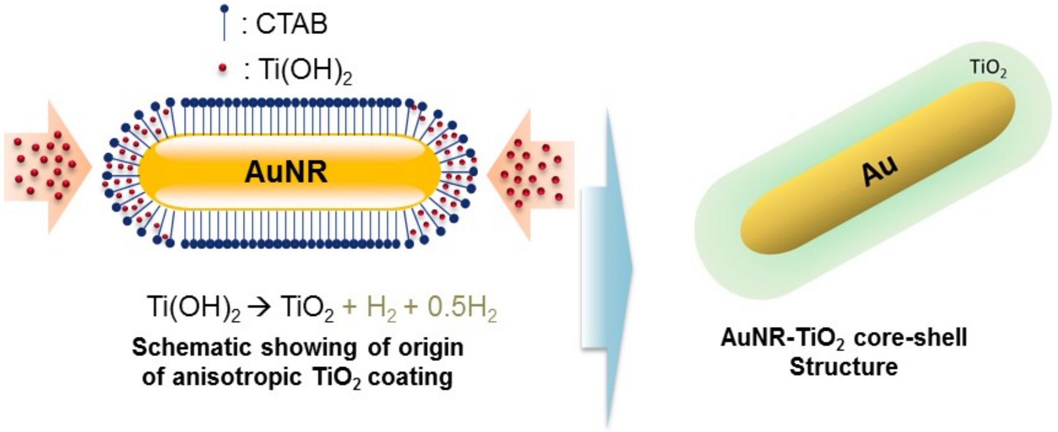

Fig. 7 Origin of anisotropic TiO_2 coating to synthesis of AuNR-TiO_2 core-shell

2.2.10 AuNP-rGO-Cu_2O with CTAB

The integration of a graphene spacer layer in these structures, as shown in Fig. 8, could provide enhanced electron transfer/mobility. To integrate the graphene layer, the following procedure was employed. A 10-mL volume of citrate-capped AuNP solution (optical density [OD] = 1.0 at 800 nm) was slowly added into a large excess of negatively charged nGO solution (0.5 mg/mL, 20 mL) and gently vortexed for 1 h. Following incubation, the hybrid materials were collected by centrifugation (at 4000 rpm for 15 min, 2 times) and the final purified pellet dispersed in 10 mL of DDI. The pH of the graphene oxide–coated AuNP solution was adjusted between 10.0 and 11.0 using trace amounts of ammonium hydroxide solution (28%, w/w).

The reduction of graphene oxide to rGO was then achieved with the rapid addition of hydrazine monohydrate (50 µL) to the solution. The reaction mixtures were allowed to stir for 1 h at 95 °C and then cooled, centrifuged, and dispersed in DDI. The Cu_2O coating was achieved using the coating methodology described in Section 2.2.6.

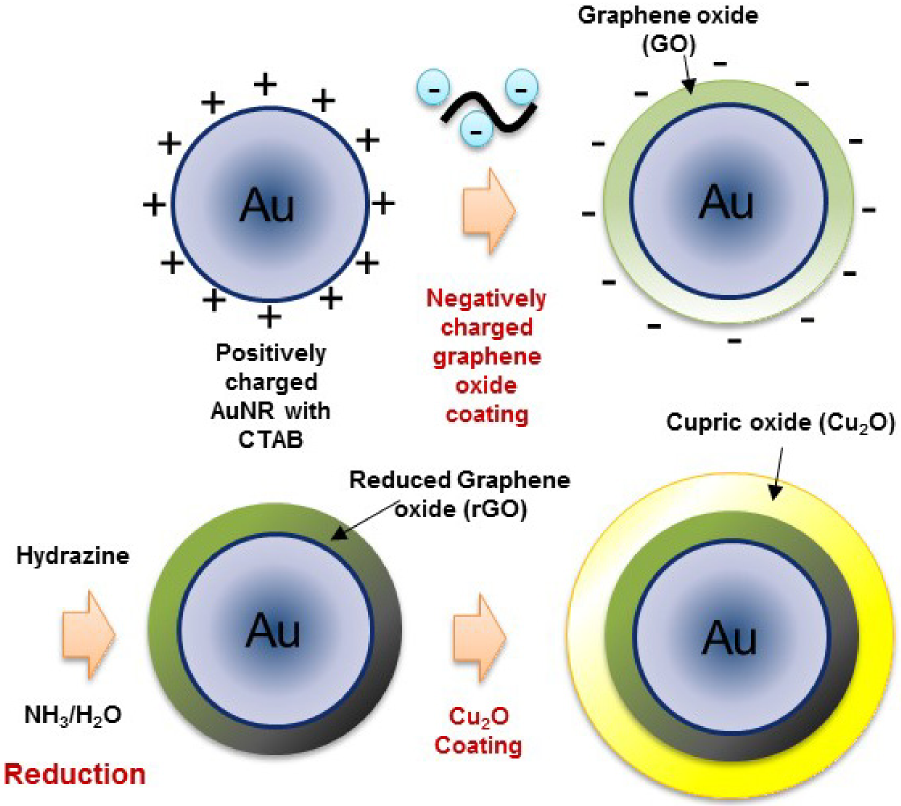

Fig. 8 Synthesis process of AuNP-rGO-Cu_2O with CTAB

2.2.11 AuNR-rGO-Cu_2O with CTAB

Apart from traditional AuNP cores, the graphene oxide layer can be integrated onto nanorod cores as well, as schematically shown in Fig. 9. A 10-mL volume of CTAB-stabilized AuNR solution (OD = 1.0 at 800 nm) was slowly added into a large excess of negatively charged nGO solution (0.5 mg/mL, 20 mL) and gently vortexed for 1 h. Following incubation, the hybrid materials were collected by centrifugation (4000 rpm, 15 min, 2 times) and the final purified pellet dispersed in 10 mL of DDI. The pH of the graphene oxide–coated AuNR solution was adjusted between 10.0 and 11.0 using trace amounts of ammonium hydroxide solution (28%, w/w). The reduction of graphene oxide to rGO was then achieved with the rapid addition of hydrazine monohydrate (50 µL) to the solution. The reaction mixtures were allowed to stir for 1 h at 95 °C and then cooled, centrifuged, and dispersed in DDI. The Cu_2O coating was achieved using the coating methodology described in Section 2.2.6.

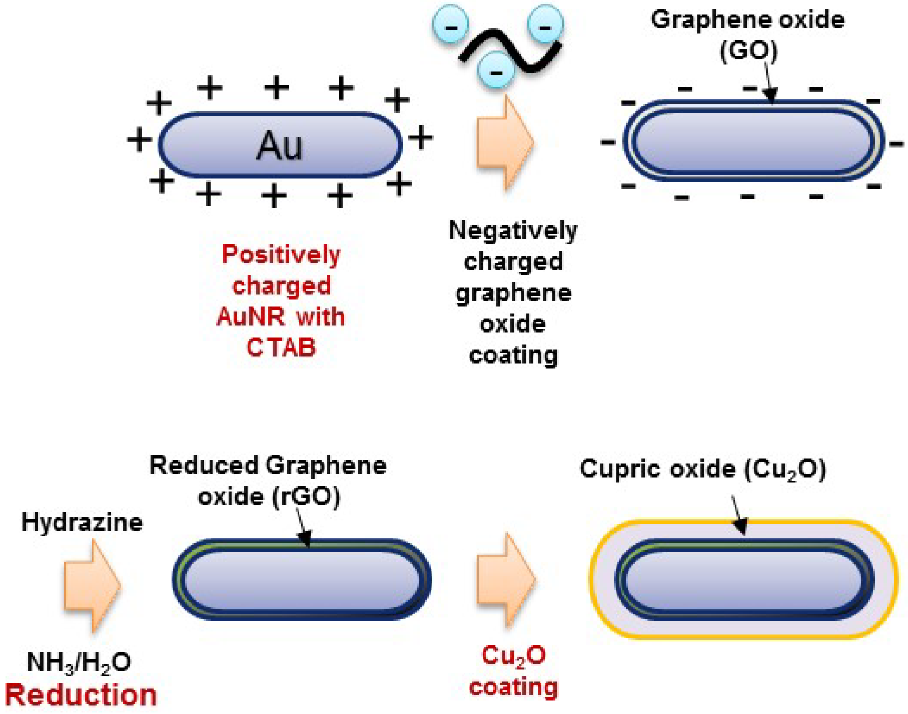

Fig. 9 Synthesis process of AuNR-rGO-Cu_2O with CTAB

To enhance the electrostatic binding between graphene oxide and AuNRs, a stronger positively charged coating was also added to the AuNR surface. The increased positive charge was achieved through the addition of polystyrene sulfonate (PSS) to the AuNR, as shown in Fig. 10. A 10 mg/mL solution of PSS solution was prepared and added in excess to the AuNR stock solution (1-mM CTAB) and allowed to incubate for 10 min, followed by centrifugal purification.

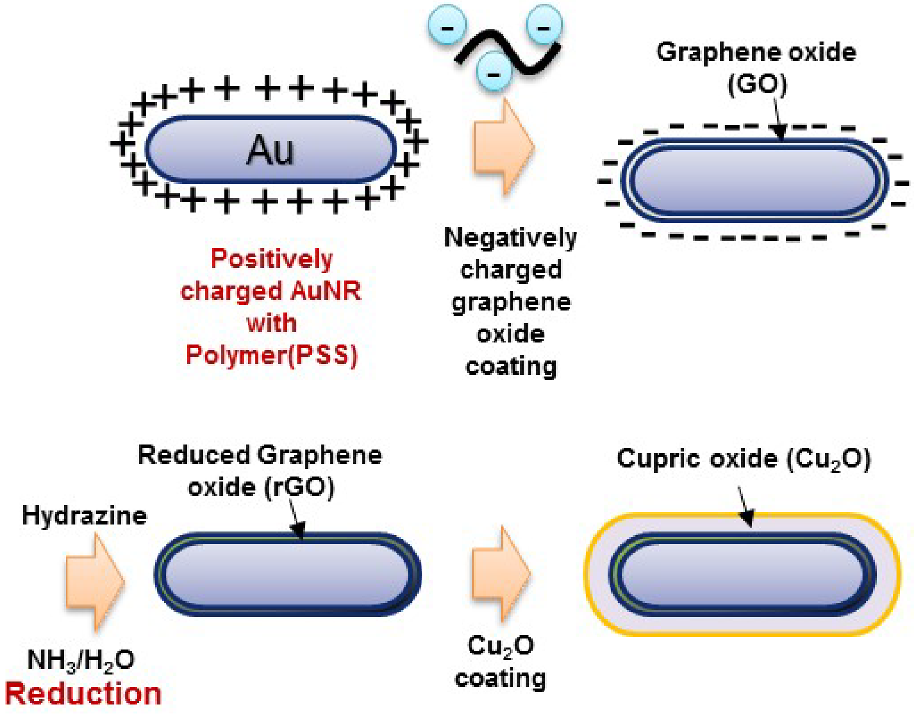

Fig. 10 Synthesis process of AuNR-rGO-Cu_2O with PSS

2.3 Characterization

2.3.1 Transmission Electron Microscopy (TEM)/Scanning Transmission Electron Microscopy (STEM)

To prepare TEM samples, the AuNRs were dispersed in ethanol and carefully deposited on top of TEM grids (Holey carbon support film on Cu grid). As the ethanol evaporated, the AuNRs were able to self-assemble on the surface of the support film. Bright field (BF)-TEM images were acquired with a JEOL 2100F field emission TEM/STEM at 200 keV. The JEOL 2100F TEM/STEM is equipped with an EDAX Octane Elite 30 windowless X-ray microanalysis system, a Gatan model 806 high-angle annular dark field detector (HAADF), and a Gatan Tridiem electron energy loss spectrometer and imaging filter.

2.3.2 UV-Vis

The absorption spectra for AuNRs were obtained on a UV/Vis/NIR (Perkin-Elmer, Lambda 1050, Waltham, MA) spectrometer in the optical region of 300–1200 nm with a path length of 1 cm. The UV-Vis was equipped with a 3-D WB detection module.

2.3.3 Atomic Force Microscopy (AFM)

AFM of Asylum Research (Cypher Scanning Probe Microscope) was used to measure the size change of graphene oxide after sonication. AFM measurement was conducted in tapping mode, with a scan rate of 1.5 Hz and set point of 700 mV. The AFM sample was prepared by drop-casting the nanoparticle solution on silicon (Si) wafers that were rinsed twice with ethanol, isopropyl alcohol, and deionized water followed by drying under N_2 gas.

2.3.4 Scanning Electron Microscopy (SEM)

SEM samples were prepared by drop-casting the nanoparticle solution onto Si wafers that were rinsed twice with ethanol, isopropyl alcohol, and deionized water followed by drying under N_2 gas. The solvent was allowed to completely evaporate and the samples were analyzed using a Hitachi S-4700 Field Emission SEM.

2.3.5 Electrochemical Property

The prepared nanoparticles (Au/TiO_2) in ethanol were condensed by centrifugation and coated on an indium tin oxide (ITO) substrate (as-prepared samples as the working electrodes with an active area of approximately 2.5 cm^{-2}). The electrode was dried in air at 60 °C for 2 h. A standard three-electrode electrochemical cell was assembled using Ag/AgCl electrode and platinum (Pt) wire as reference and counter electrodes, respectively, as illustrated in Fig. 11. An aqueous solution of 0.5-M Na_2SO_4 was used as an electrolyte, and the cell was irradiated using UV (Lumen Dynamics Omnicure LX400+) and solar simulating (Newport 69907) lamps. Linear sweeps and current versus time (I-t) scans were measured at zero bias voltage by a Biologics electrochemical workstation.

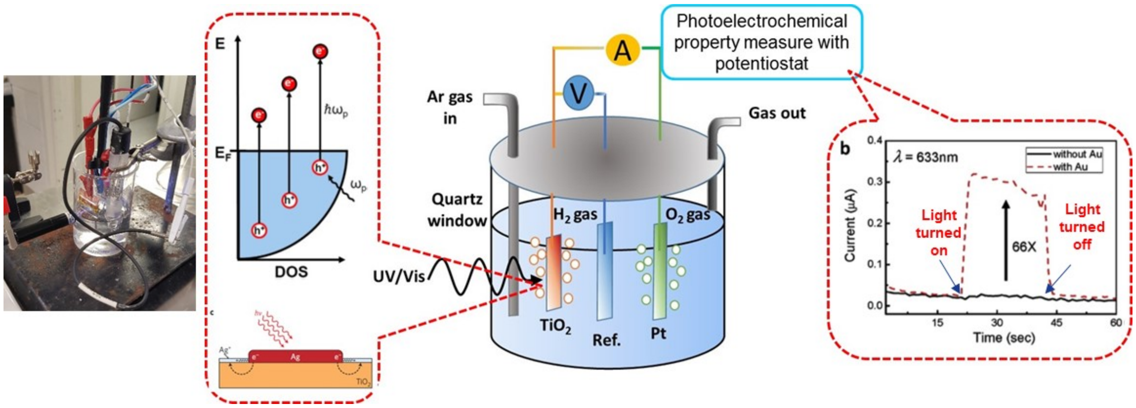

Fig. 11 Photocurrent (photoelectrochemical) measurements

Oxidation and reduction mechanism probe experiments were performed by preparing 1 mL of AuNR-TiO_2 dumbbell solution in a 50-mL centrifuge. To this solution, 10 mL of 0.026 M $AgNO_3$ and 200 mg of sodium citrate was added. After 30 min of stirring, the mixture was irradiated by a UV lamp for 1 min, followed by centrifugal washing to purify the sample.

HER experiments were performed with a three-electrode measurement method as depicted in Fig. 12. A Pt wire was used as a counter electrode and Ag/AgCl as a reference electrode with samples prepared on a glassy carbon electrode to serve as the working electrode. A 10-mg sample was dispersed using a bath sonicator in 1-mL water–ethanol (1:1 v/v) solution containing 25 μL of Nafion solution (5 wt%), with 10 μL of the dispersed solution drop-cast on the glassy carbon electrode and dried before electrochemical testing. All the electrochemical measurements were conducted in an N_2-saturated 0.5-M H_2SO_4 electrolyte at room temperature. Electrochemical impedance spectroscopy studies were performed in a frequency range of 0.05 Hz–10 kHz with an applied 10 mV of AC amplitude for all measurements

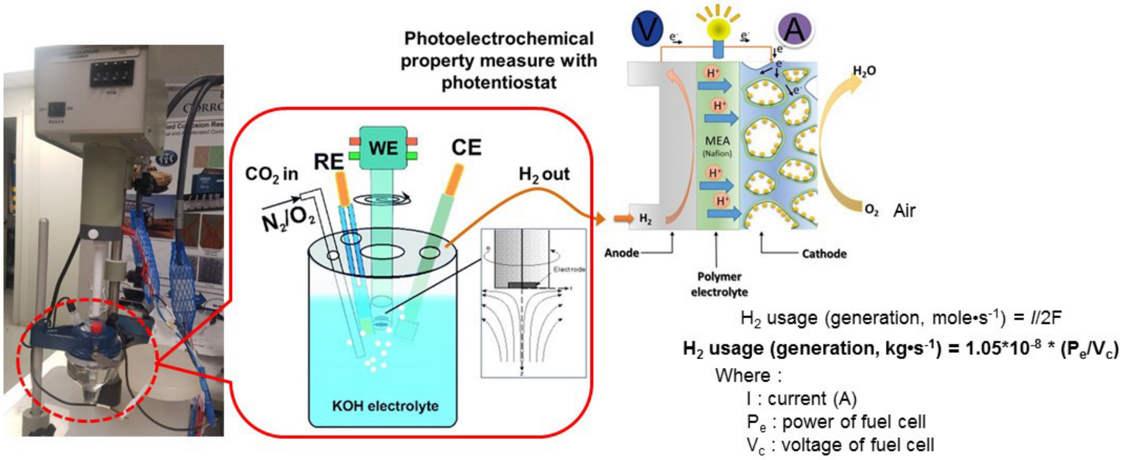

Fig. 12 HER measurement setup and mechanism

3. Results

3.1 AuNR

The UV-Vis spectrum for AuNR is presented in Fig. 13 showing two primary absorption peaks located at 530 and 617 nm, which correspond to transverse surface plasmon resonance (TSPR) and LSPR peaks, respectively.

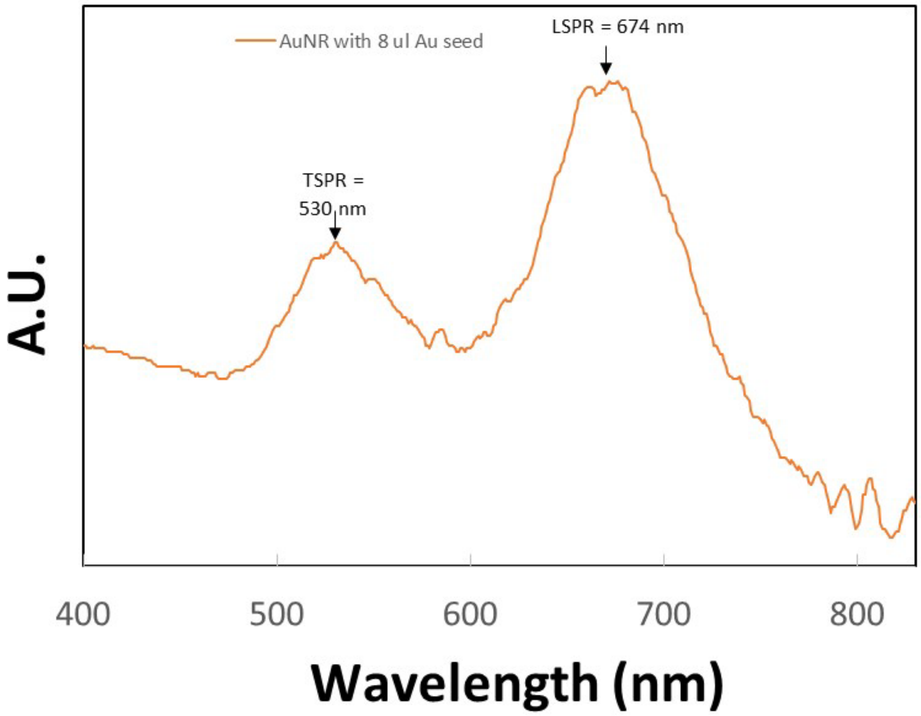

Fig. 13 UV-Vis spectrum for synthesized AuNRs with NaOL using 8-µL Au seed during the seed-mediated synthesis method

The theoretical aspect ratio (based on results from optical analysis) was obtained by projecting the experimental λ_{LSPR} into an equation derived from literature[15,16] (λ_{LSPR} vs. AR; Eq.1):

$$AR = 0.0092(\lambda_{LSPR}) - 3.41\ . \qquad (1)$$

The theoretical aspect ratio obtained using Eq. 1 is 2.73. Compared with the real aspect ratio obtained from BF-TEM image in Fig. 14, the real aspect ratio of AuNR was 2.72. Both agreed well with theoretical calculations. The average diameter of the synthesized AuNR was 9.95 nm.

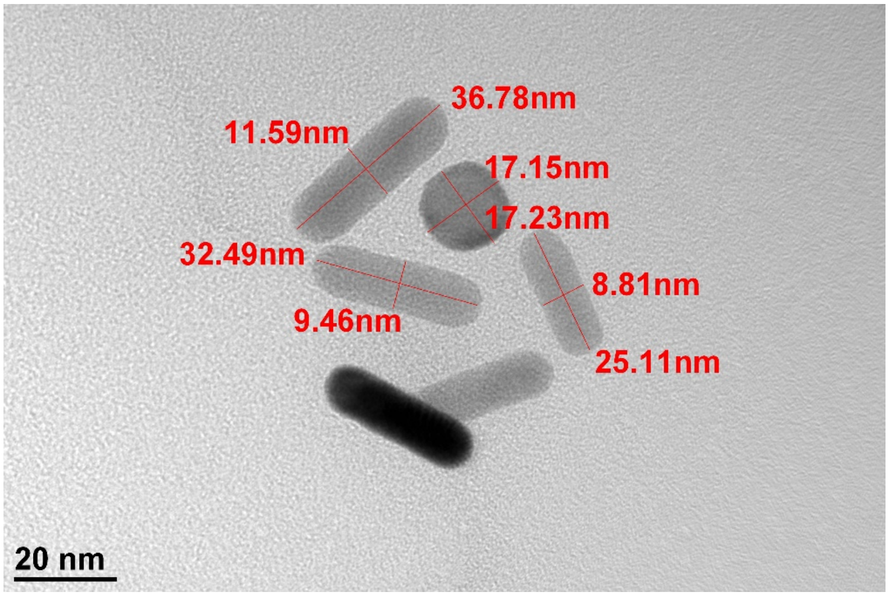

Fig. 14 BF-TEM image of synthesized AuNRs with CTAB using 160-µL Au seed during the seed-mediated synthesis method

After decreasing the amount of Au seed during the synthesis of AuNR with CTAB from 160 to 80 µL, UV-Vis spectra were measured after synthesis. Adjusting the Au-seed volume was the only variation to the experimental procedure; all other values remained constant. The UV-Vis spectrum is shown in Fig. 15. LSPR is red shifted to 771 nm after decreasing the amount of Au-seed. From UV-Vis measurements, it was found that that decreasing the Au seed causes the LSPR to be red shifted. The SEM image of AuNR with CTAB using 80 µL of Au seed is shown Fig. 16. Note the sharp edges at the ends of AuNR, as opposed to the typical rounded end structures compared to other samples. The shape of AuNR is rather rectangular than capsule-like form, as further highlighted by TEM images in Fig. 17. The diameter of AuNR with CTAB using 80-µL Au seed averages 24.21 nm.

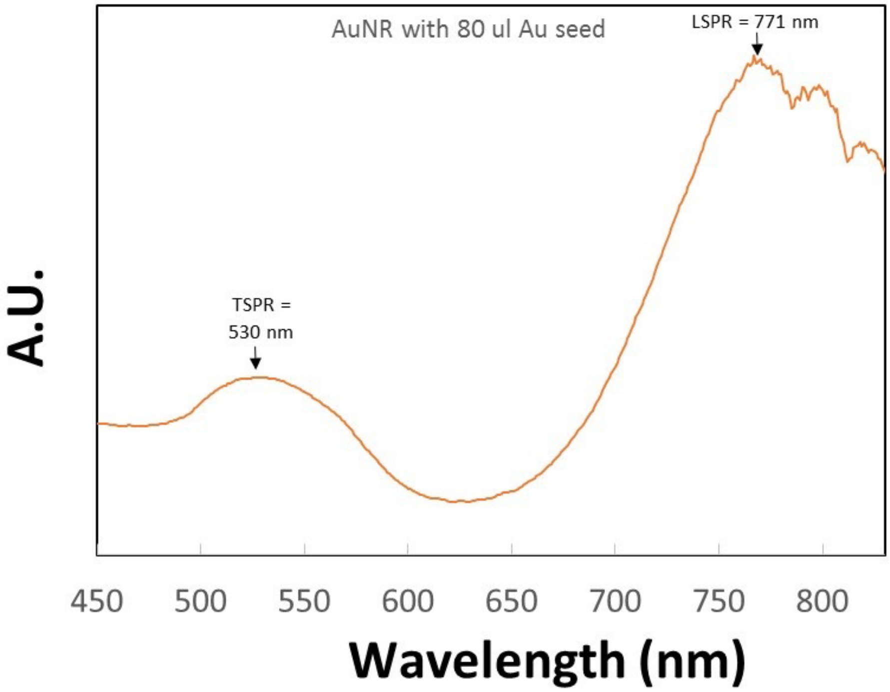

Fig. 15 UV-Vis spectrum for synthesized AuNRs with CTAB using 80-μL Au seed during the seed-mediated synthesis method

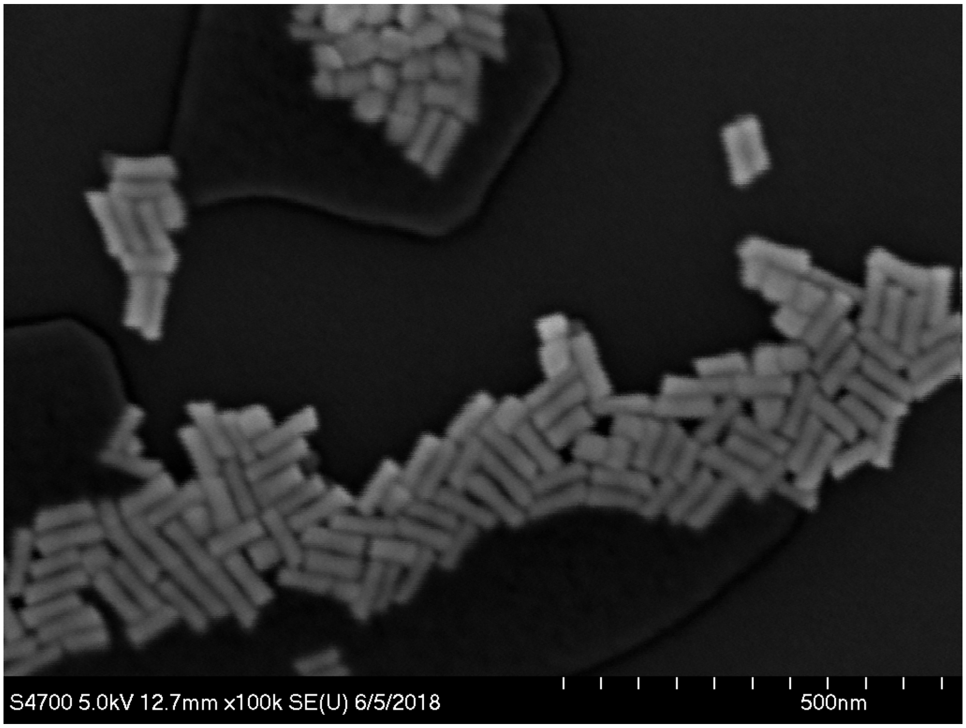

Fig. 16 SEM image of synthesized AuNRs with CTAB using 80-μL Au seed during the seed-mediated synthesis method

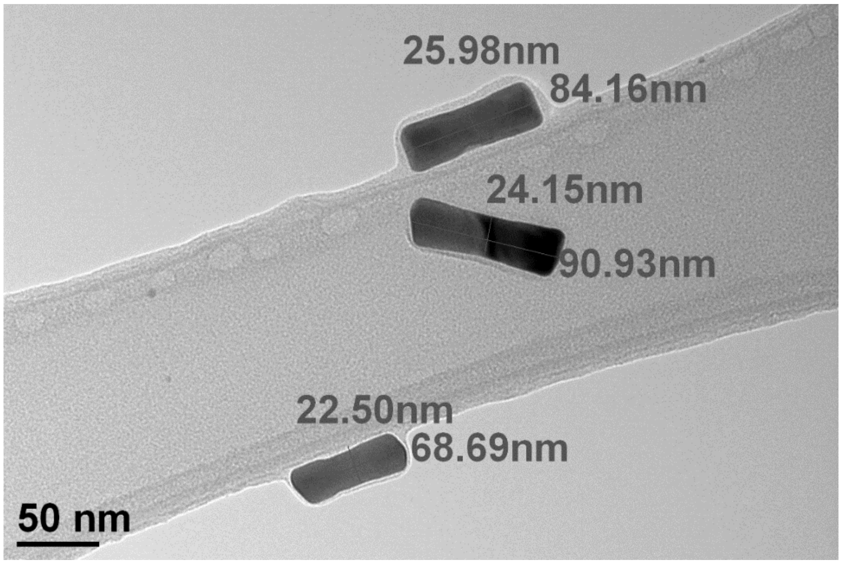

Fig. 17 BF-TEM image of synthesized AuNRs with CTAB using 80-µl Au seed during the seed-mediated synthesis method

In the AuNR synthesis with CTAB, the LSPR was blue shifted as the Au seed increased from 80 to 160 µL as shown in Fig. 18. The diameter of AuNR with CTAB was also decreased from 24.21 to 9.95 nm as shown in Fig. 19.

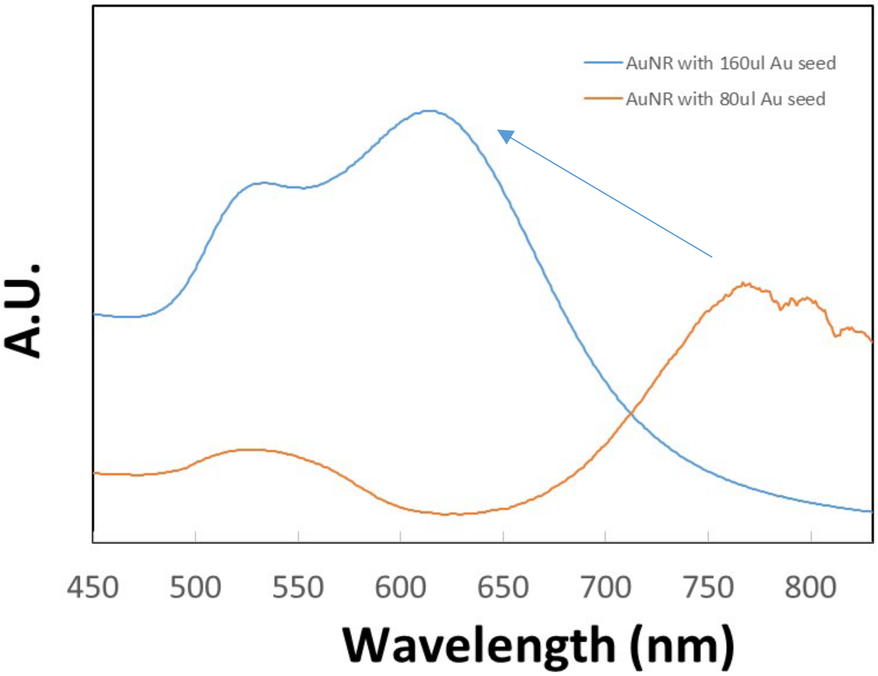

Fig. 18 UV-Vis spectra change of AuNR with different Au seed amount during AuNR synthesis with CTAB

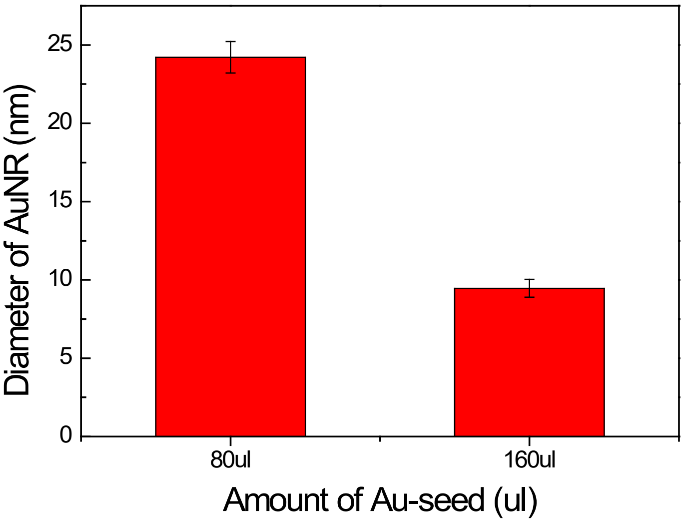

Fig. 19 Diameter of AuNR variation according to the amount of Au seed during AuNR synthesis with CTAB

In an attempt to increase rod diameter, a synthesis methodology using NaOL was employed. The UV-Vis spectrum of AuNR with NaOL using 16-μL Au seed during the seed-mediated synthesis is shown in Fig. 20. The LSPR of AuNRs is 1059 nm, which could be tuned to other wavelengths as desired by tuning the reaction conditions. It should be noted that the LSPR:TSPR ratio is greatly enhanced with this approach, showing an increase in material monodispersity. BF-TEM and SEM analysis of the produced materials is shown in Figs. 21 and 22, respectively. The average diameter of AuNR with NaOL using 16 μL of Au seed is 14.01 nm with an aspect ratio of 6.4. Since the theoretical aspect ratio of AuNR is 6.33, the measured and theoretical aspect ratios are in good agreement.

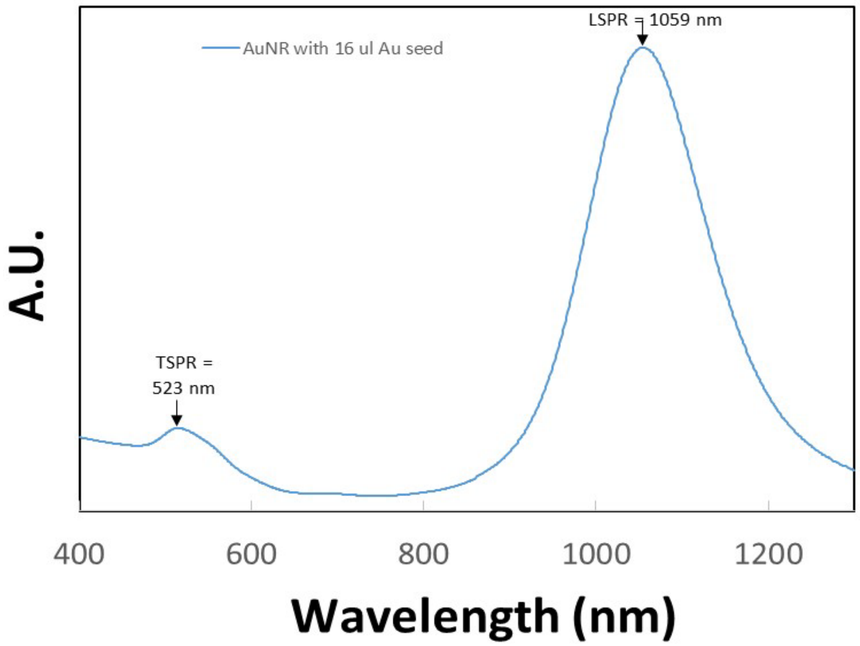

Fig. 20 UV-Vis of synthesized AuNRs with NaOL using 16-μL Au seed during the seed-mediated synthesis method

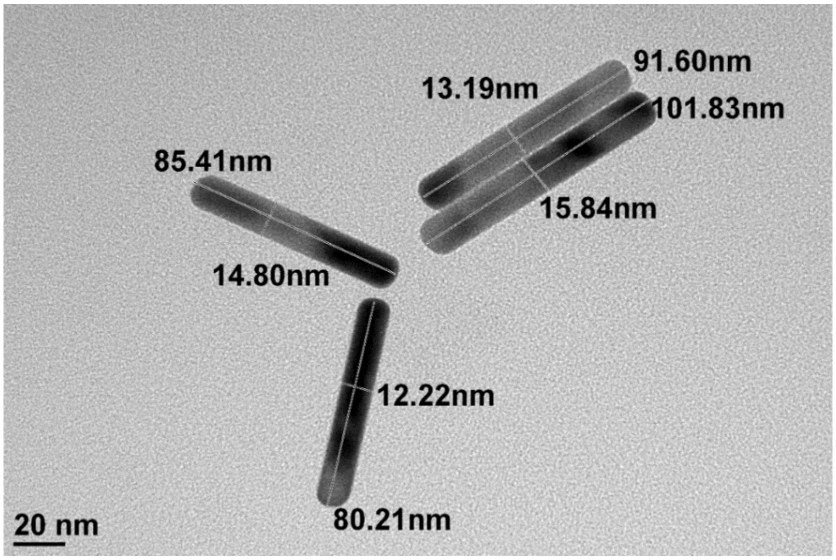

Fig. 21 BF-TEM image of synthesized AuNRs with NaOL using 16-μL Au seed during the seed-mediated synthesis method

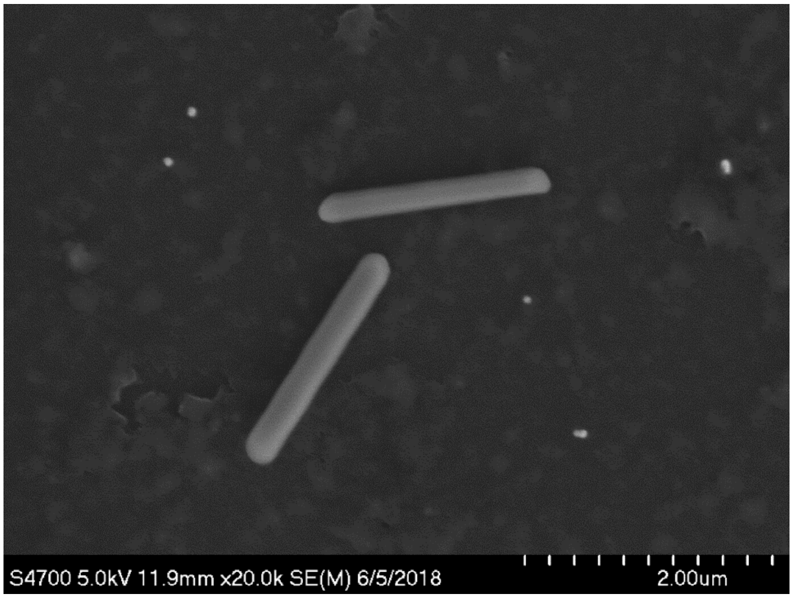

Fig. 22 SEM image of synthesized AuNRs with NaOL using 16-μL Au seed during the seed-mediated synthesis method

The UV-Vis spectrum of AuNR with NaOL using 8 μL of Au seed is shown in Fig. 23, showing an LSPR peak at 674 nm. Through evaluation of the SEM and BF-TEM results shown in Figs. 24 and 25, respectively, it can be seen that a decrease in aspect ratio and mono-dispersity results from the decreased seed amount. The average diameter of the rods produced is 35.5 nm, demonstrating that the diameter of AuNR decreases with an increase of Au seed during the synthesis as shown in Fig. 26. The simple adjustment of Au seed amount in this method results in a substantial red shift in the LSPR peak location when compared to the AuNRs synthesized with a doubled seed amount as shown in Fig. 27. In the AuNR synthesis with CTAB, the LSPR was blue shifted with an increase of Au seed.

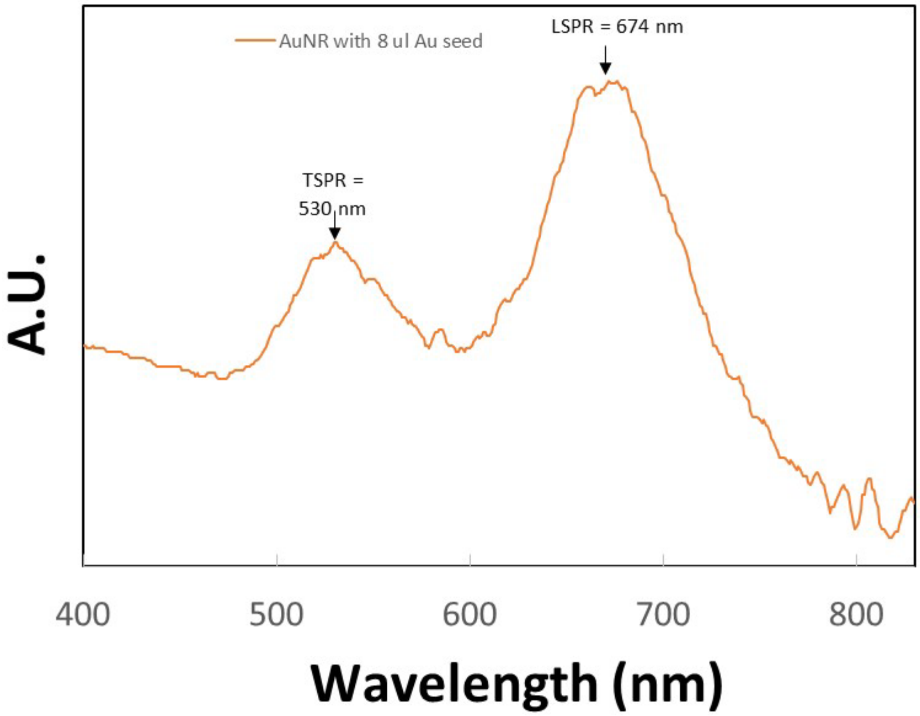

Fig. 23 UV-Vis spectrum for synthesized AuNRs with NaOL using 8-μL Au seed during the seed-mediated synthesis method

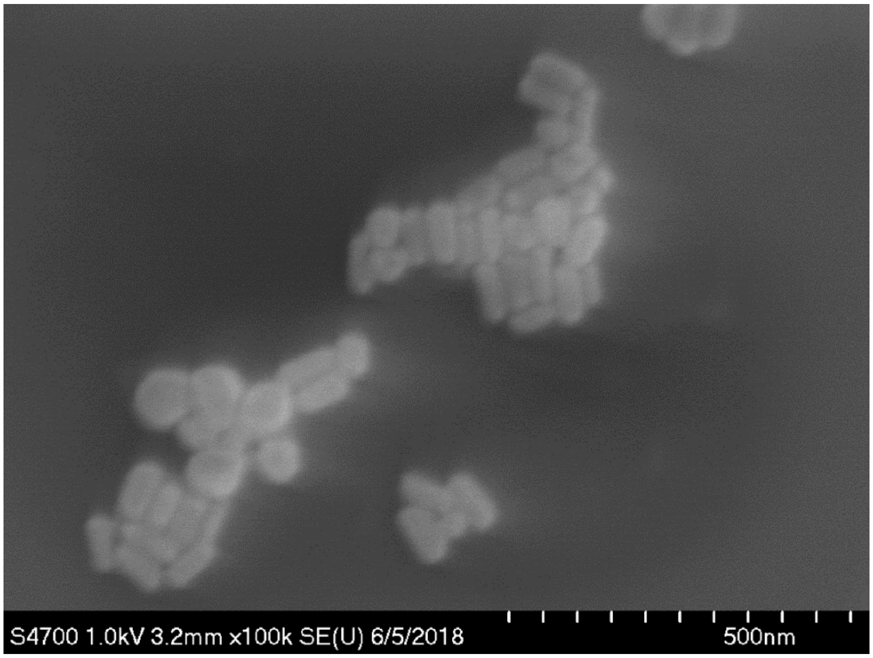

Fig. 24 SEM image of synthesized AuNRs with NaOL using 8-μL Au seed during the seed-mediated synthesis method

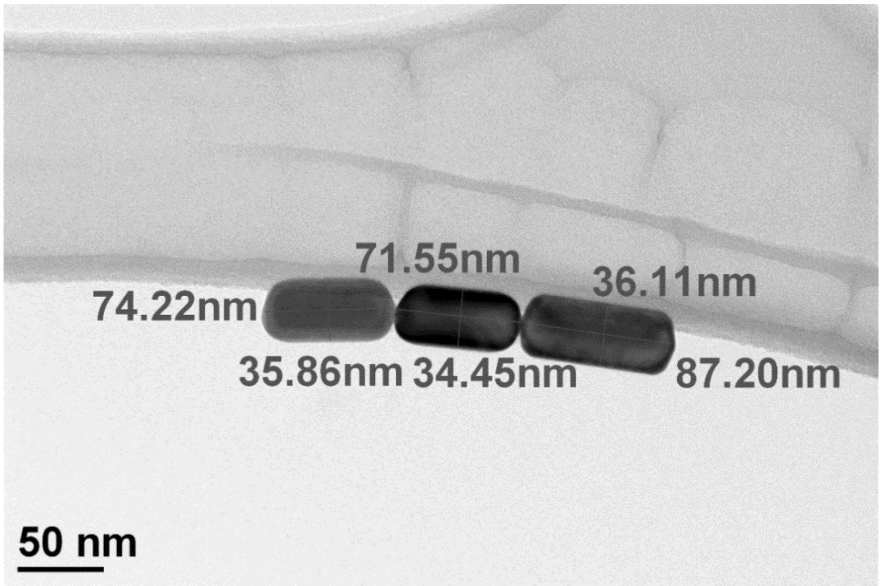

Fig. 25 TEM image of synthesized AuNRs with NaOL using 8-μL Au seed during the seed-mediated synthesis method

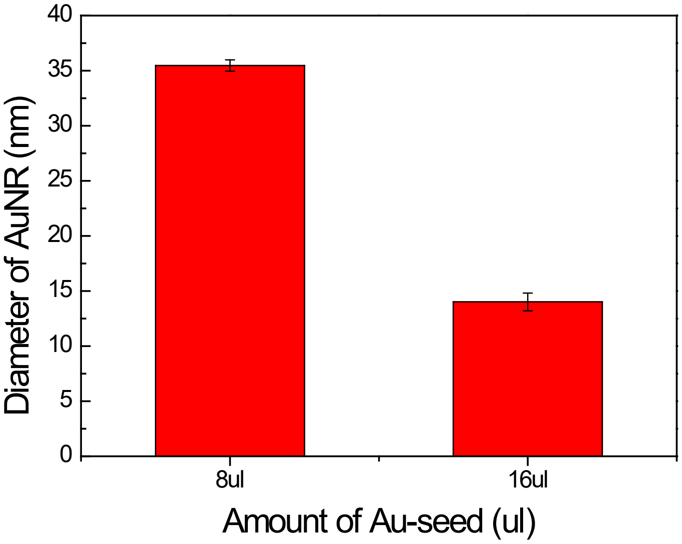

Fig. 26 Diameter of AuNR variation according to the amount of Au seed during AuNR synthesis with NaOL

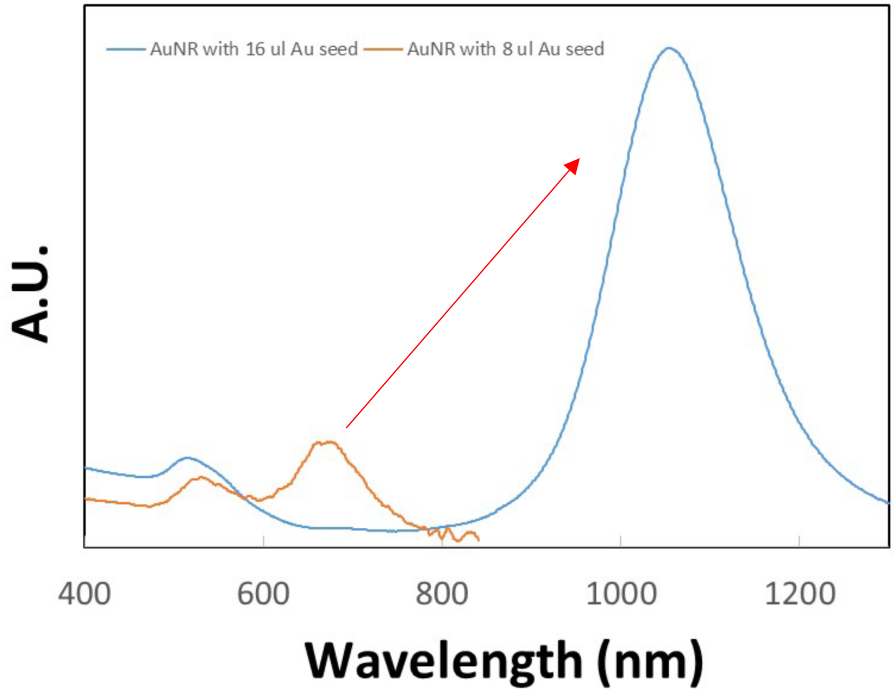

Fig. 27 UV-Vis spectra change of AuNR with different Au seed amount during AuNR synthesis with NaOL

Since AuNR synthesis is a time-consuming process and performed in small batch quantities, high-quality materials are typically difficult to scale. In this work, a scaled AuNR synthesis approach was investigated where a direct scaling of Au-seed and growth solution concentrations is explored. For example, if a 25-fold increased quantity of AuNR is required, the amount of Au seed and AA or HQ are increased by 25-fold as well.

In Fig. 28, the UV-Vis spectra for massive AuNR synthesized using AA to 25 and 100 times with AA are shown. Interestingly, the standard material synthesis ratio of AuNR produces the expected TSPR as well as LSPR resonance locations. However, as the ratio increased to 25 and 100 times, the LSPR disappeared. LSPR shows just a shoulder around 600 nm, suggesting that only nanoparticle structures have formed. LSPR disappearance is more evidently shown in Fig. 29, where HQ is used as the reduction agent, again demonstrating that rods were not formed through the scaled procedure. It is known that $AgNO_3$ has the most effect on longitudinal growth of AuNR during the synthesis, thus $AgNO_3$ concentration was isolated in AuNR synthesis procedure. As the ratio of AuNRs increased from 1- to 50-fold, a blue shift of the LSPR peak occurred, which is believed to be due to the agglomeration of Au seed and AuNR.

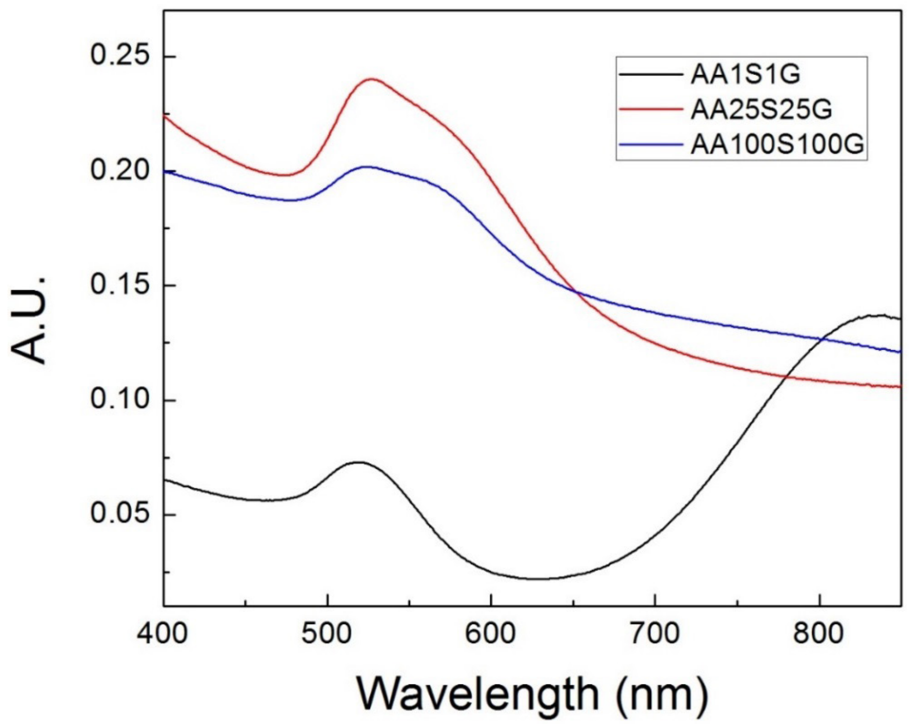

Fig. 28 UV-Vis spectra for massive synthesized AuNR with AA

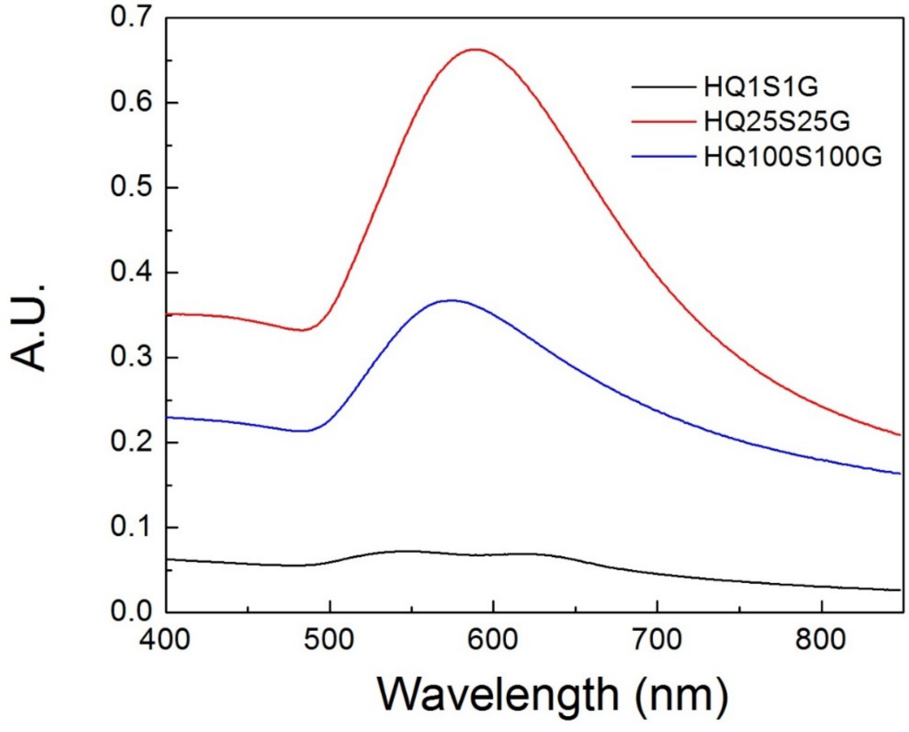

Fig. 29 UV-Vis spectra for massive synthesized AuNR with HQ

In the scaled-up AuNR study, we can conclude that the increase of Au seed as well as AA and HQ can increase the amount of AuNRs synthesized. However, the increase of Au seed results in a significant blue shift, trending toward particle formation instead of tailored nanorod structures. This phenomena can be alleviated by increasing the amount of $AgNO_3$ during the growth stage, as shown in Fig. 30. To study the stability of massive AuNRs synthesized, UV-Vis spectra variation has been studied after 1 day. The UV-Vis variation of 1S1G with HQ after 2 h and 1 day shows a blue shift as time passes (Fig. 31). However, as shown in Fig. 32, 25S25G with HQ shows a red shift. The microstructure of 25S25G with HQ was examined using TEM, as shown in Fig. 33. The diverse shapes of AuNRs, as well as AuNPs, suggests that further optimization of a scaled approach is required and new methodologies should be employed besides direct scaling of material components.

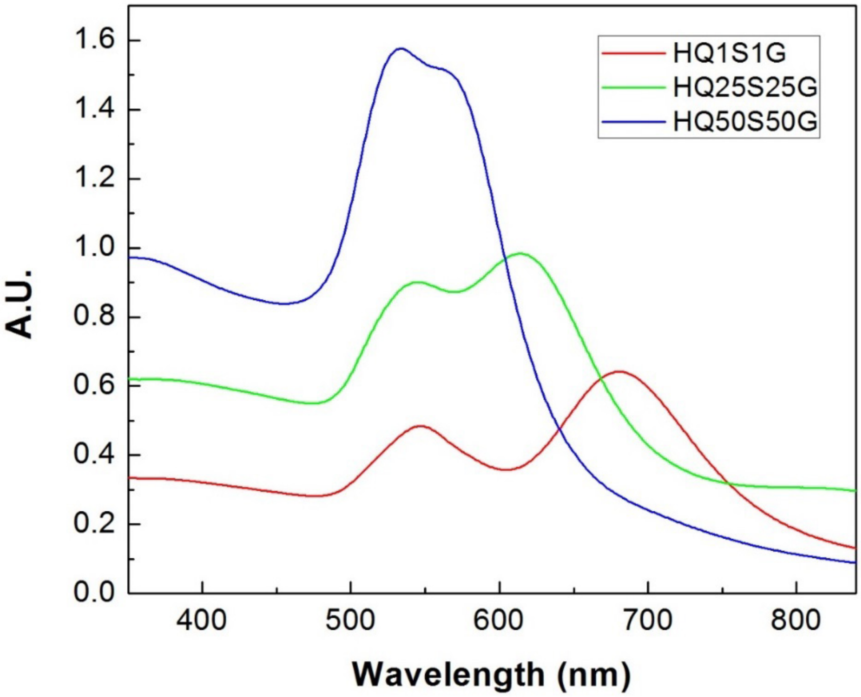

Fig. 30 UV-Vis spectra for massive synthesized AuNR with HQ with increased $AgNO_3$ concentrations

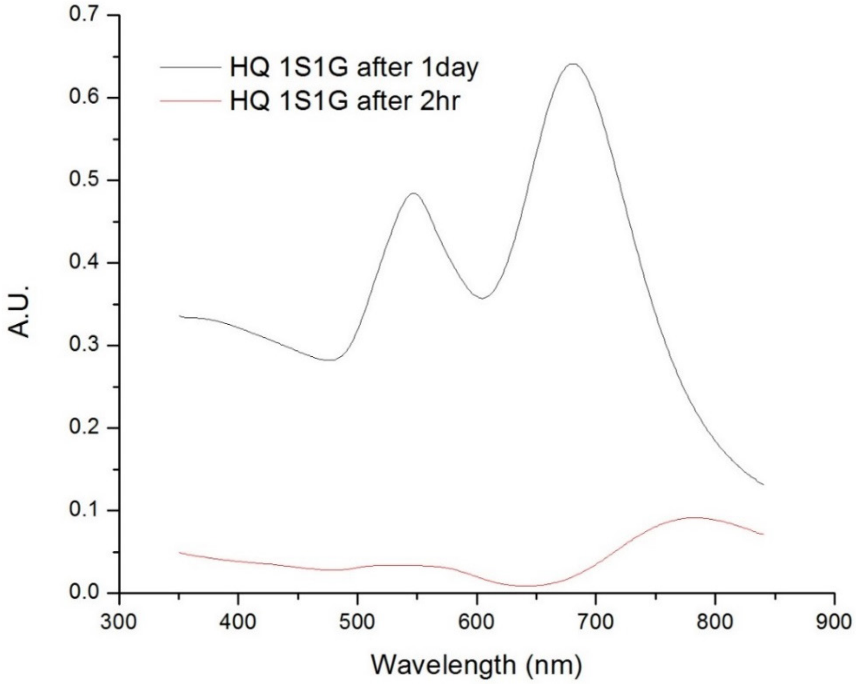

Fig. 31 UV-Vis spectra change after 1 day of synthesis on 1S1G with HQ

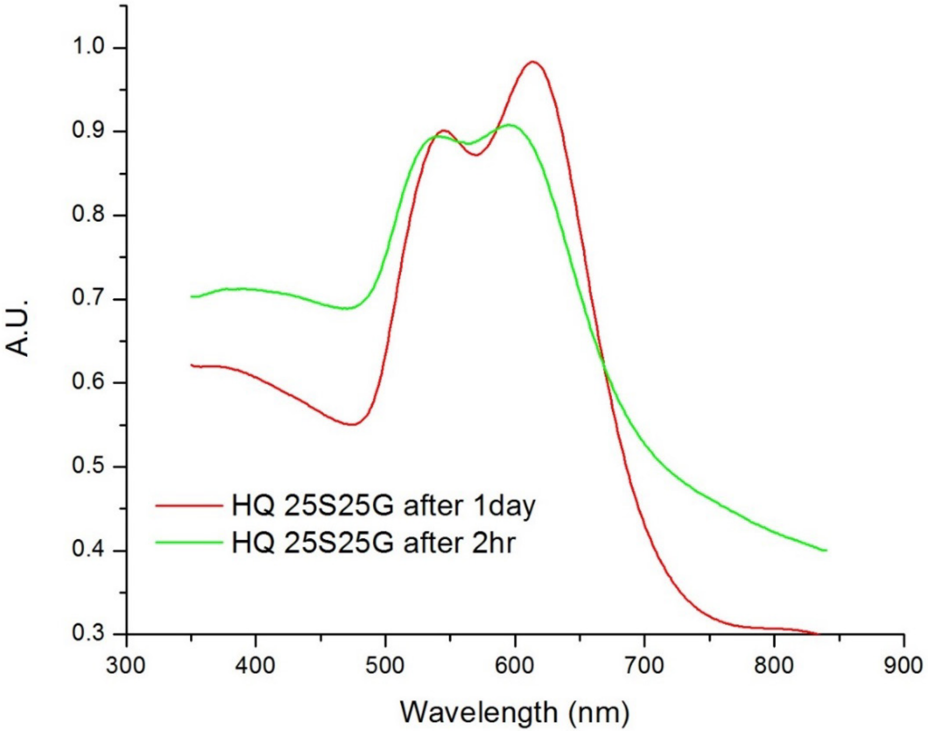

Fig. 32 UV-Vis spectra change after 1 day of synthesis on 25S25G with HQ

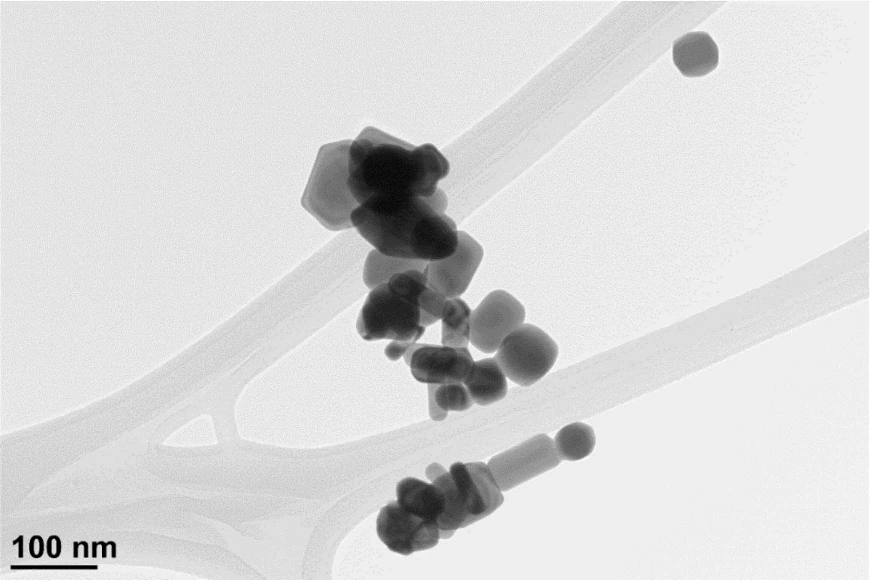

Fig. 33 BF-TEM image of massive AuNRs with HQ (25S25G)

3.2 AuNR-Cu_2O

It has been shown that Cu_2O is a typical p-type semiconductor. Because of its narrow forbidden band, Cu_2O can efficiently absorb visible light and has a high absorption coefficient.[17] Also it has potential applications in solar energy conversion and photocatalysis, electrode materials, catalysts, and gas sensors.[18–21] In 1998, Hara et al.[22] found that Cu_2O can split water under visible light due to its band gap. After this discovery, Cu_2O has been researched as a potential photocatalyst by itself and in combination with noble metal catalysts such as Au.[23,24] Recently, Yu et al.[25] reported hollow porous Cu_2O microspheres and their photocatalytic properties under visible light irradiation. It has been demonstrated that light absorption properties of Cu_2O nanoshells can be fine-tuned in the visible region by tailoring the dimensions and interior structures of the single layer or multilayer nanoshells.[26,27]

The core-shell and dumbbell structure of AuNR with Cu_2O could provide an optimal material platform to use direct plasmon energy transfer to power the catalytic activity of the Cu_2O. To synthesize Au-Cu_2O core-shell materials, related synthesis methods were applied[28] using other oxide materials. To date, there has been no report of AuNR-Cu_2O dumbbells. To synthesize AuNR-Cu_2O dumbbells, a Cu_2O microsphere synthesis mechanism was investigated. As schematically represented in Figs. 34 and 35, AuNR-Cu_2O dumbbell synthesis methods should be optimized to prevent full oxide coating, which could be achieved through targeted oxide deposition at the rod ends via alterations in the adsorbed CTAB density.

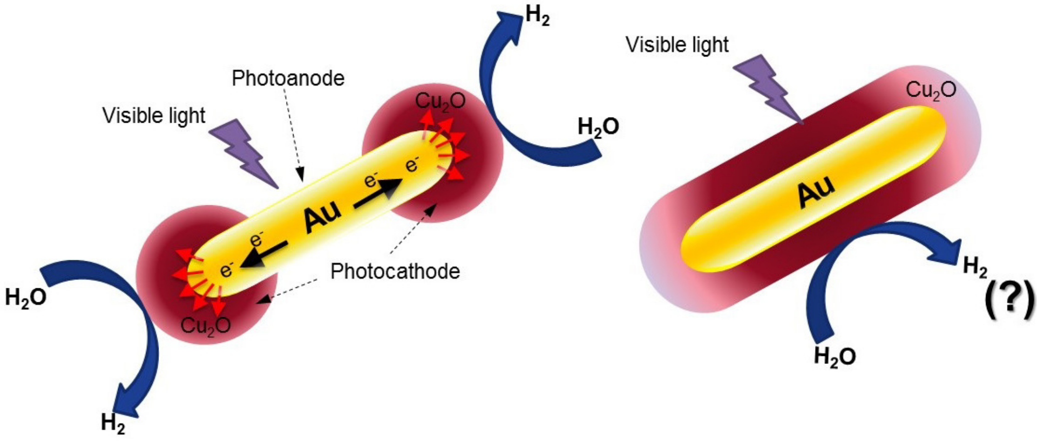

Fig. 34 Schematics of AuNR-Cu_2O dumbbell and core-shell

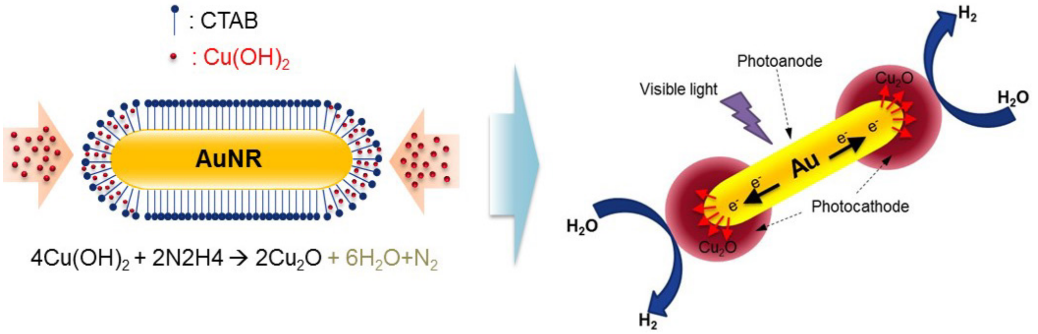

Fig. 35 Schematics showing AuNR-Cu_2O dumbbells

To synthesize AuNR-Cu_2O dumbbells, $TiCl_3$ has been replaced by $CuCl_2$, and ammonium monohydrate (NH_3H_2O) is used instead of the sodium bicarbonate described in Section 2.2.7. In the process of hollow microsphere Cu_2O synthesis, the anionic surfactant SDS acts as the role of a soft template and is a stable micelle in the solution. The inside lipophilic groups are intertwined together in aqueous solution, whereas the outside hydrophilic groups containing sulfates attract Cu_2^+ to form the copper-rich zone. When ammonia and NaOH were added to the solution, the $Cu(OH)_2$ precursor formed first at the outside of the micelle and then was reduced to Cu_2O by hydrazine hydrate, which is common reducing agent. At the same time, N_2 was generated in the redox reaction process and produced copious amounts of bubbles. Under the effects of SDS and bubbles, both of which acted as soft templates, the hollow porous Cu_2O microspheres would form. The suggested chemical reactions are as follows.[25]

$$Cu^{2+} + 2NH_3H_2O \rightarrow Cu(OH)_2 + 2NH^{4+}$$

$$Cu^{2+} + 2OH^{-} \rightarrow Cu(OH)_2$$

$$4Cu(OH)_2 + 2N_2H_4 \rightarrow 2Cu_2O + 6H_2O + N_2\uparrow$$

The SEM image of the AuNR-Cu_2O core-shell structures is shown in Fig. 36. At lower magnifications, the AuNR-Cu_2O images appear to have a cubic structure, while at higher magnifications cylindrical structures can be discerned. Figure 37 shows a BF-TEM image of the AuNR-Cu_2O core-shell structure, which illustrates the direct identification of the AuNR core inside of the Cu_2O shell. It is known that for Au and Cu_2O, the great similarity in their crystalline structures (face-centered cubic crystals) and the relatively small lattice mismatch (4.5%) make it possible to heteroepitaxially grow Cu_2O layers on the surface of Au nanoparticles without much lattice stress under appropriate conditions.[28]

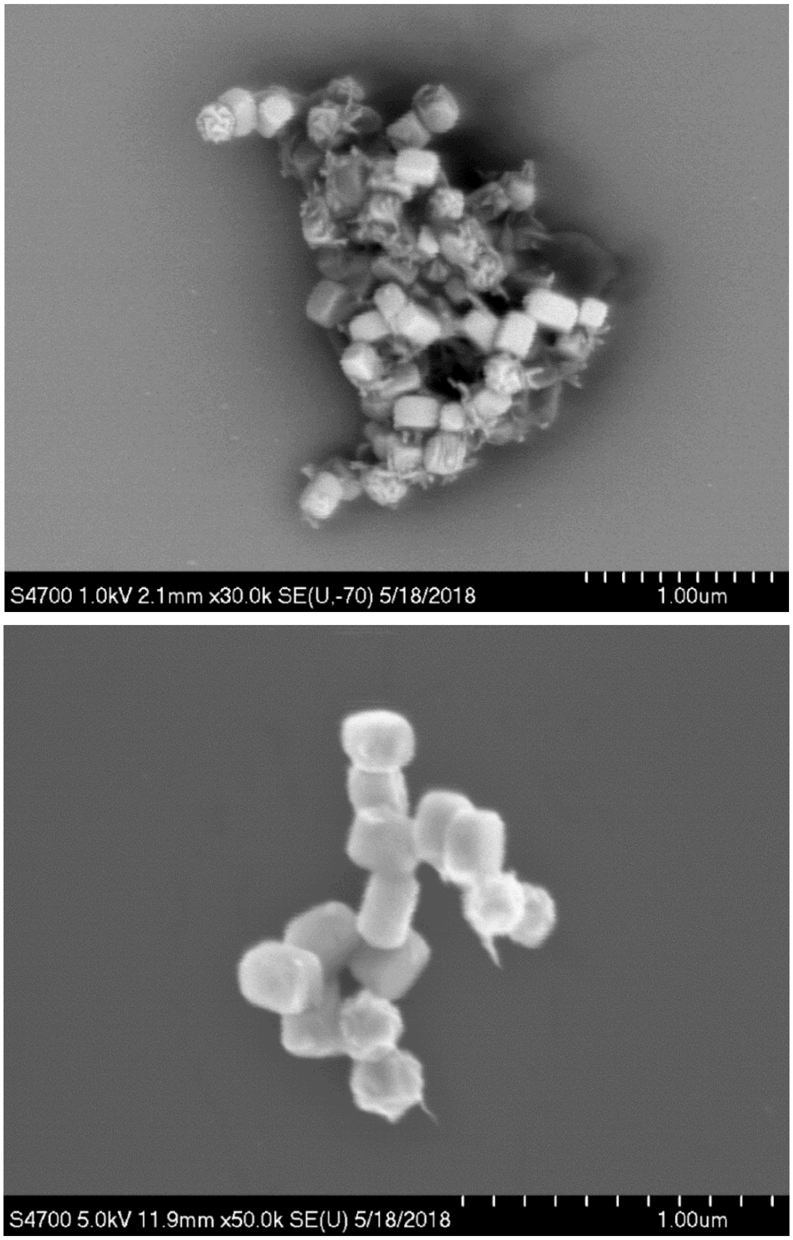

Fig. 36 **SEM images of AuNR-Cu_2O core-shell using high aspect ratio of AuNR (AR = 5)**

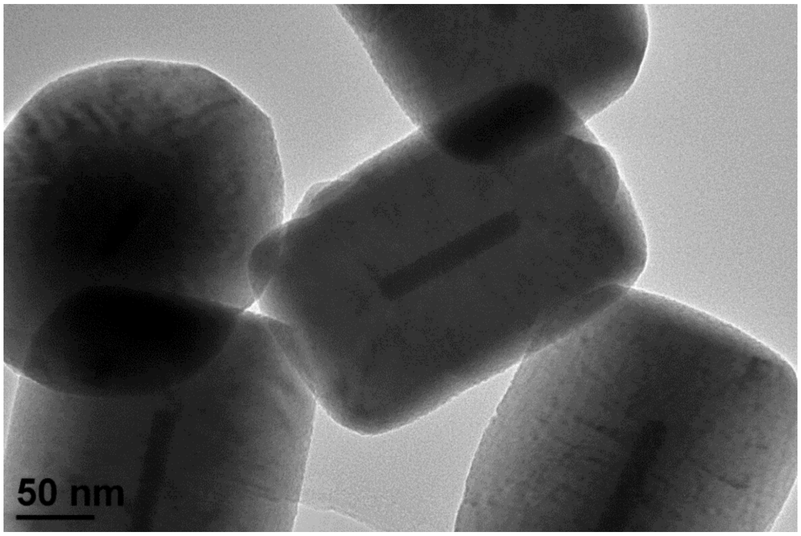

Fig. 37 BF-TEM images of AuNR-Cu_2O core-shell using high aspect ratio of AuNR (AR = 5)

To expand beyond core-shell structures, alternate methods were explored to develop AuNR-Cu_2O dumbbells. The UV-Vis properties of the produced dumbbell structures are shown in Fig. 38. Similar to what occurred with AuNR-Cu_2O core-shells, the signature surface plasmon resonance (SPR) of AuNR disappears after the Cu_2O coating onto the surface of AuNR and a singular peak at 493 nm emerges. This is contrary to reported literature, where Cu_2O coatings onto AuNRs yields two primary SPRs that are dampened/shifted to absorption peaks at around 500 and 650 nm,[23] depending on the AuNR morphology.

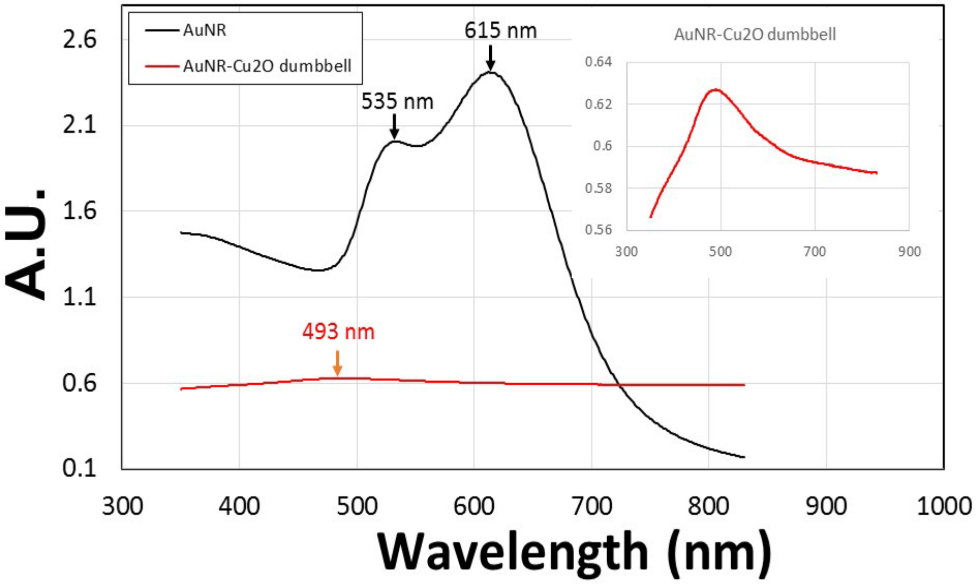

Fig. 38 UV-Vis spectra of AuNR-Cu_2O dumbbell

3.3 Hollow Cu_2O and TiO_2 Particles

Hollow Cu_2O particles have been synthesized to compare with AuNR-Cu_2O followed by Yu et al.[25] The BF-TEM image of hollow Cu_2O is shown in Fig. 39, which displays a similar morphology to that achieved with gold hollow shell particles.[29] As shown in the BF-TEM image, the middle of the particle's bright areas indicate the hollow core. In further investigation with STEM-HAADF as well as STEM X-ray mapping, the holes in particles are clearly seen. UV-Vis results of the hollow Cu_2O are shown in Fig. 40 before and after sonication. Before sonication, SPRs of hollow Cu_2O are not evident; however, after sonication SPR peaks at around 360 nm and shoulders at 450 nm, similar to that of previously reported work.[25] Additionally, TiO_2 microspheres have been synthesized for control comparisons and are shown in Fig. 41. There are many similarities in the synthesis of hollow Cu_2O structures compared to TiO_2 particles. The surface morphologies of the two types of particles are also very similar.

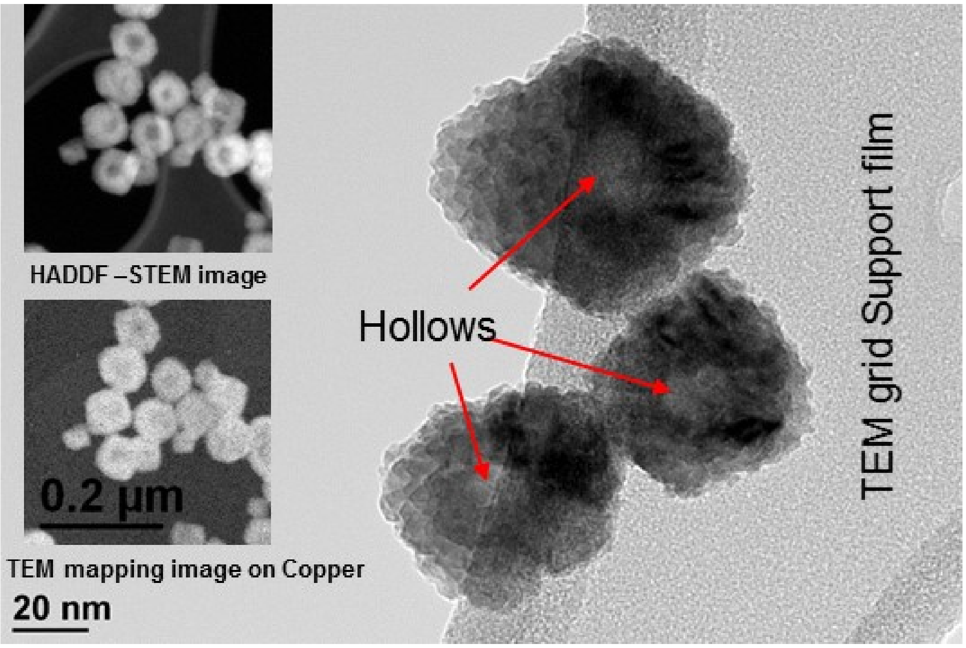

Fig. 39 BF-TEM images of hollow Cu_2O microspheres. The inset shows a STEM-HAADF image and a corresponding Cu-Kα X-ray map of the hollow microspheres.

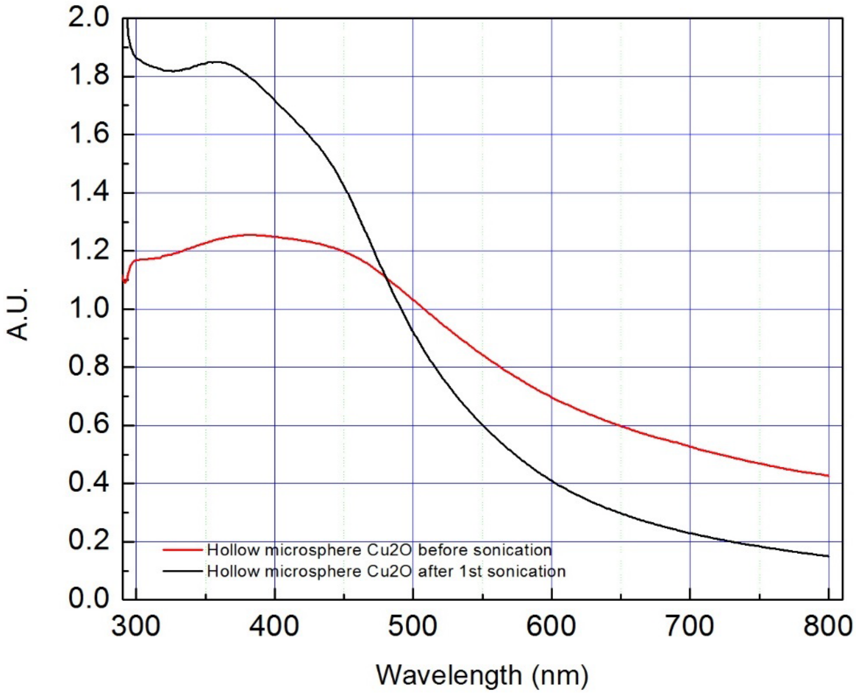

Fig. 40 UV-Vis spectrum of microsphere hollow Cu_2O

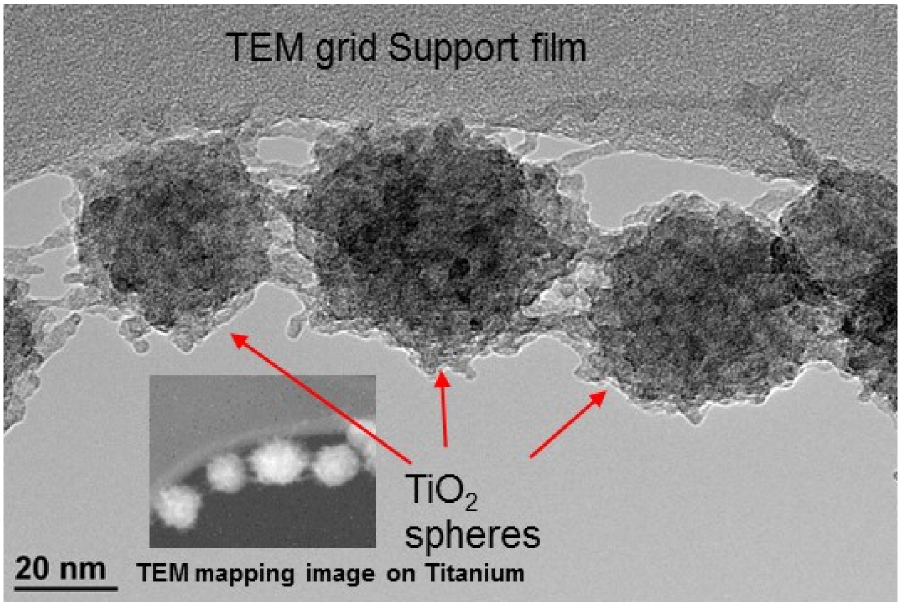

Fig. 41 TEM image of TiO_2 spheres. The insert shows a STEM Ti-Kα X-ray map.

3.4 Nano-Sized Graphene Oxide (nGO)

Recent efforts have demonstrated the preparation of graphene oxide by the chemical exfoliation of graphite.[11,12] Briefly, it consists of the reaction of graphite flakes with concentrated H_2SO_4 and $KMnO_4$ to obtain individual sheets in an oxidized state. The resultant suspension is extensively washed with distilled water by filtration and centrifugation and finally subjected to dialyses to remove ionic contaminants. The resulting graphene oxide is dried by lyophilization to avoid aggregation. The nGO preparation was based on the breakage of graphene oxide by combined mechanical aging and ultrasonication processes. Graphene oxide was resuspended in water and subjected to different ultrasonication/stirring times.

Gonçalves et al.[30] reported a mechanical-driven graphene oxide size-reduction approach through the use of high-energy probe sonication. In this work, five sets of sonication treatment times were applied, giving rise to five graphene oxide suspensions, herein referred to as GO1 (0 min), GO2 (30 min), GO3 (60 min), GO4 (90 min), and GO5 (180 min). The final material (GO5) was centrifuged (12,000 rpm, 15 min^{-1}) to remove possible remaining graphene oxide bigger flakes in the solution.

Kumar et al.[31] reported the role of reduced graphene layers as highly efficient electron acceptors and transporters to facilitate the use of hot electrons for plasmonic photocatalysts. The femtosecond transient spectroscopic results also show 8.7 times higher transport efficiency of hot plasmonic electrons in rGO-AuNPs compared with AuNPs. However, as the AuNP is coated with rGO, the oxidation photocatalytic efficiency is increased.

To synthesize AuNR-rGO-Cu_2O as well as AuNR-rGO-TiO_2, nGO must be prepared. Several approaches were used to optimize nGO formation. The initial method involved the direct application of SLGO. The SLGO had average lateral dimensions on the order of 800 nm. Directly applying the as-produced SLGO to the AuNRs from AuNR-nGO hybrid structures, the large size of the SLGO relative to the AuNRs prevented wrapping of the rod structure and instead yielded simple attachment of the AuNR to the graphene sheets, as shown in Fig. 42. To achieve wrapping of graphene around the rod structure, reduced size graphene materials are required.

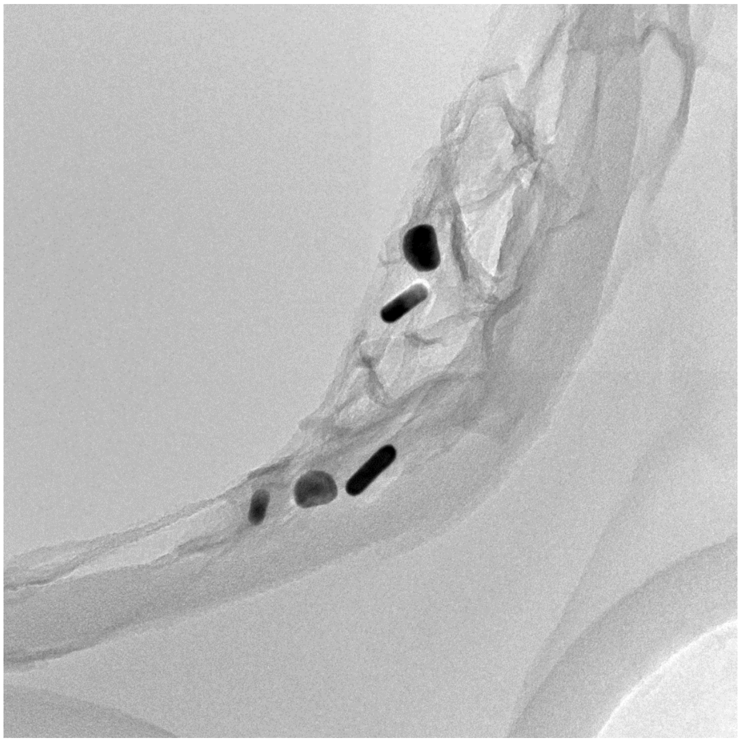

Fig. 42 BF-TEM image of AuNR and single layer of graphene oxide as-received

Most of the nGO synthesis reported in literature starts from carbon precursors (graphite, carbon nanotubes, etc.) using modified Hummer's method.[30,32] The direct synthesis of nGO using oxidation was performed following Kim et al.[11,12] recipe. After synthesis, dynamic light scattering (DLS) measurements were conducted, with the graphene oxide dimensions before and after oxidation shown in Fig. 43. Before sonication the average size of single layer graphene oxide is about 800 nm, whereas after sonication the average size decreases to about 130 nm. BF-TEM images of the postprocessed graphene oxide are shown in Fig. 44.

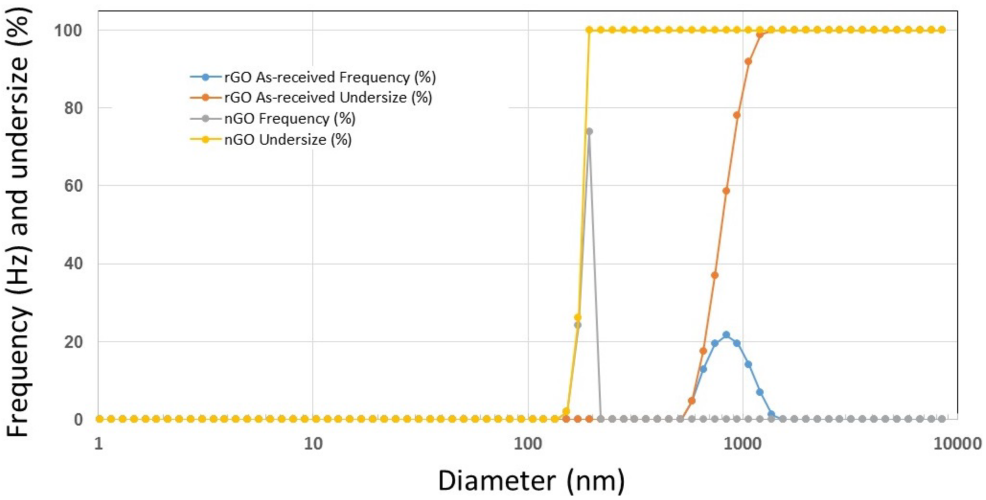

Fig. 43 DLS measurement result of before and after oxidation of graphene oxide

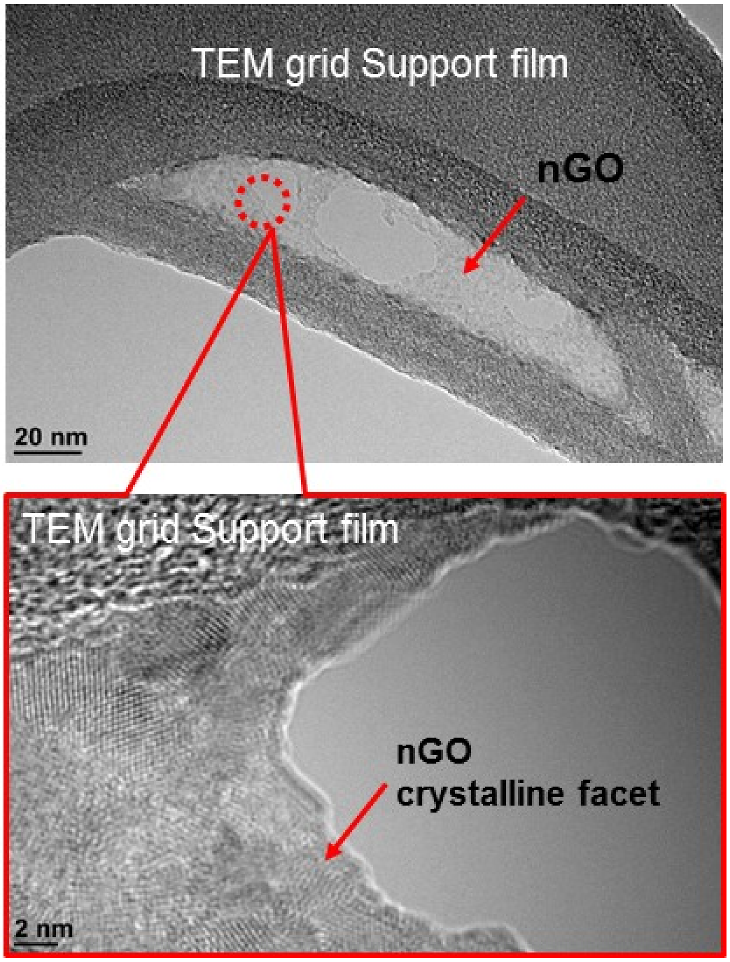

Fig. 44 BF-TEM images of nGO synthesized by oxidation method

A separate method to control nGO lateral dimensions includes direct mechanical breaking of the film. Gonçalves et al.[30] showed that heat generation during ultrasonication has a great effect on breaking graphene flake into nGO, especially along the oxide functional group. They reported that longer sonication times produced a smaller graphene oxide size. In our study, the ultrasonication time was varied between 3 and 12 h with DLS measurements made every 3 h after the sample had cooled. The Z-average and mean average size of graphene oxide according to the sonication time variation are shown in Figs. 45 and 46. The Z-average size measurement results in Fig. 45 demonstrate that after initiating ultrasonication on as-received graphene oxide, significant size decreasing effect occurs up until 6 h of sonication. However, after 6 s, the Z-average sizes slightly increase. In Fig. 46, mean average size variation according to the ultrasonication time demonstrates no significant change. The variations in DLS results can be attributed to the DLS measurement mechanism, which measures the hydrodynamic diameter based on volume, as single layer of graphene oxide will behave differently than smaller particle forms.

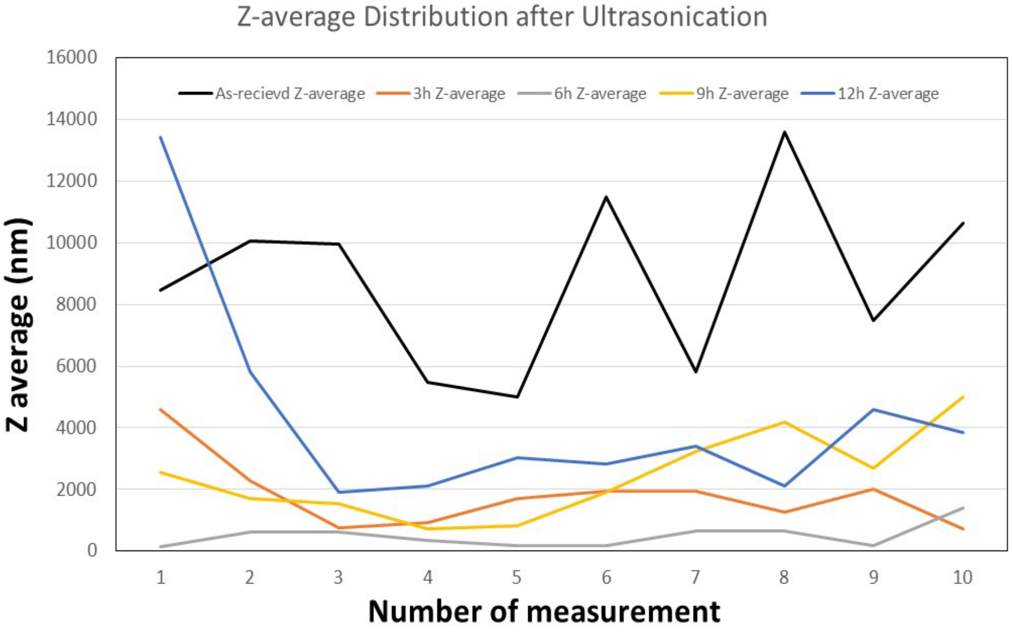

Fig. 45 Z-average results for before and after oxidation of graphene oxide sonication time

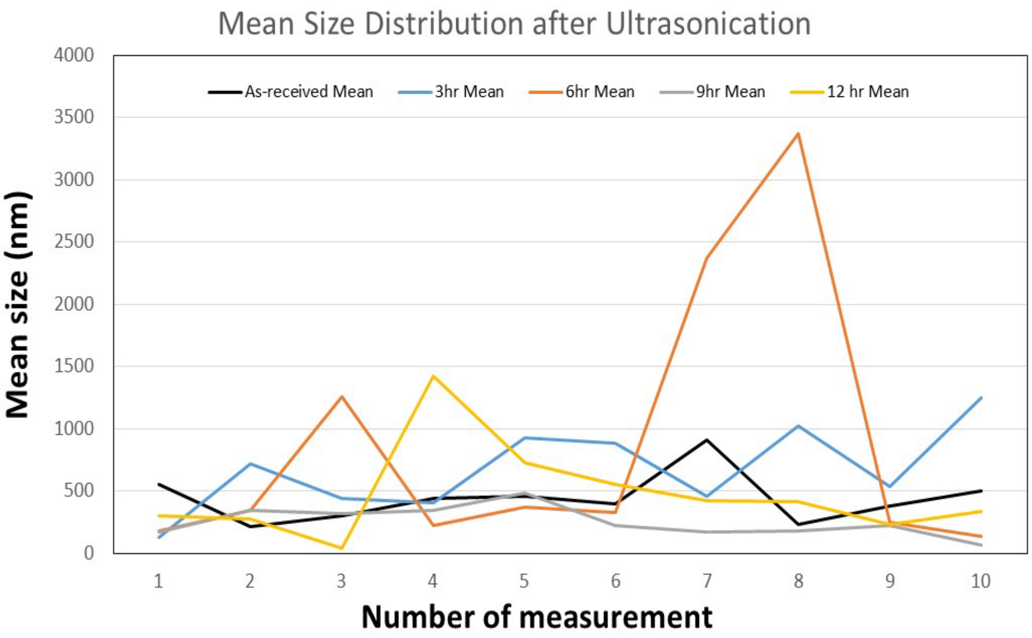

Fig. 46 Mean average for before and after oxidation of graphene oxide sonication time

Figure 47 shows the results of AFM measurements conducted to determine the effect of ultrasonication time on synthesizing nGO. As-received graphene oxide shows large stacked features on the surface of Si-wafer substrate. However, as the ultrasonication time increased from 3 to 12 h, a drastic decrease in lateral dimensions was observed. UV-Vis spectra measurements were also conducted on ultrasonicated graphene oxide samples. Figure 48 shows the significant absorption peaks at around 230 nm and shoulder at around 300 nm, which correspond to the π-π* and n-π*, respectively.

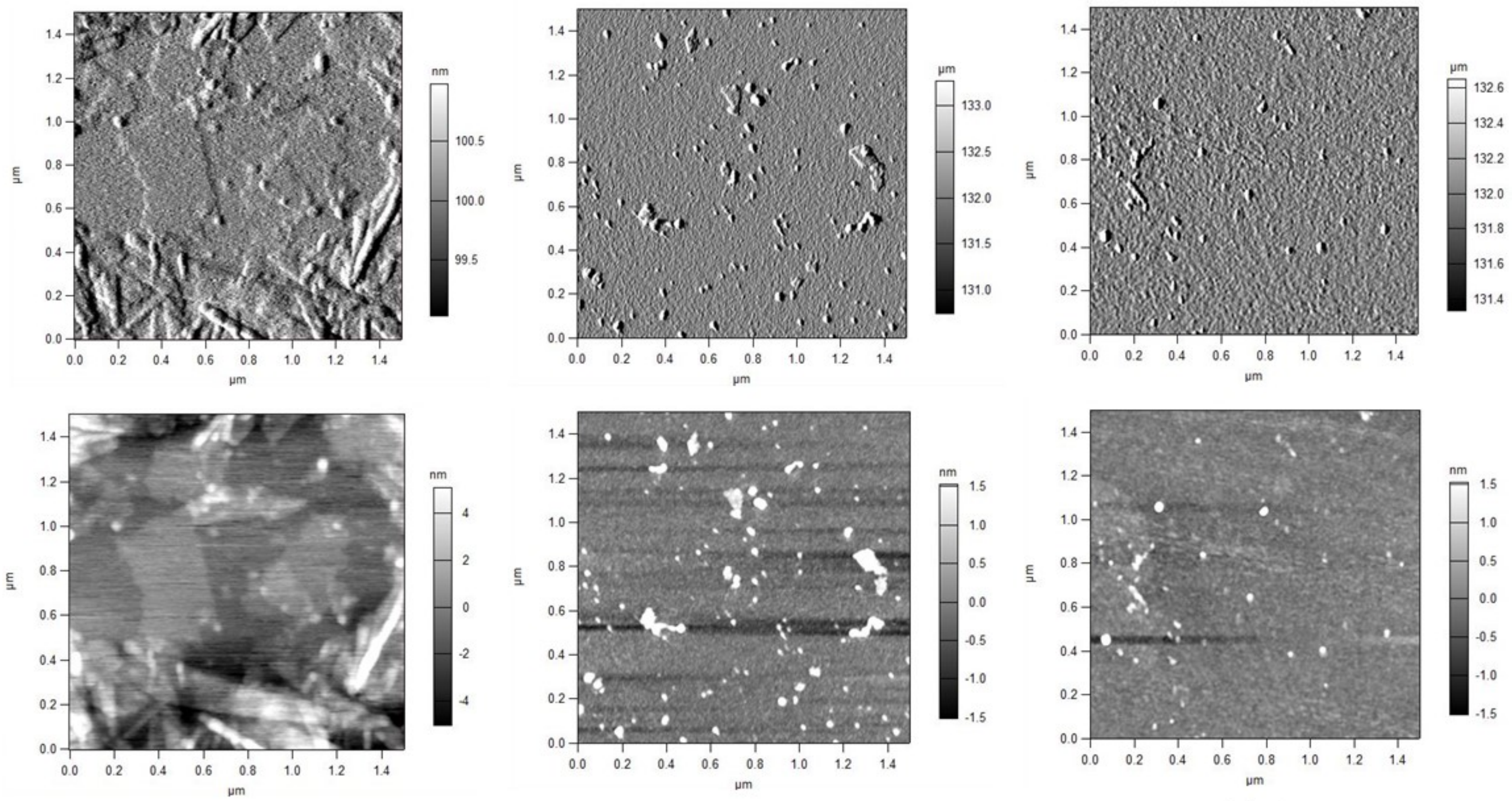

As-received

3 hr

12 hr

Fig. 47 AFM result on nGO according to the ultrasonication time

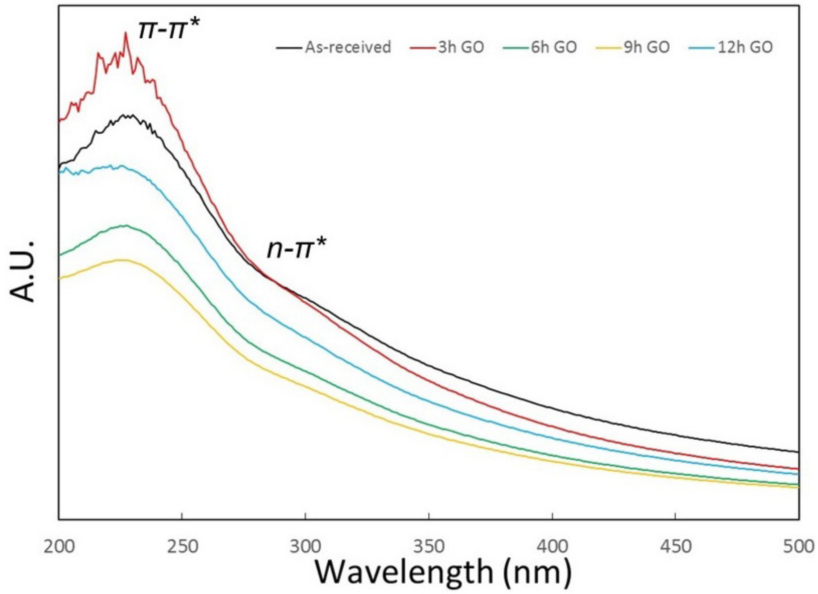

Fig. 48 UV-Vis results on nGO according to the sonication time

The final method that is applied to synthesis of nGO varies from previous approaches as it is a “bottom-up” methodology rather than a “top-down” methodology. With lateral dimensions less than 10 nm, graphene oxide, or graphene terminology, is often altered to be reported as graphene oxide quantum dots or GQDs. In the context of this work, the ability to synthesize GQD materials on the order of <10 nm could be ideal for coating the AuNRs. To synthesize GQDs, the known method using DMF with hydrothermal synthesis was applied. After synthesis the photoluminescent property was observed, with the UV-Vis spectra and corresponding fluorescence shown in Fig. 49. The two images on the left of Fig. 49 show the GQD solution under visible light and UV light, respectively, with GQDs yielding a bright green fluorescence under UV irradiation. The image on the right of Fig. 49 shows photoluminescent emission at 536 nm.

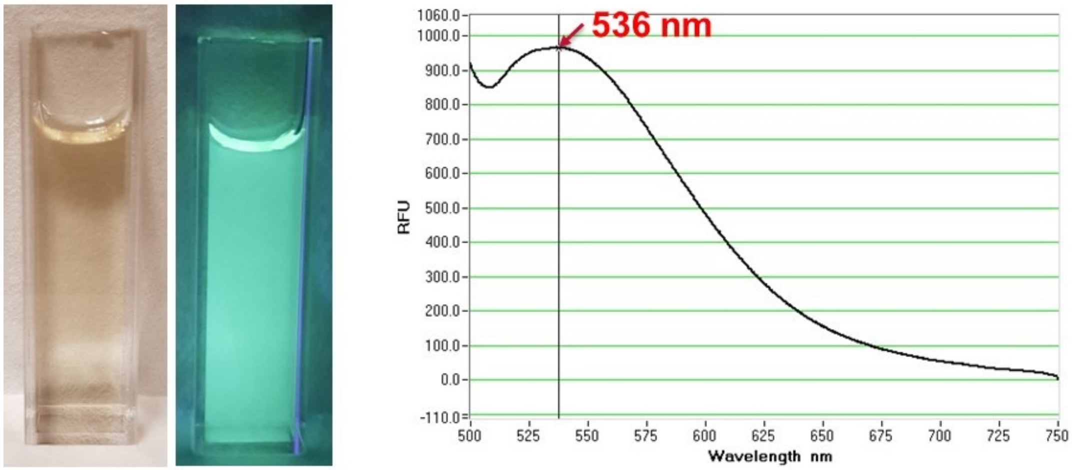

Fig. 49 Photoluminescent properties of GQD in UV irradiation. Left: under visible light and UV light; Right: photoluminescent emission at 536 nm (excitation at 475 nm).

3.5 AuNR-rGO-Cu_2O

Utilizing the produced nGO, a hybridized AuNR-rGO-Cu_2O core-shell has been synthesized. The UV-Vis spectra of AuNR, AuNR-GO, AuNR-rGO, and AuNR-rGO-Cu_2O are compared in Fig. 50. After the coating with Cu_2O, the AuNRs exhibit a significant red shift toward a longer wavelength as well as broadening of the absorption peak, which is in accordance with Zhang et al.[33] results. They ascribed this result to enhanced optical tunability that arises from the unique interactions between the metallic cores and semiconducting shells over the nanometer length scale. They also proposed a wet chemistry approach through which a series of important geometrical parameters of the hybrid nanoparticles, such as shell thickness, shell crystallinity, shell porosity, and core compositions, can be tailored in a highly precise and controllable manner.

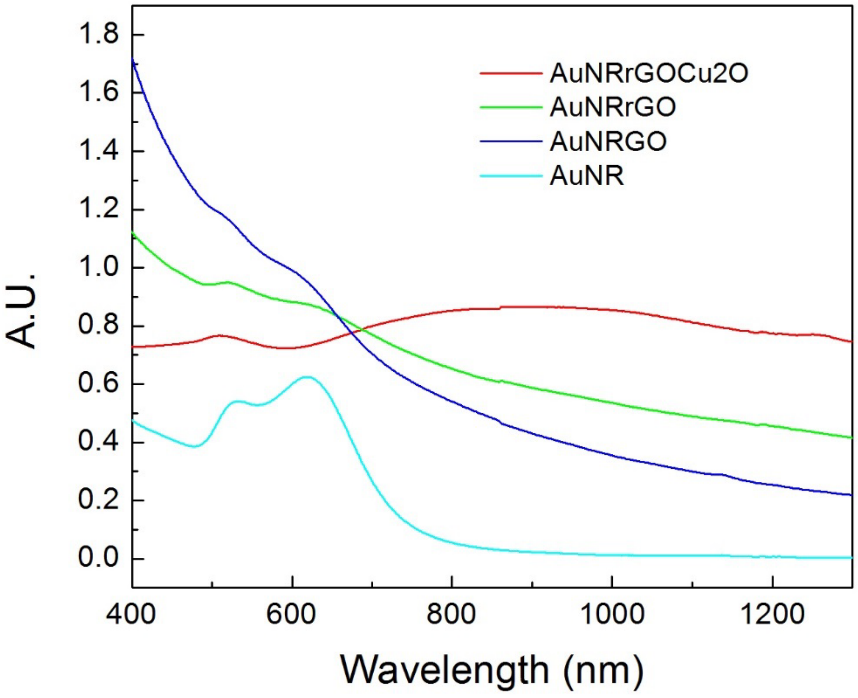

Fig. 50 UV-Vis spectra of AuNR, AuNR-GO, AuNR-rGO, and AuNR-rGO-Cu_2O prepared with nano-sized rGO

Interestingly, after Cu_2O has coated the surface of AuNR, the unique SPR peaks of AuNR disappear. This phenomenon is in accordance with Kuo et al.[28] Kuo et al. reported that after Cu_2O coating, only the characteristic absorption feature of Cu_2O crystals having a weak band gap absorption band at approximately 500 nm and broad light scattering bands in the red and NIR regions due to the large particle sizes were recorded for the core-shell heterostructures. The spectral results provide strong evidence that essentially all the nanocrystals have turned into core-shell particles. Furthermore, the BF-TEM images shown in Fig. 51 demonstrate full hybrid formation.

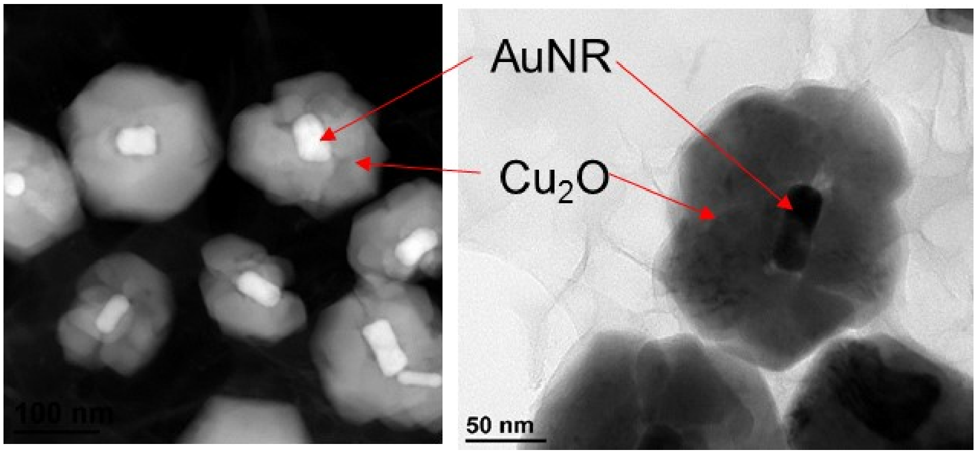

Fig. 51 STEM-HAADF and BF-TEM images of AuNR-rGO-Cu$_2$O

3.6 AuNR-TiO$_2$

At first, the AuNR-TiO$_2$ core-shell structure synthesis was attempted following previously reported procedures by Wu et al.[9] In the reported approach, SDS is used to synthesize AuNR-TiO$_2$ core-shell; however, in this study CTAB was applied instead of SDS. As shown in Fig. 52, the TiO$_2$ shell covers the entirety of the AuNR. In the energy-filtered transmission electron microscopy (EFTEM) elemental map image, shown in Fig. 53, the shells brightly outlined around the AuNRs were revealed as TiO$_2$, as expected. In SEM analysis, the AuNR-TiO$_2$ core-shell appears in both cylindrical and hexahedron structures, as shown in Figs. 54 and 55. UV-Vis analysis has been carried out for the AuNR-TiO$_2$ core-shell and compared to the as-prepared AuNR, as shown in Fig. 56. After the TiO$_2$ coating onto AuNR, the TSPR and LSPR peaks red-shifted from 535 to 545 nm and 615 to 668 nm, respectively, which is in accordance with a previous report.[9]

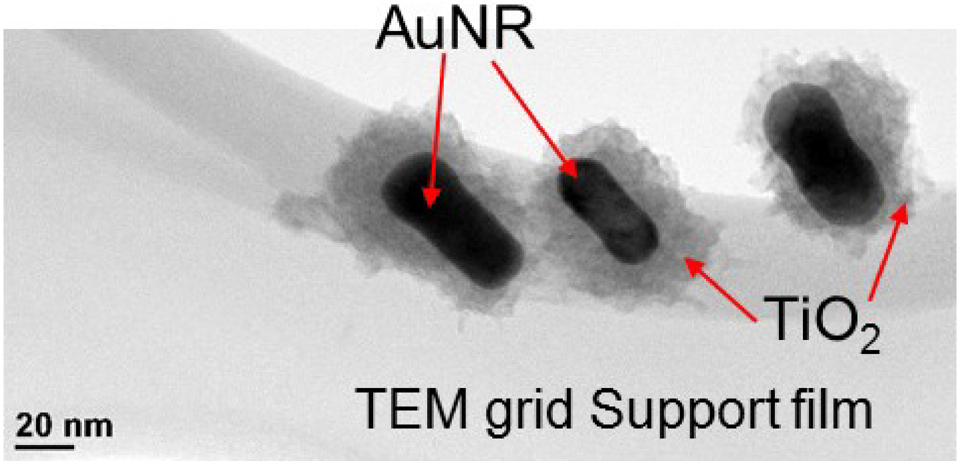

Fig. 52 TEM image of AuNR-TiO$_2$ core-shell

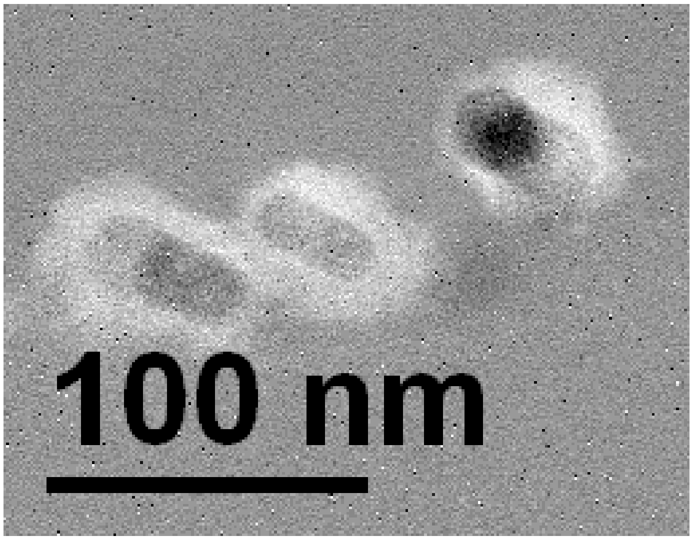

Fig. 53 EFTEM O-K elemental map image of AuNR-TiO_2 core-shell

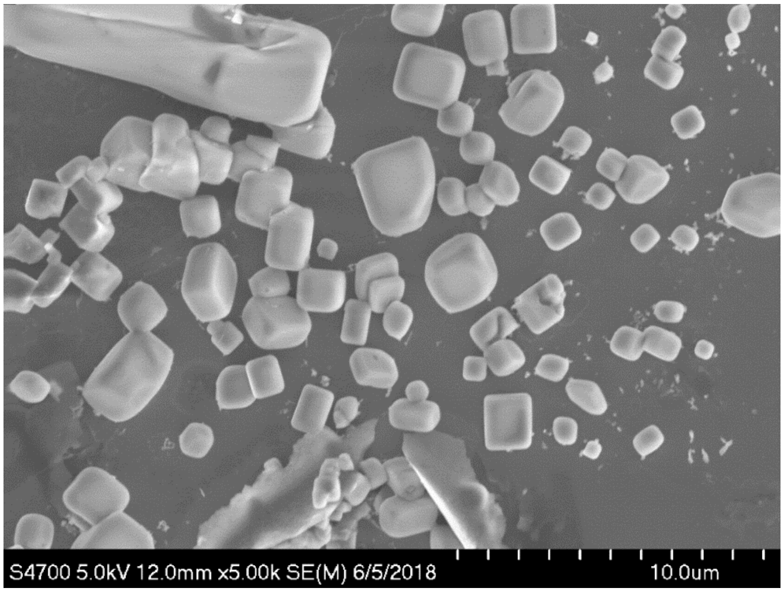

Fig. 54 SEM image of AuNR-TiO_2 core-shell

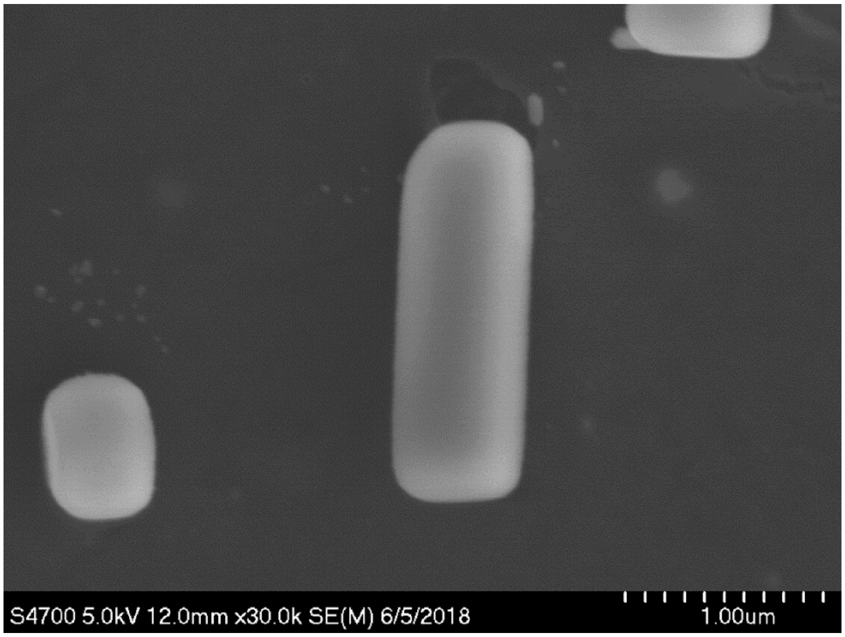

Fig. 55 SEM image of AuNR-TiO_2 core-shell

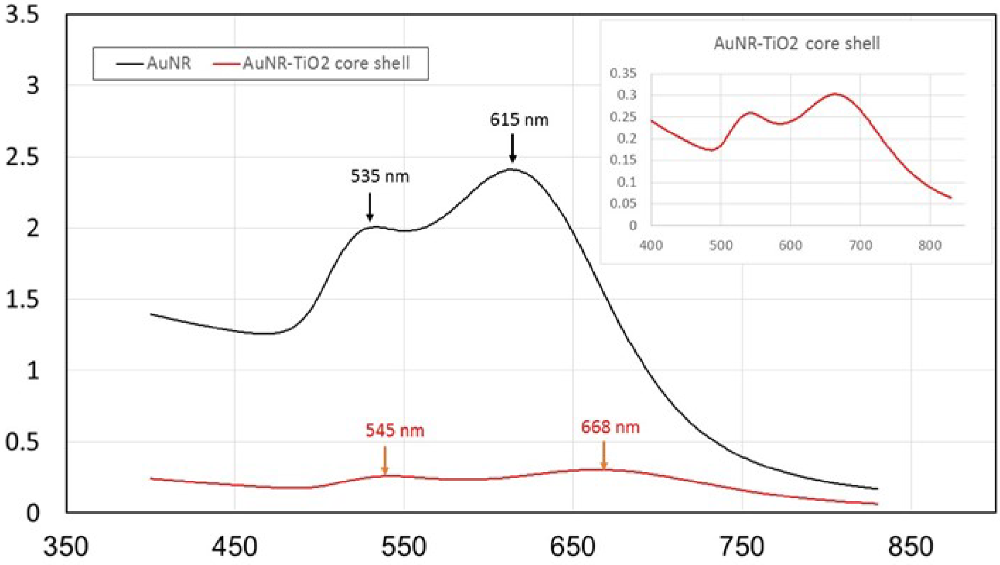

Fig. 56 UV-Vis spectrum of AuNR-TiO_2 core-shell

Methods to optimize this synthesis approach to favor AuNR-TiO_2 dumbbells formation were conducted by controlling the CTAB concentration. In this study, five CTAB concentrations were chosen: 6.93, 12.95, 27.12, 49.17, and 83.76 mM. The corresponding AuNR-TiO_2 dumbbells seen in the SEM, as outlined in Table 2, are shown in Fig. 57. At a CTAB concentration of 6.93 mM, TiO_2 is mixed between fully coated onto the AuNR and selective coatings onto both ends of AuNRs like dumbbells. In the range of 12.92 and 49.17 mM of CTAB, AuNRs are fully coated with TiO_2. However, at 83.76 mM of CTAB concentration TiO_2 is only partially coated onto the AuNRs. UV-Vis analysis for AuNR-TiO_2 dumbbells according to variation of CTAB concentrations is shown in Fig 58 and comparative TSPR: LSPR ratios are shown in Fig. 59. As seen in the AuNR-TiO_2 core-shell, both TSPR and LSPR peaks are red shifted. Interestingly, LSPR's red shift is more significant and the higher CTAB concentration of 27.12 mM LSPRs is blue shifted again.

Table 2 AuNR-TiO_2 structure change according to CTAB concentration

Sample no.	CTAB concentration (mM)	TiO_2 coating onto AuNR
1	6.93	Full coating or dumbbell
2	12.95	Full coating
3	27.12	Full coating
4	49.17	Full coating
5	83.76	Partial coating

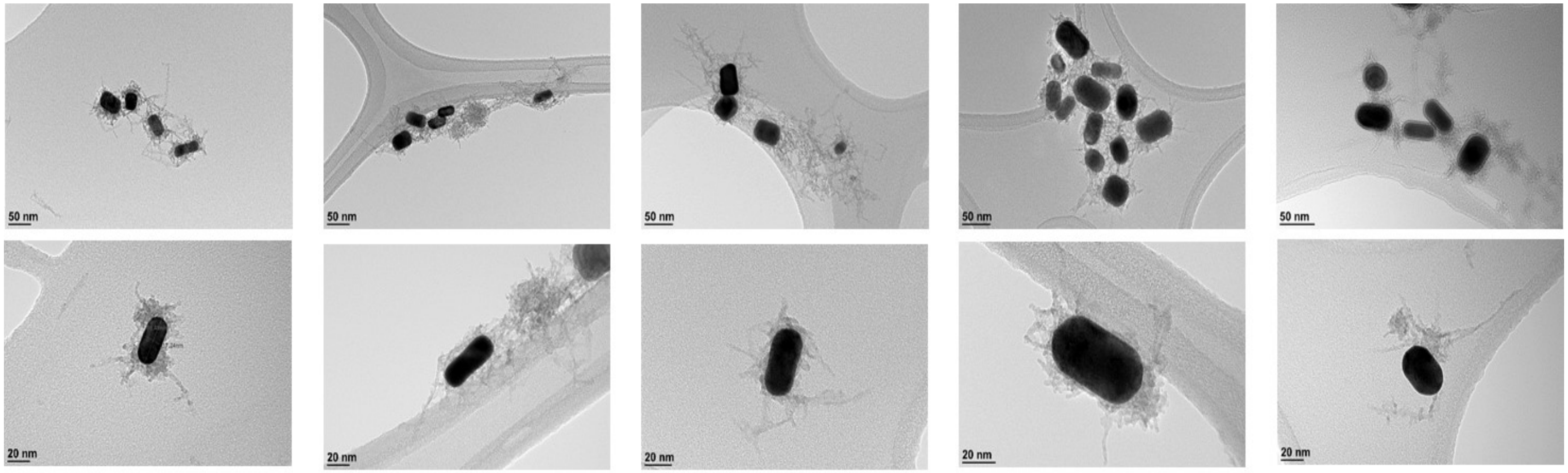

CTAB : 6.93mM CTAB : 12.95mM CTAB : 27.12mM CTAB : 49.17mM CTAB : 83.76mM

Fig. 57 BF-TEM images of AuNR-TiO_2 dumbbell according to the change of CTAB concentration

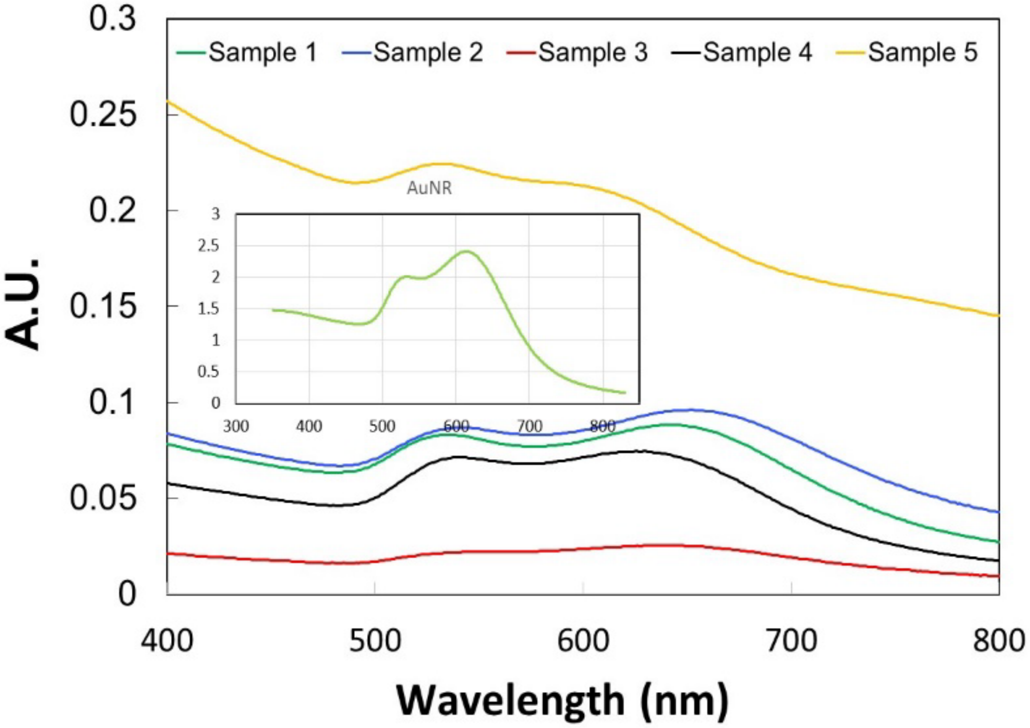

Fig. 58 UV-Vis spectra of AuNR-TiO$_2$ dumbbells according to CTAB concentration

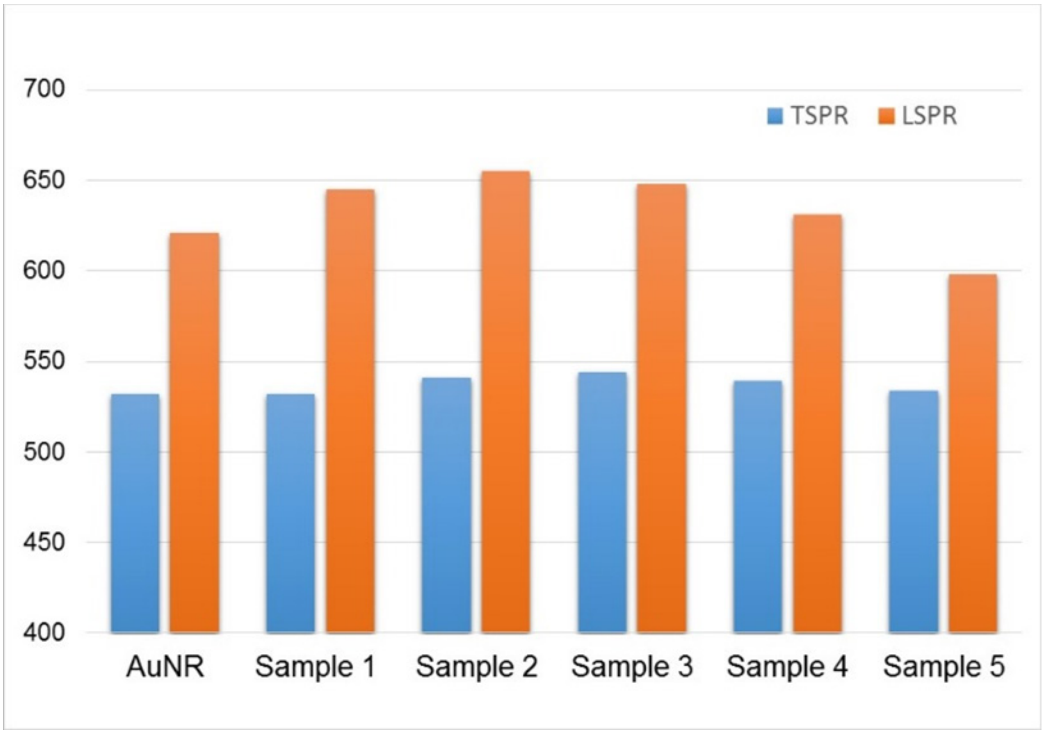

Fig. 59 TSPR and LSPRs of AuNR-TiO$_2$ dumbbells according to CTAB concentration

It has been reported that TiO_2 nanoparticles (NPs) can be selectively anchored on the tips of AuNRs, where the thickness of TiO_2 clusters were increased with the adding of $NaHCO_3$.[9] When the amount of $NaHCO_3$ is of sufficient concentration, the nanostructures can change from Au/TiO_2 NPs to AuNRs-TiO_2 NP structures and from Au/TiO_2 NPs to AuNRs-TiO_2 NPs core-shell structures. Cassaignon et al.[34] reported titania nanoparticles that were synthesized by hydrolysis and oxidation of $TiCl_3$ in an aqueous medium. The TiO_2 synthesis via the hydrolysis of Ti(III) proceeds in two steps: a condensation step and an oxidation step, which can be separated or simultaneous and they could take place in both orders.[34] The importance of weak acidity ($2 < pH < 6.5$) at 60 °C on the precipitation was underlined in this study to effectively prepare anatase species. Depending on the pH, brookite (diamond-shape platelets) or rutile (rods) was obtained under highly acidic and near-neutral conditions, respectively. Moreover, the control of the $TiCl_3$ hydrolysis allowed the synthesis of uncommon morphologies of TiO_2 nanoparticles, especially rods of anatase, which are small square platelets (3 nm) of rutile.[34]

The mechanism of the enhanced photocatalytic water splitting efficiency is proposed as follows. When a visible light irradiation source was used, AuNRs acted as light harvesters due to their LSPR effect. The hot electrons excited from AuNRs were injected via Schottky junction into the conduction band of tip-coated TiO_2 NPs. Then the sides of AuNRs were involved in the generation of H_2, while the departing holes were consumed by CH_3OH. At the same time, part of electron energy was transferred back from TiO_2 to AuNRs. Under UV light irradiation, TiO_2 NPs were excited to generate electrons (e^-) and holes (h^+); the electrons in the conduction band of TiO_2 NPs were injected to AuNRs due to the lower Fermi level of AuNRs. As a result, the individual positively charged TiO_2 NPs region and negatively charged AuNRs region were formed. Subsequently, the H_2 was produced on the surface of AuNRs. Under natural sunlight irradiation, the directed spatial partition of the charge carrier also formed in the presence of the Au/TiO_2 NPs photocatalyst; however, the AuNRs acted as an H_2-production reaction site. AuNR-TiO_2 dumbbell synthesis results have been studied according to the change of AuNR shape as shown in Fig. 60. In Fig. 60, most of the shapes can be synthesized to AuNR-TiO_2 dumbbells; however, the larger diameter and higher apect ratio of AuNRs seem to be more efficient to synthesize AuNR-TiO_2 dumbbells. To synthesize AuNRs having larger diameter and higher aspect ratio with monodispersity, AuNRs were synthesized using the NaOL approach. The AuNRs produced had an aspect ratio of 5, and the corresponding AuNR-TiO_2 dumbbell structures are shown in Fig. 61.

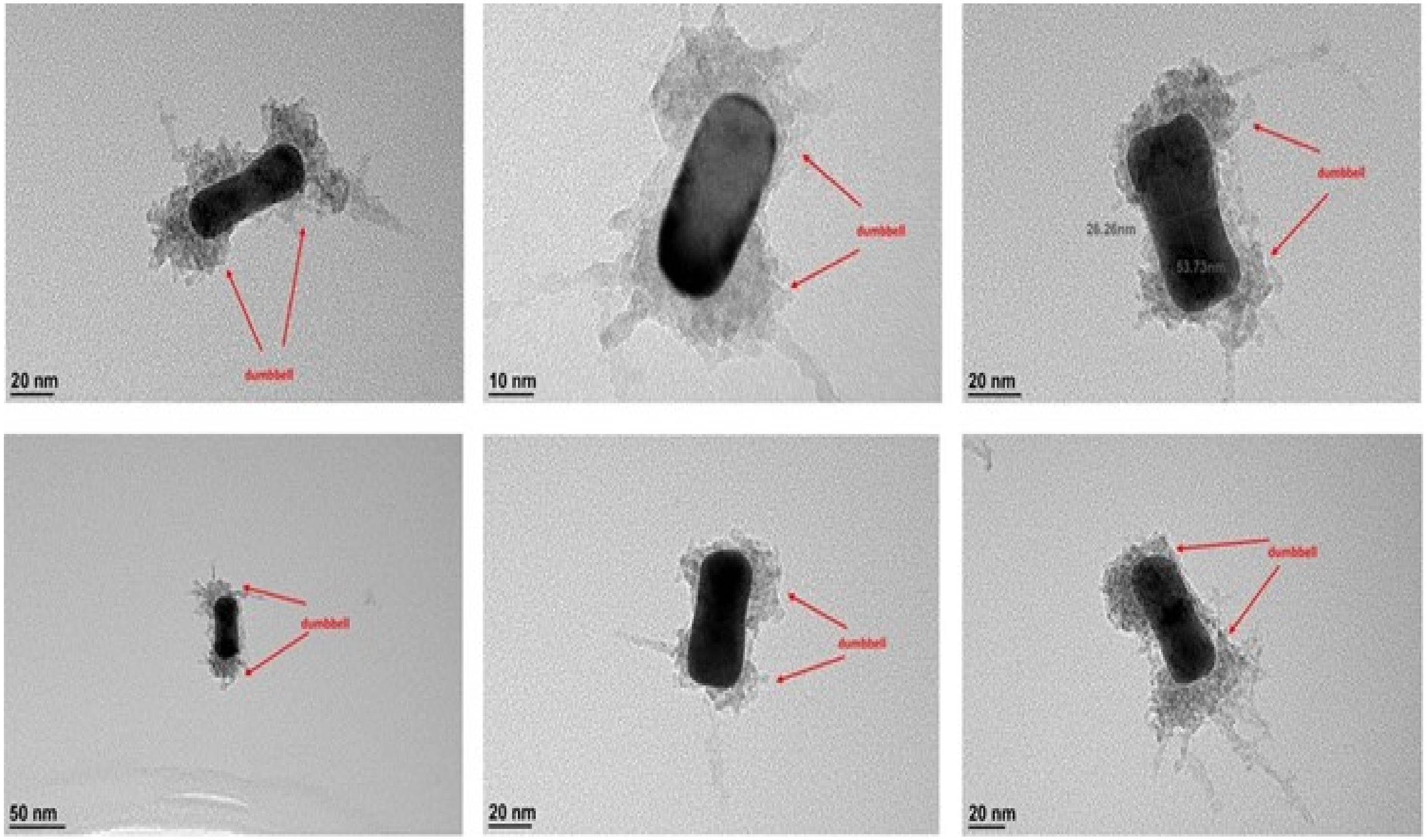

Fig. 60 BF-TEM images of AuNR-TiO_2 dumbbell according to AuNR shapes

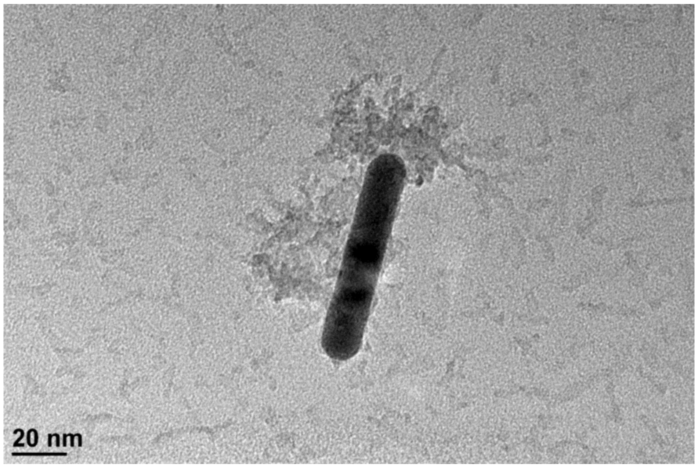

Fig. 61 BF-TEM images of AuNR-TiO_2 dumbbell on high aspect ratio (AR = 5)

Besides the CTAB-controlled AuNR-TiO_2 dumbbell synthesis, bicarbonate-controlled AuNR-TiO_2 dumbbell synthesis has been conducted. As the bicarbonate increased, AuNR was deformed as shown in Fig. 62.

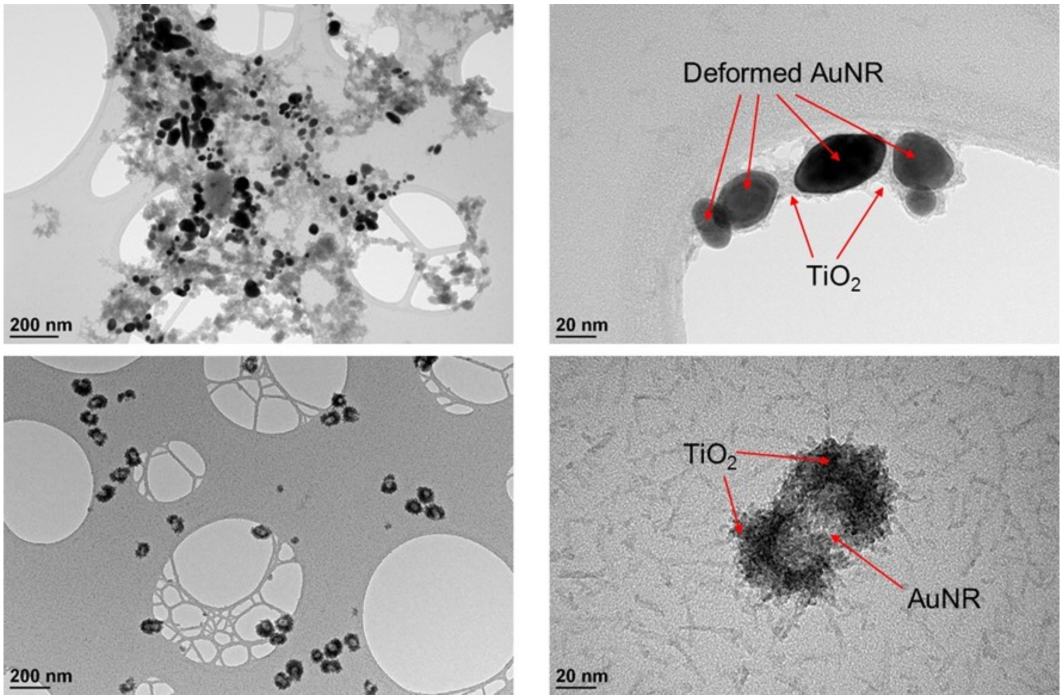

Fig. 62 BF-TEM images of AuNR-TiO_2 dumbbell synthesized by sodium bicarbonate concentration change

The results of Zeta potential measurements on sonicated, CYS coating and after graphene oxide coating on AuNR (diameter of 32 nm) are shown in Fig. 63. The as-received graphene oxide shows almost neutral Zeta potential at the beginning and then after 6 h of sonication, the potential dropped to –1.8 mV, which is believed to be the change of functional group on the graphene oxide surface during sonication. To increase the positive charge on the surface of AuNR, CYS is adsorbed on the nanorod surface. After CYS coating, the Zeta potential of AuNR was +0.1 mV, which is a lower Zeta potential change than expected. Finally, after obtaining the AuNR-CYS-GO hybrid, a Zeta potential of –0.1 mV is obtained. Likely, if the CYS concentration is increased during the coating process, this Zeta potential change could be higher than these results, which could make the AuNR more highly positively charged. Charge potentials that are evident here are much lower than those achieved with electrostatic polymer functionalization.[35]

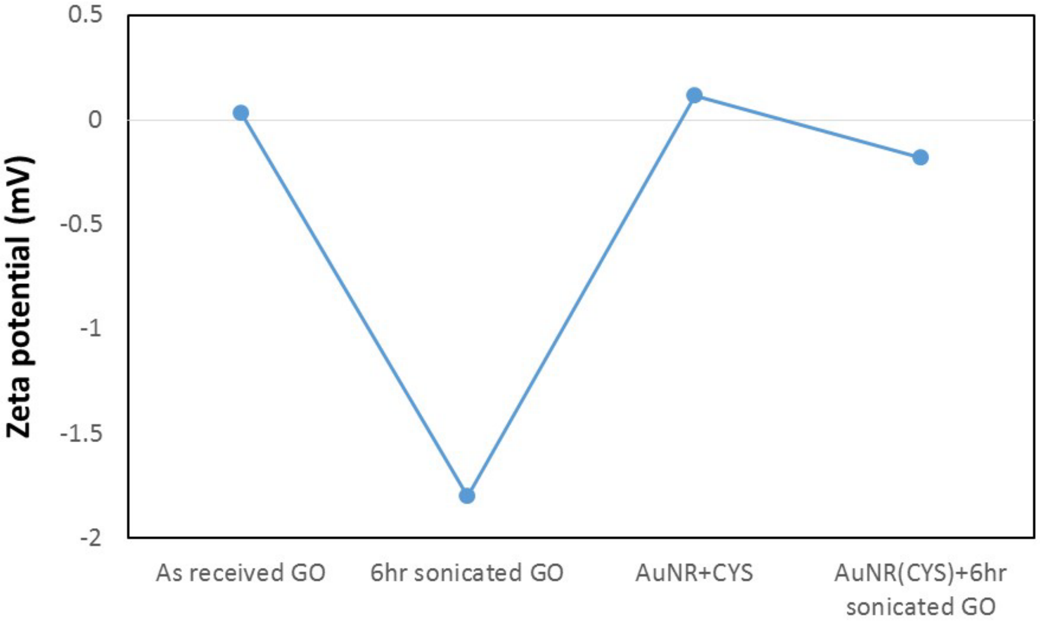

Fig. 63 **Zeta potential variation for AuNR (32 nm) according to the surface treatment**

3.7 AuNR-nGO

To synthesize AuNR wrapped with nGO, two methods have been employed to include the AuNR-CTAB and AuNR-PSS functionalization. CTAB is a well-known surfactant for AuNR synthesis due to the positive charge of CTAB. The AuNR is positively charged in this case, but the CTAB's electronegativity is lower than PSS. Figures 64 and 65 show the comparison of electrostatically charged AuNRs based on both the CTAB and PSS functionalization used to synthesize AuNR-nGO. In these images, large flakes of graphene sheets are still present around the rod structures. Based on these results, it can be concluded that a smaller size of graphene oxide for evenly wrapping of the gold nanoparticles is needed.

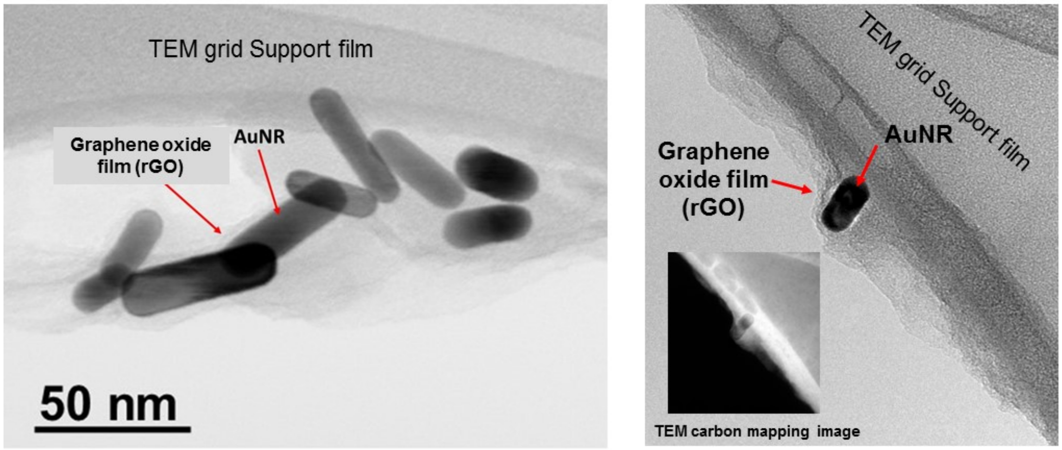

Fig. 64 BF-TEM images of AuNR-rGO with CTAB functionalized AuNRs. The inset shows an EFTEM carbon–K edge elemental map.

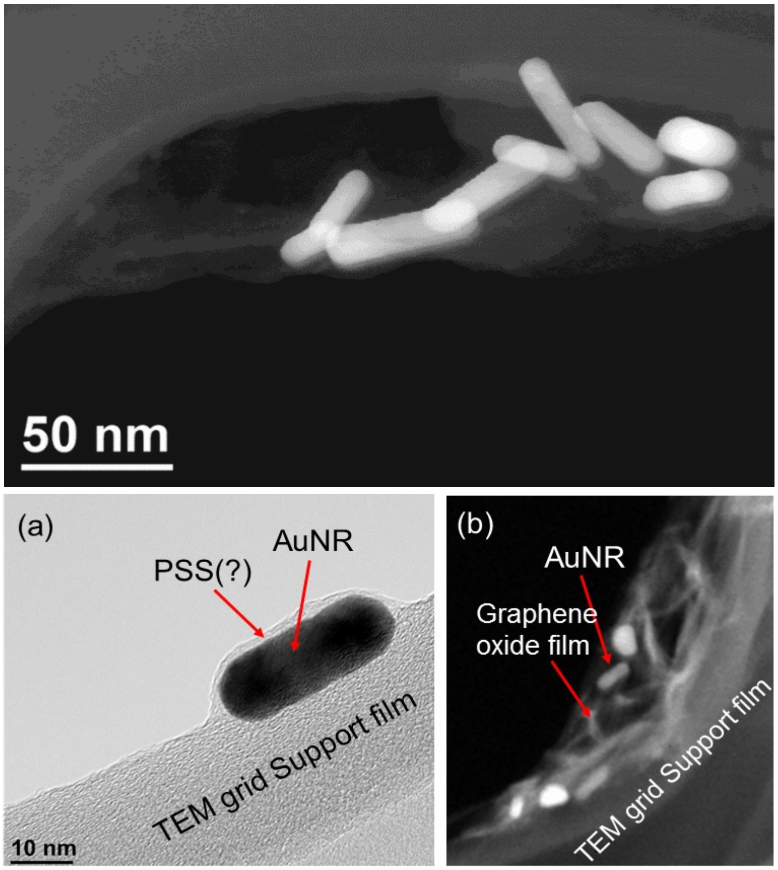

Fig. 65 STEM-HAADF image (top), BF-TEM image (bottom left), EFTEM C-K elemental map image (bottom right) of PSS-coated AuNR-rGO by PSS method

To optimize AuNRs coated with nGO, AuNR synthesized with CTAB and nGO synthesized by oxidation were first used. The BF-TEM images of AuNR-nGO are shown in Fig. 66. It is difficult to recognize AuNR; however, some evidence of nGO crystalline structure can be seen at higher magnification. During oxidation of graphene oxide, strong chemicals and oxidant have been applied; therefore, any residual $KMnO_4$ and hydrazine could result in the dissolution of AuNRs.

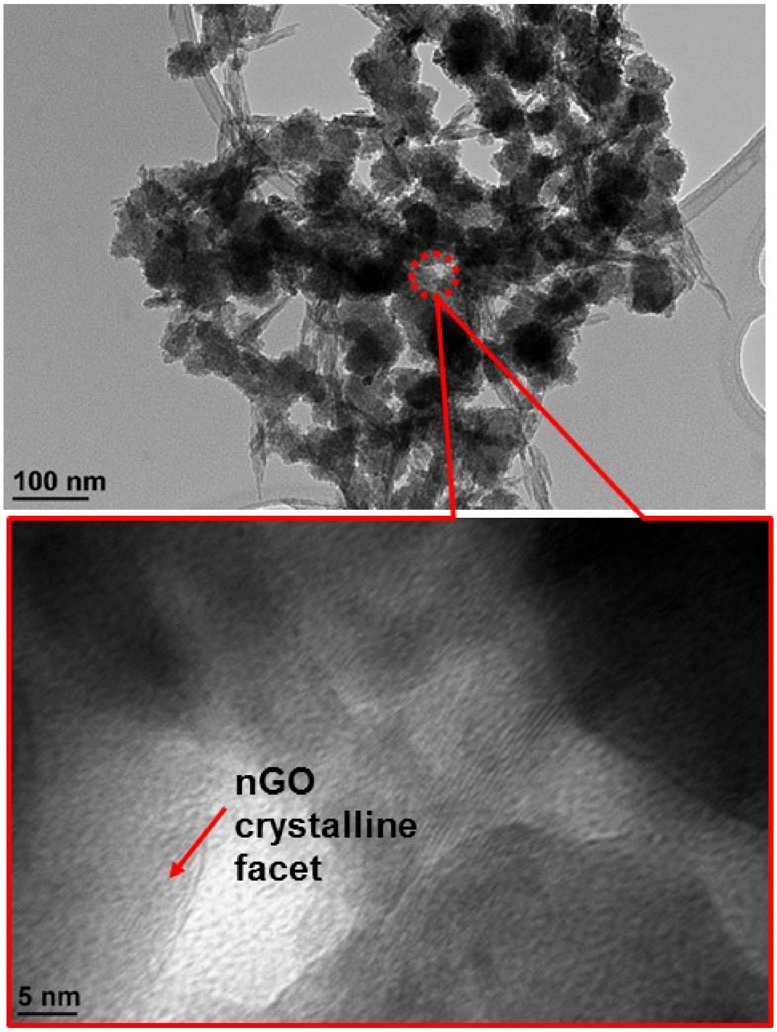

Fig. 66 BF-TEM images of AuNR-nGO (AuNR was synthesized with CTAB and nGO synthesized by oxidation)

To reduce chemical contaminations, nGO synthesized by sonication in DI water was used. The BF-TEM image of AuNR-nGO prepared with these materials is shown in Fig. 67. Compared to the previous oxidation method, nGO synthesized in DI water with several hours of sonication requires no additional neutralization or lyophilization. Furthermore, sonication induces more defects in the graphene structure, creating dangling bonds that ultimately increases the graphene oxide's negative charge. Functional groups generated during the sonication makes graphene oxide more negatively charged and it enhances the adhesion between AuNR and nGO. However, as shown in Fig. 68, there are still big chunks of graphene oxide single layers that have not been broken apart during sonication.

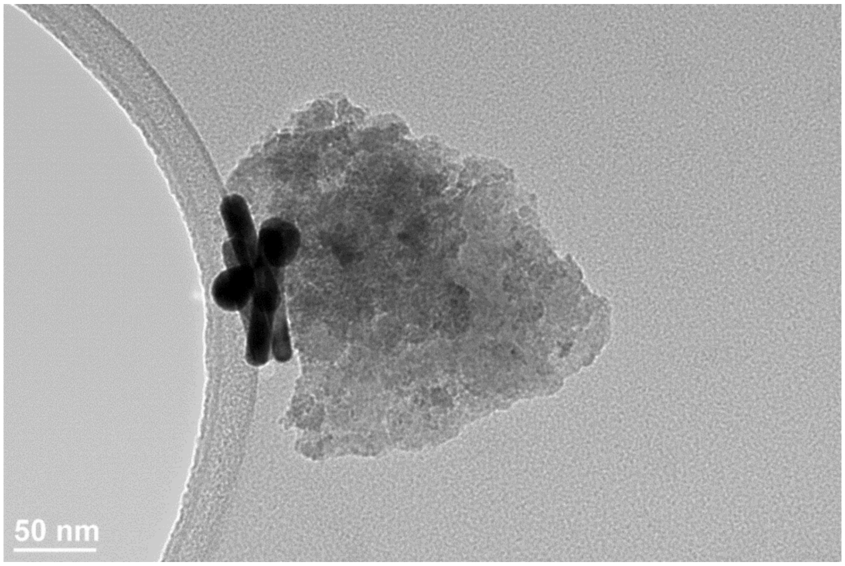

Fig. 67 BF-TEM images of AuNR-nGO (AuNR was synthesized with NaOL and nGO synthesized by sonication)

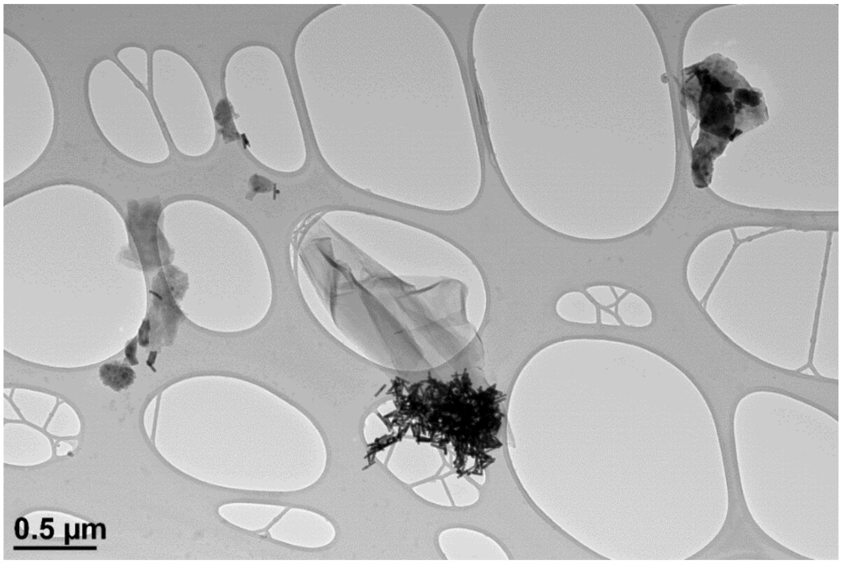

Fig. 68 BF-TEM images of AuNR-nGO, highlighting attachment to NGO sheets

In conclusion, to make monodispersed nGO (< 10 nm or so), previously synthesized nGOs are inappropriate for AuNR-nGO synthesis. The solution to this problem was to use GQDs. GQDs have a very monodispersed size distribution of less than 10 nm, which is believed to be optimal for AuNR-nGO synthesis.

3.8 AuNP-rGO-CuO

Urchin-like CuO has been synthesized by microwave-assisted hydrothermal synthesis within 10 min using $CuCl_2/NH_4OH$ aqueous solution.[36,37] Current efforts were unsuccessful in creating the proposed Cu_2O structures through this methodology; however, catalytic properties of the created CuO structures were explored. Urchin-like or nanostar structures have been well reported in plasmonic nanomaterials,[38,39] but are usually limited to oxides. The synthesized urchin-like 3-D CuO structures are shown in Fig. 69. The synthesis method of urchin-like 3-D CuO utilizes similar precursor materials as with the core-shell AuNR-nGO-Cu_2O; however, the hydrothermal processing alters the growth mechanism and subsequent physical structure. As shown in Fig. 69, CuO grew on the surface of graphene oxide shell like an urchin's thorns. UV-Vis measurement was conducted during the synthesis (Fig. 70). At first, the unique and intrinsic peak of AuNP is shown at around 530 nm (P1). After the graphene oxide was reduced to the rGO form onto AuNP, P1 disappears. After final CuO coating, P2 and P3 peaks are observed, as seen in UV-Vis spectra of AuNR-nGO-CuO. These P2 and P3 peaks are attributed to be the CuO's plasmonic-coupling relationship with Au. A preliminary conclusion is that CuO can be used as a control agent on AuNR or AuNP to alter its absorbance as well as to increase the absorbance in the visible light spectrum.

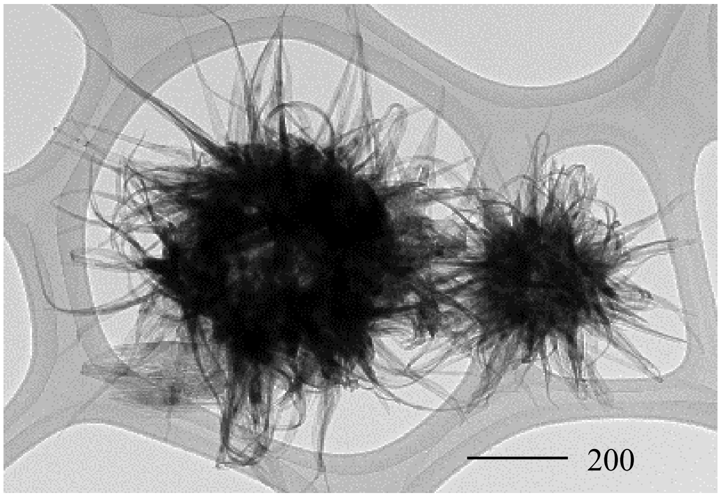

Fig. 69 TEM image of AuNP-rGO-CuO

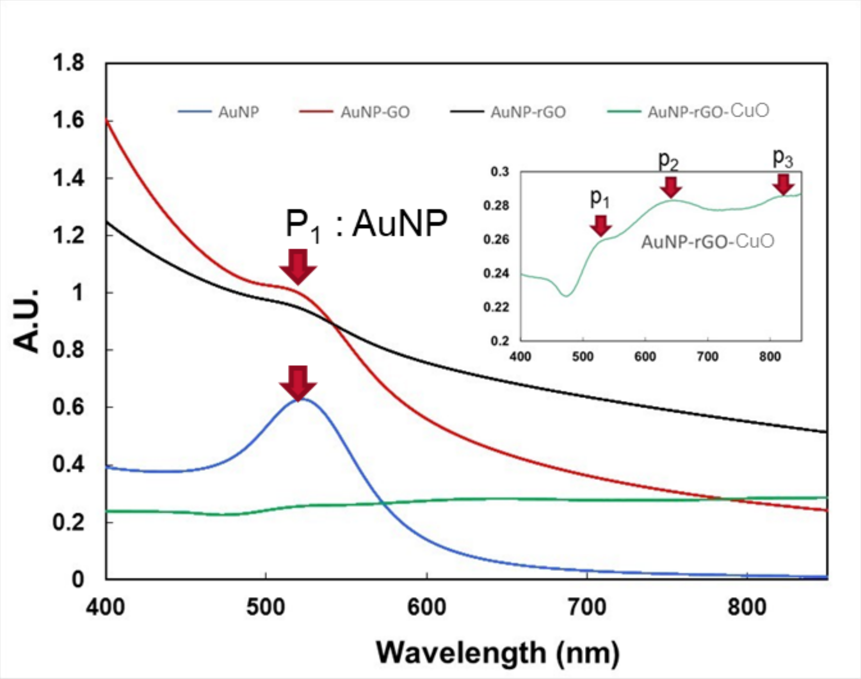

Fig. 70 UV-Vis spectra of AuNP, AuNP-GO, AuNP-rGO, and AuNP-rGO-CuO (P_2 and P_3 peaks in UV-Vis spectra are ascribed to urchin-like structure of CuO)

Because of the UV-Vis spectra results, band-gap variation of AuNR-rGO-CuO was investigated using the Kubelka-Munk plot method as shown in Fig. 71. At first, the band gap of the prepared AuNP is approximately 1.9 eV. After graphene oxide, rGO, and CuO coating cumulatively onto AuNP, the band gaps seem to be decreasing. The band gap in Fig. 71 is determined by linearly extrapolating a line to the X-axis from the portion of the curve before inflection point. From the Kubelka-Munk plot, we should expect higher photocatalytic efficiencies in the sequence of coatings from graphene oxide to rGO and CuO.

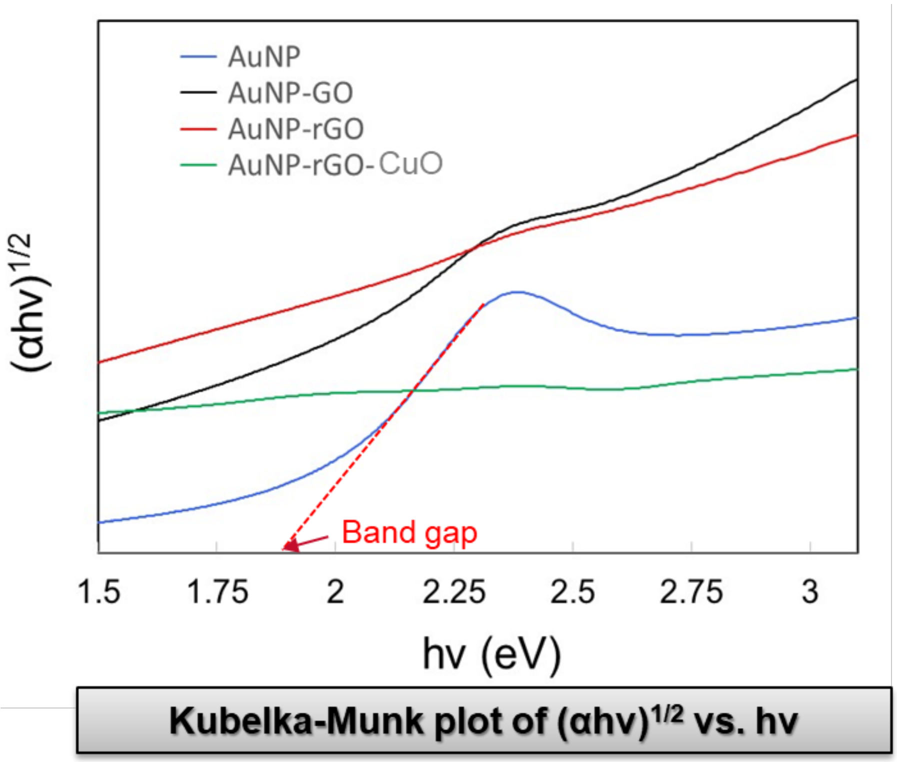

Fig. 71 Kubelka-Munk plot of $(\alpha h\nu)^{1/2}$ vs. hν

To examine urchin-like 3-D CuO in detail, STEM-HAADF, selected area diffraction (SAD), and X-ray energy dispersive spectroscopy (XEDS) analyses were done. In the STEM-HAADF image shown in Fig. 72, most of the 3-D urchin-like structure shows bright contrast indicating it having a uniform average atomic number, while the core is the brightest due to the thickness of the particle there. Although the intended phase was Cu_2O, the SAD pattern and XEDS spectrum shown in Figs. 73 and 74, respectively, show only CuO. Further investigation is required to isolate the Cu_2O form in future work. It should be noted that only trace amounts of graphene and Au were found.

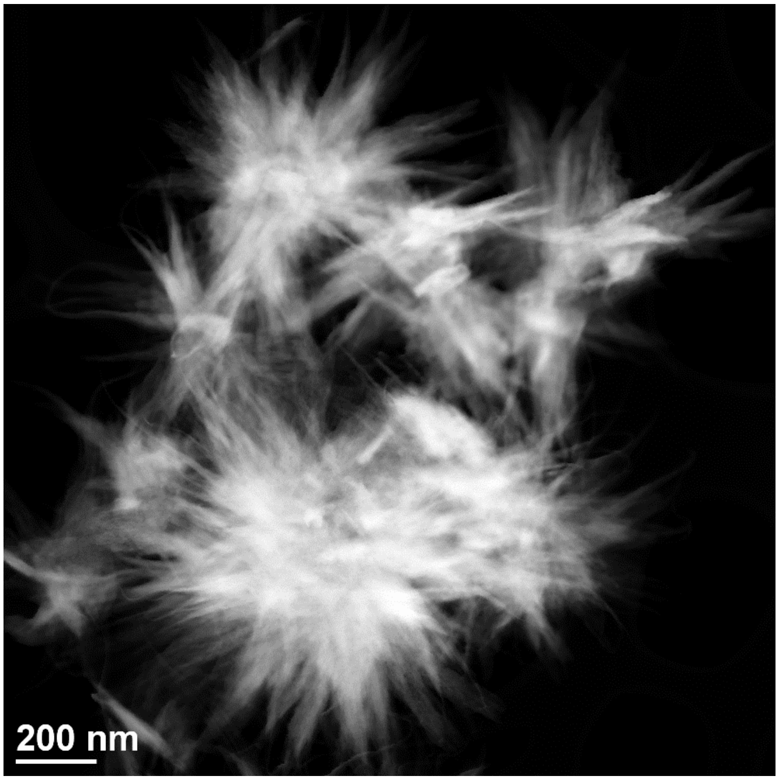

Fig. 72 STEM-HAADF image of CuO urchin

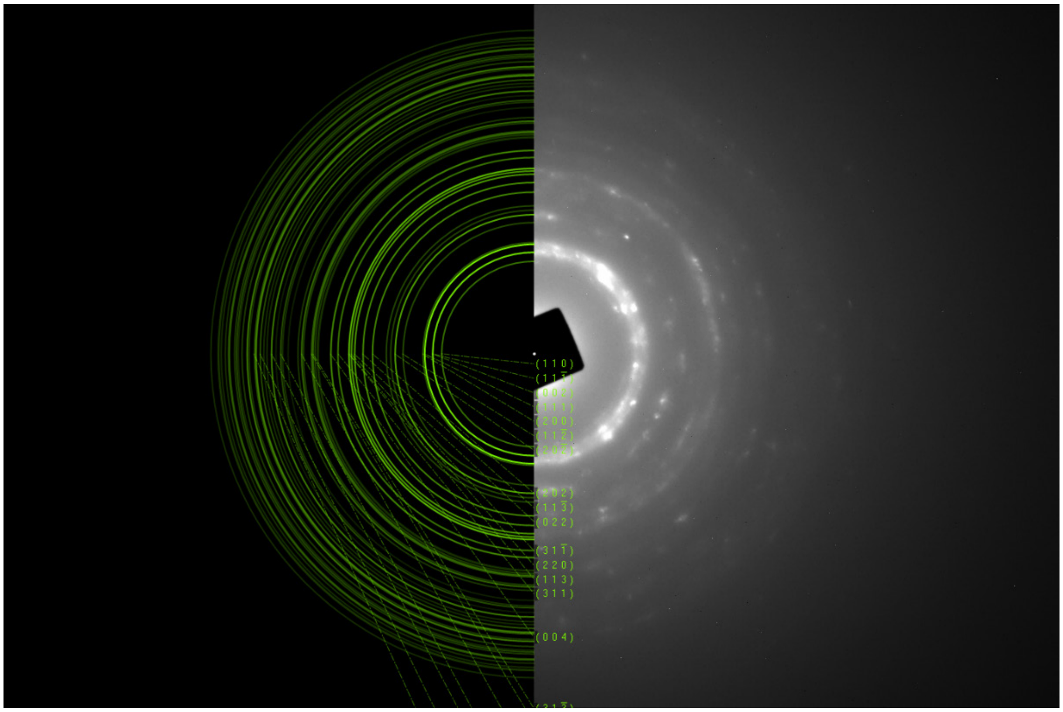

Fig. 73 TEM SAD pattern for CuO urchin

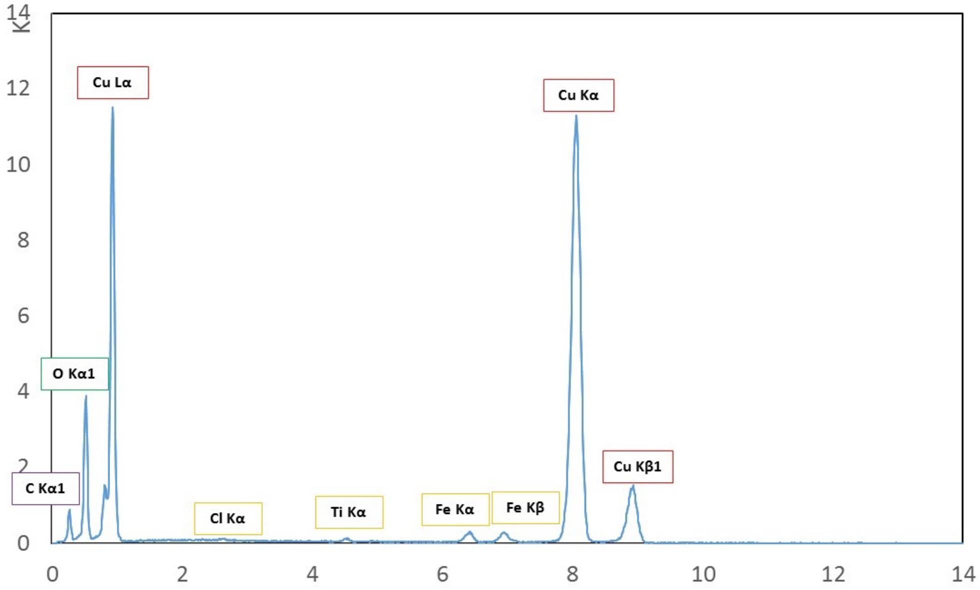

Fig. 74 XEDS spectra on CuO urchin

The possible synthesis mechanism of urchin-like 3-D CuO that is proposed is shown in Fig. 75. At first, positively charged AuNPs are wrapped with negatively charged graphene oxide and then graphene oxide is reduced with hydrazine and ammonia monohydrate. During reduction, hydrazine and ammonia monohydrate traces are present and etch the AuNP, which leaves the graphene oxide hollow microsphere as the nucleation site for CuO urchin thorns.

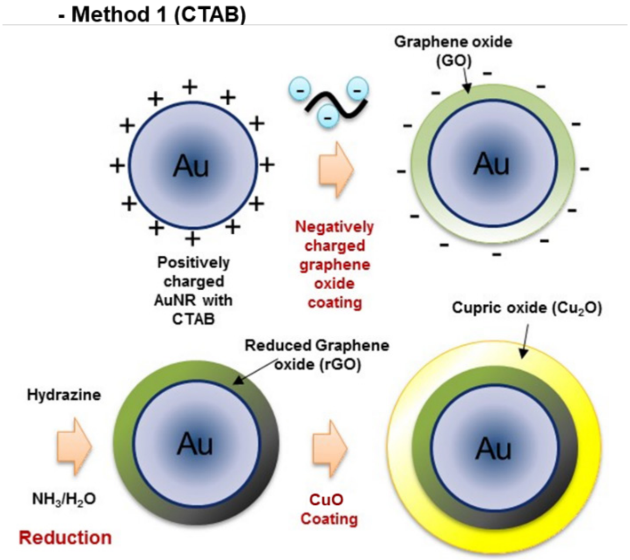

Fig. 75 Urchin-like rGO-Cu_2O hollow microsphere synthesis mechanism

In the final CuO growth stage, the remaining hydrazine and ammonia monohydrate could create an environment to grow the urchin structure. In this study, sea urchin-like 3-D CuO was successfully synthesized without microwave assistance.

3.9 AuNR-TiO_2 Deformation Mechanism under UV Irradiation

As discussed in the introduction, there are many controversies related to the plasmonic reaction of AuNR-TiO_2 under UV and visible light irradiation. The reduction of $AgNO_3$ was used to determine whether AuNR-TiO_2 was producing the desired plasmonic reaction. First, AuNR-TiO_2 dumbbells were synthesized, then $AgNO_3$ was added to the solution, and UV light was irradiated to the solution. After UV irradiation of the solution, AuNR deformed irregularly.

As shown in Fig, 76, it is known that AuNRs are deformed by heat. This implies that during UV irradiation of AuNR heat was generated by the photocatalytic reaction. In the case of hot electrons generated from TiO_2, phonons are generated and heat can be transferred to the gold core. However, in case of electrons originated from the excitation of LSPR modes on Au nanoparticles, no measurable quantity of heat could be detected.

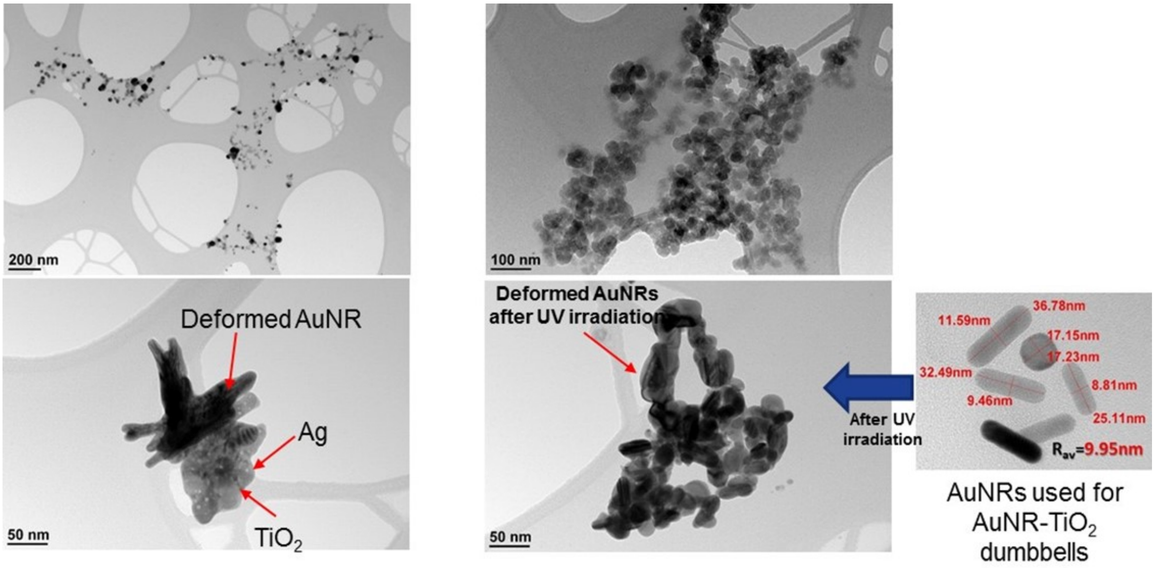

Fig. 76 BF-TEM images after UV irradiation showing deformed AuNRs. The shape was changed to irregular from rod shape.

A preliminary conclusion is that AuNR is thermally unstable during the photosynthesis and that in order to enhance the stability of AuNR, appropriate measures must be made to AuNR to increase the efficiency of the photocatalytic reaction.

3.10 Mechanism Study on AuNR-TiO_2 Core-Shell, AuNR-TiO_2 Dumbbell, and AuNR-rGO-TiO_2 Dumbbell

Possible photocatalytic mechanisms for AuNR-TiO_2 core-shell, AuNR-TiO_2 dumbbell, and AuNR-rGO-TiO_2 dumbbell under visible light are proposed and shown in Fig. 77.

In the case of AuNR-TiO_2 core-shells, hot electrons are generated under visible light irradiation of AuNR, jump up to the conduction band, and then move to the TiO_2. It is likely that these hot electrons reduce H^+ to H_2; meanwhile, H_2 oxidizes to H^+ at the AuNR surface. In the process of dissociation of a hot electron and a hot hole, the delayed hot electron moving over to TiO_2 can cause recombination of the hot electron and the hot hole. Because the AuNR is covered by TiO_2, the photocatalytic reaction activity and efficiency of the AuNR-TiO_2 core-shell is severely reduced.

Similar to the AuNR-TiO_2 core-shell model, a hot electron generated from the AuNR in the AuNR-TiO_2 dumbbell model can easily recombine with a hot hole; however, some surface of the AuNR is open for H_2 oxidation to H^+, which can enhance photocatalytic reaction compared to AuNR-TiO_2 core-shell model.

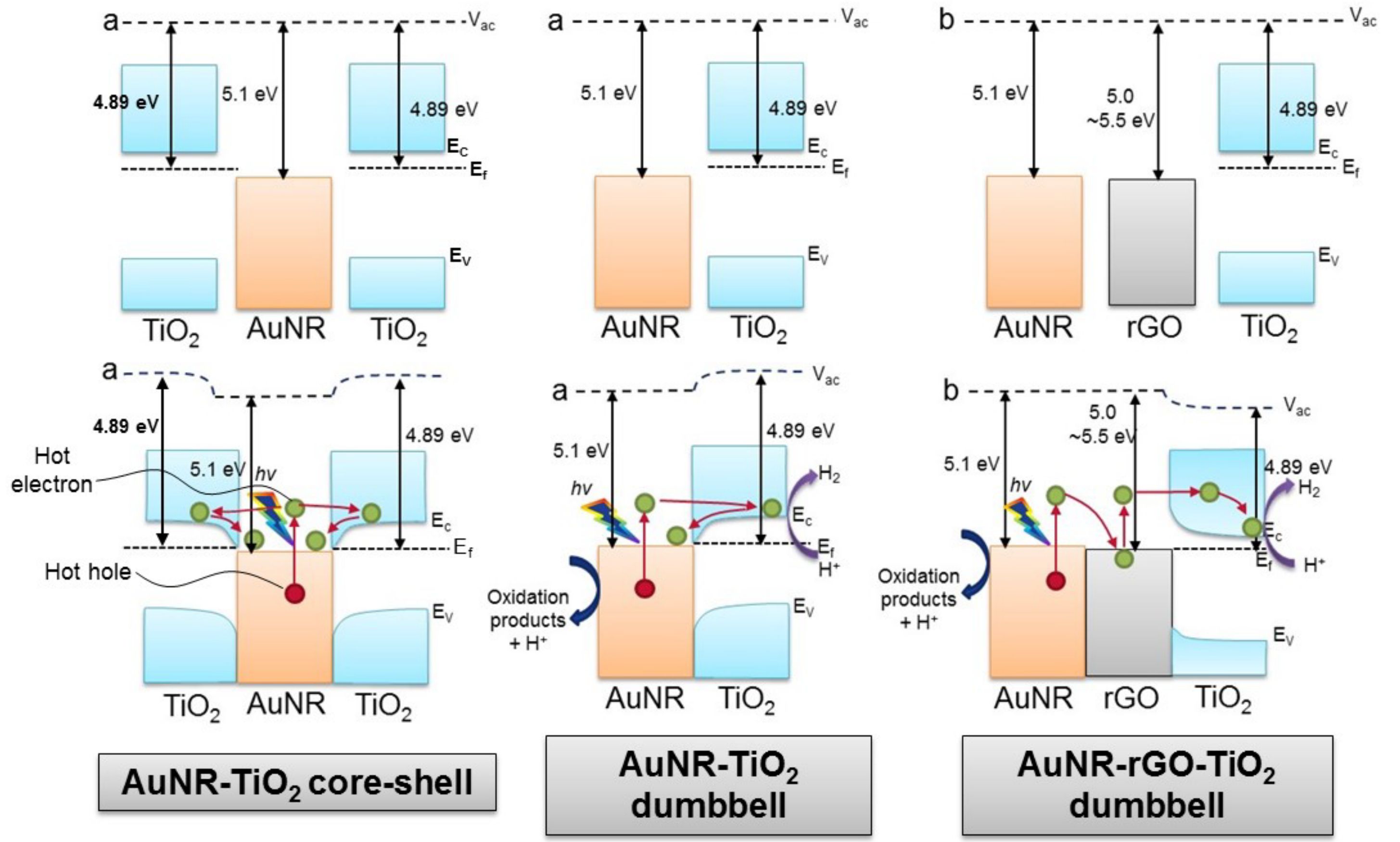

Fig. 77 Schematic illustrating the photo catalytic mechanism for AuNR-TiO_2 core-shell and dumbbell and AuNR-rGO-TiO_2 under visible light

In this respect AuNR-rGO-TiO_2 can provide the optimum photocatalytic reaction efficiency in terms of higher efficient hot electron separation from hot hole. It is well known that graphene has super high electron conductivity among any other materials. This super high electron conductivity allows the hot electron to move over to TiO_2 faster than other AuNR-TiO_2 core-shells and dumbbells, which enhances kinetics of the photocatalytic reaction. Therefore, AuNR-rGO-TiO_2 can be the optimum photocatalyst.

3.11 Photochemical Properties

To prove the theoretical mechanisms of the AuNR-TiO_2 core-shell, AuNR-TiO_2 dumbbell, and AuNR-rGO-TiO_2 dumbbell models as mentioned previously, the photoelectrochemical properties on as-received ITO, hollow Cu_2O, AuNR-TiO_2-1 (AuNR-TiO_2 core-shell simulated structure) and AuNR-TiO_2-5 (AuNR-TiO_2 dumbbell simulated structure), the linear sweep voltammograms and the I-t curves were measured in both UV and sunlight wavelength regions as shown in Fig. 78. Here it is shown that hollow microsphere Cu_2O produces 1.4 mA right after the UV light turns on. In the sunlight region, hollow microsphere Cu_2O shows 0.15 mA photocurrent.

Kim et al.^{40} reported that the sharp spike in the photocurrent during the on/off illumination cycles demonstrates the predominant transport of photogenerated electrons in the TiO_2 structure. Similar to the TiO_2 hollow microstructure, Cu_2O shows a sharp spike in the photocurrent during the UV radiation. However, AuNR-TiO_2-5 shows no sharp spike during the UV radiation, which means that at UV irradiation all samples show anodic photocurrent with cathodic photocurrent properties. In sunlight irradiation, all samples show anodic photocurrent properties. Photocurrent properties in sunlight irradiation have been investigated in more detail as shown in Fig. 79. AuNR-TiO_2-5 (simulating dumbbell structure) shows the highest photocurrent of 0.16 mA in sunlight irradiation which is four times and approximately 2.7 times higher than Cu_2O and AuNR-TiO_2-1 (simulating core-shell structure), respectively. This is clearly evidence of the proposed mechanisms on AuNR-TiO_2 core-shell and dumbbell as mentioned in Section 3.10.

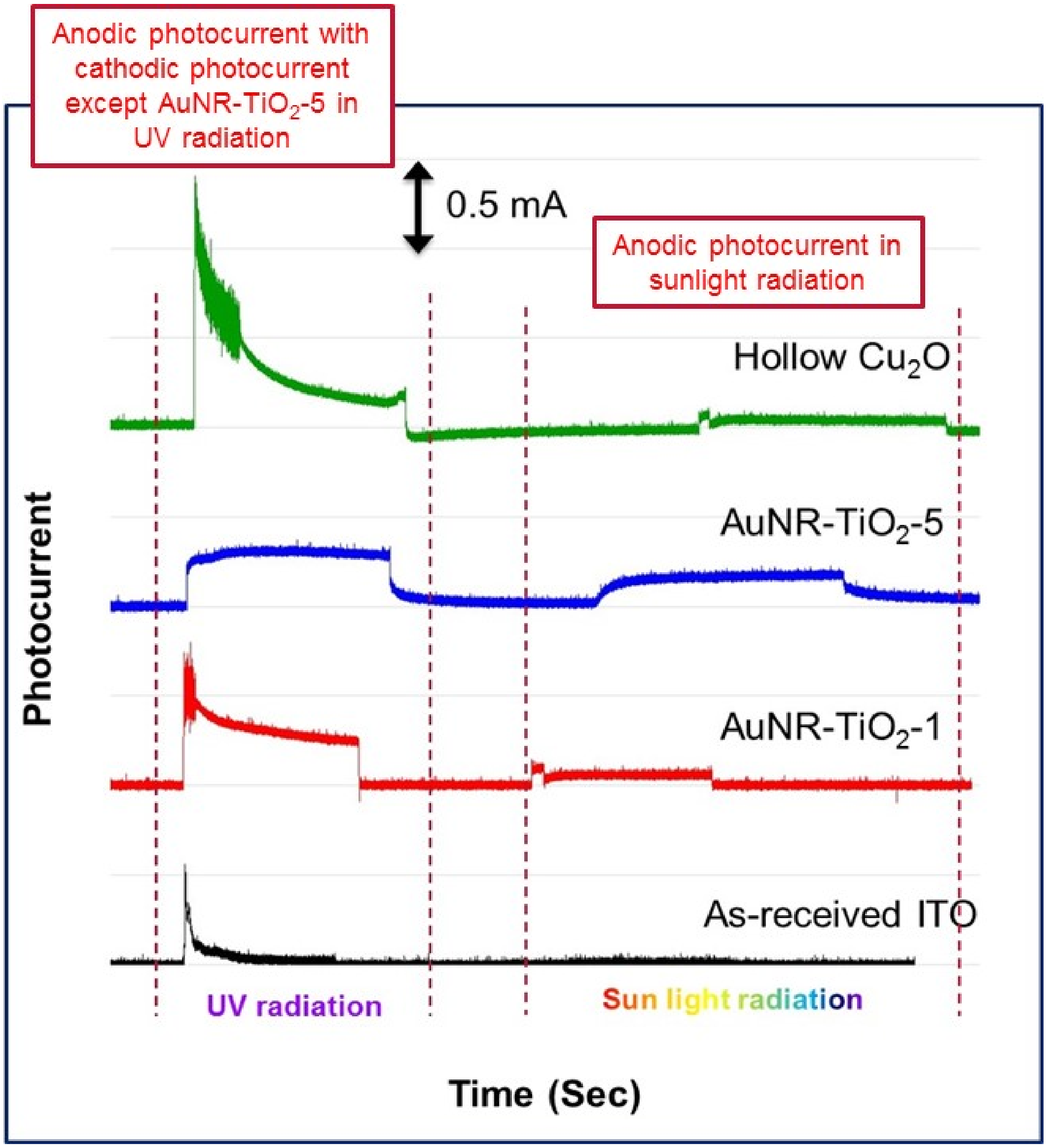

Fig. 78 Amperometric I-t curves of as-received ITO, hollow microsphere Cu_2O, AuNR-TiO_2-1, and AuNR-TiO_2-5 photoelectrodes

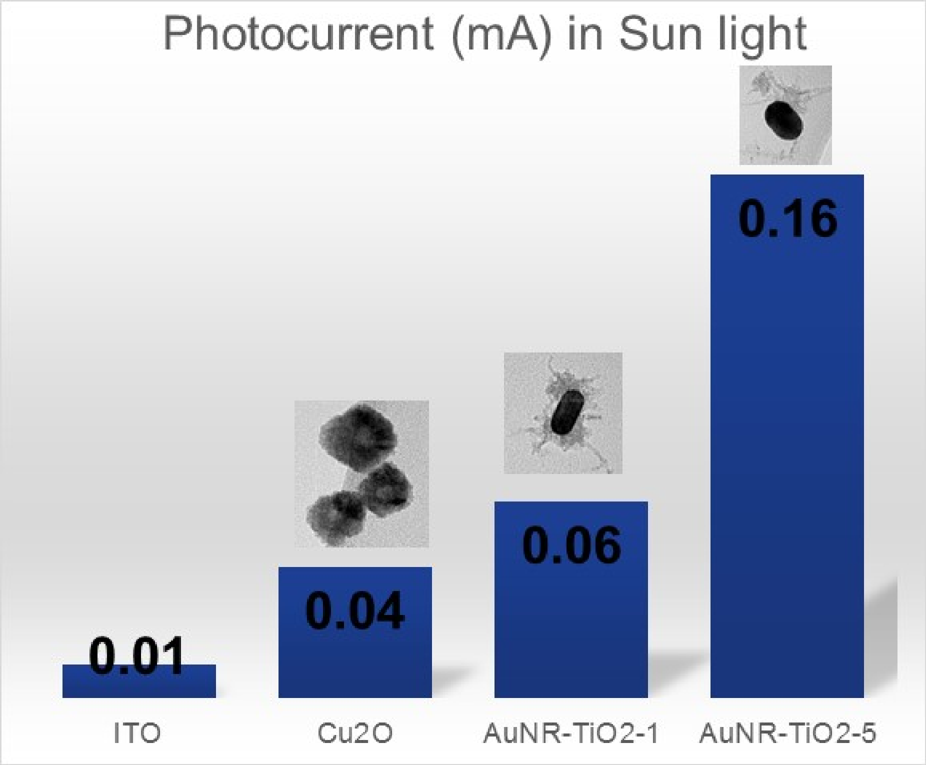

Fig. 79 Photocurrent of as-received ITO, hollow microsphere Cu_2O, AuNR-TiO_2-1, and AuNR-TiO_2-5 photoelectrodes in sunlight

As shown in Fig. 80, just after UV irradiation is turned on, Cu_2O shows the highest photocurrent of 1.4 mA. However, just before the UV irradiation is turned off, AuNR-TiO_2-5 shows the highest photocurrent of 0.28 mA. In terms of understanding the photocurrent properties exhibited by the samples in UV light on and off, further research is required. One conclusion can be drawn from the photocurrent measurements: the AuNR-TiO_2-5 sample shows excellent plasmonic photocatalytic efficiency in visible light irradiation. In addition, the AuNR-rGO-TiO_2 dumbbell configuration optimizes photocatalytic behavior for HER by separating oxidation and reduction. There can be pseudo-capacitance effects seen with photocurrent cyclic voltammetry tests; however, no pseudo-capacitance was seen in the cyclic voltammetry tests as shown in Fig. 81. For future studies, additional comparison with AuNR-nGO-TiO_2 samples would be interesting.

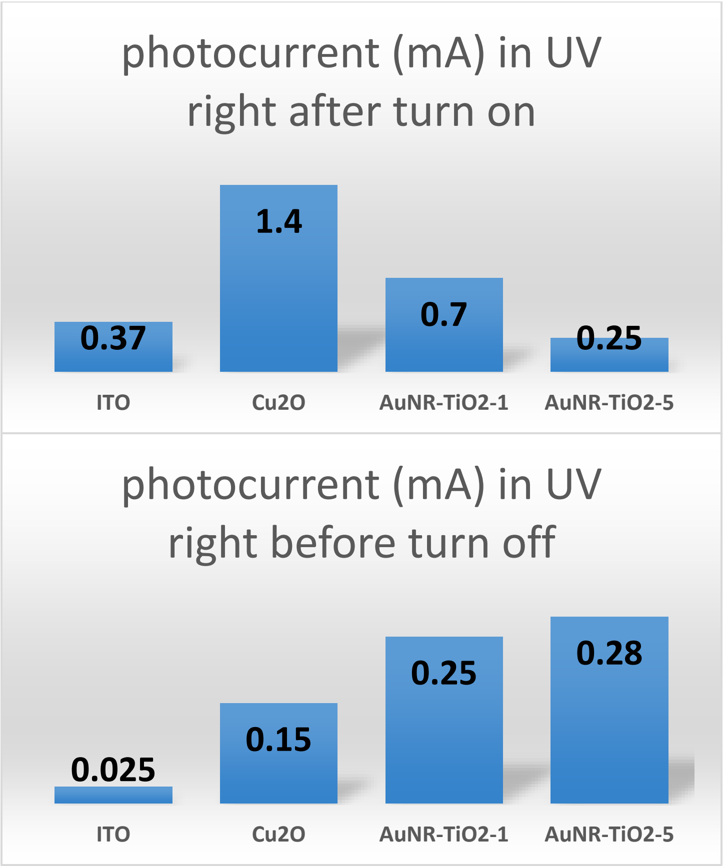

Fig. 80 Photocurrent of as-received ITO, hollow microsphere Cu_2O, AuNR-TiO_2-1, and AuNR-TiO_2-5 photoelectrodes in UV light

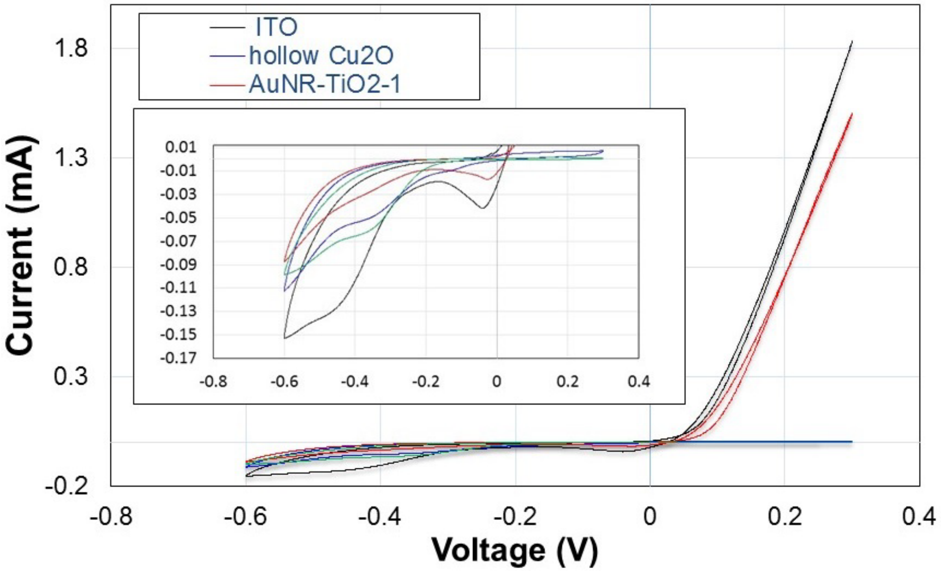

Fig. 81 Cyclic voltammogram on ITO, microsphere Cu_2O, and AuNR-TiO_2-1

3.12 MoS_2 and 3-D-rGO/MoS_2

Molybdenum disulfide (MoS_2) and 3-D rGO composite materials are known as a superior HER, oxygen evolution reaction (OER)/oxygen reduction reaction (ORR) catalysts.[41,42] In addition, they are expected to be considerably good photocatalysts. In this experiment, MoS_2/3-D rGO was synthesized by growing MoS_2 onto the surface of a 3-D rGO template. The BF-TEM images in Figs. 82 and 83 show the comparison of hydrothermally synthesized MoS_2 and the synthesized MoS_2/3-D rGO. When MoS_2 is synthesized in 3-D rGO, Fig. 83 shows that MoS_2 is successively synthesized on the surface of the 3-D rGO sheet.

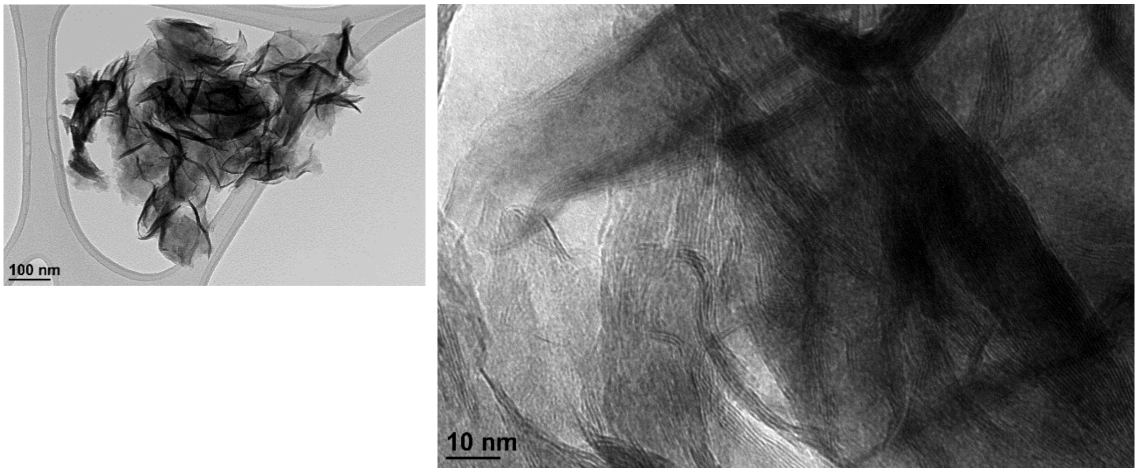

Fig. 82 BF-TEM images of MoS_2

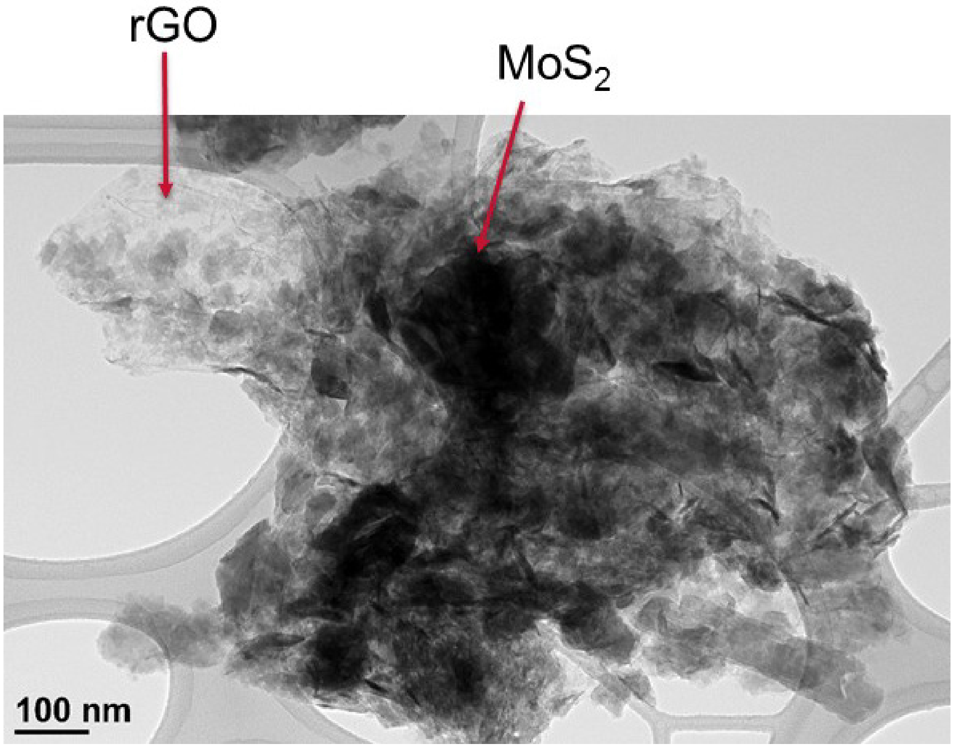

Fig. 83 BF-TEM image of 3-D rGO-MoS_2

HER characteristics of synthesized MoS_2 were measured by the well-known electrochemical Tafel plot method as shown in Figs. 84–86. The current density and the over-potential value were plotted, and the catalyst characteristics were obtained from the slope. The Tafel slope of synthesized MoS_2 was 291 mV dec^{-1}, which was somewhat higher than the generally known MoS_2 slope, 100 mV dec^{-1}. The lower the slope value, the better the catalyst characteristics. For standard catalysts such as Pt/C, the slope is within about 30 mV dec^{-1}.

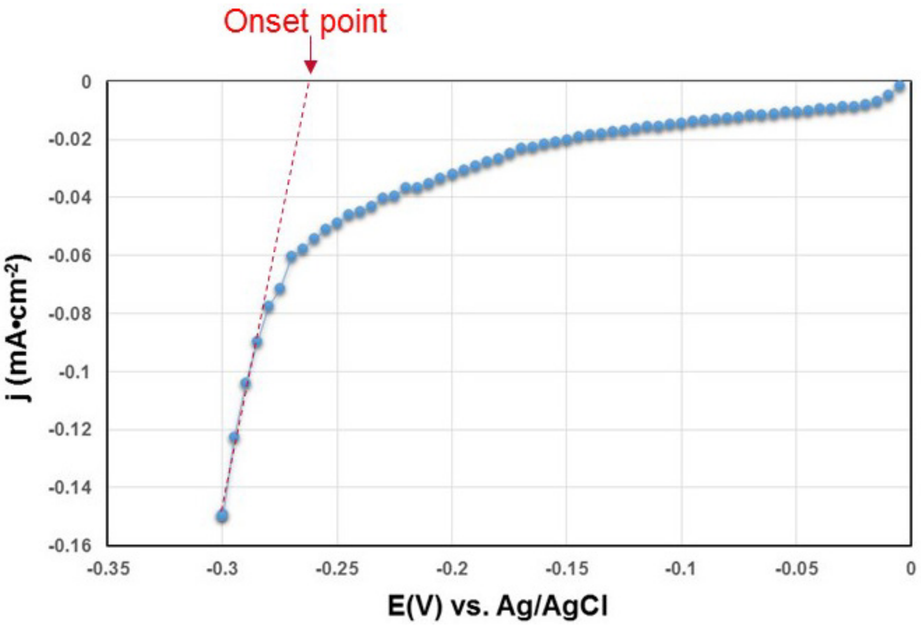

Fig. 84 Polarization curves for MoS_2 (Onset potential: ~ –260 mV)

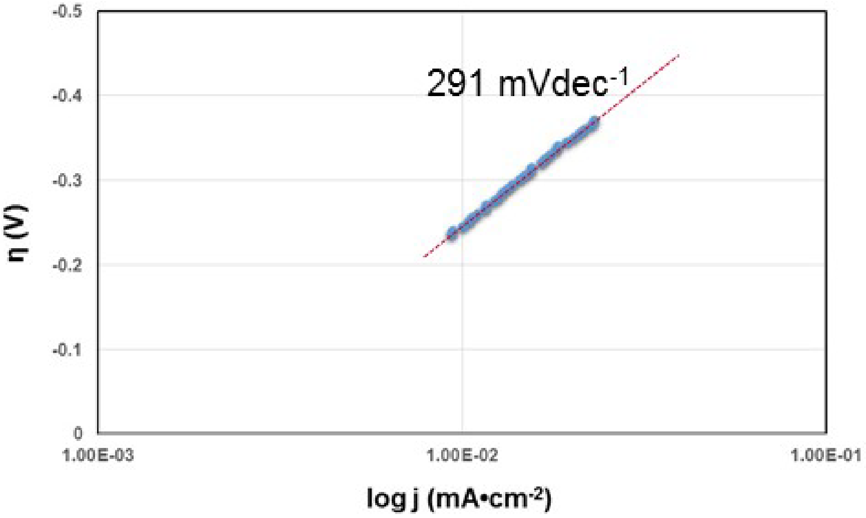

Fig. 85 Tafel plot of MoS_2 catalyst derived from the polarization curves (Tafel slope: 291 mV dec^{-1})

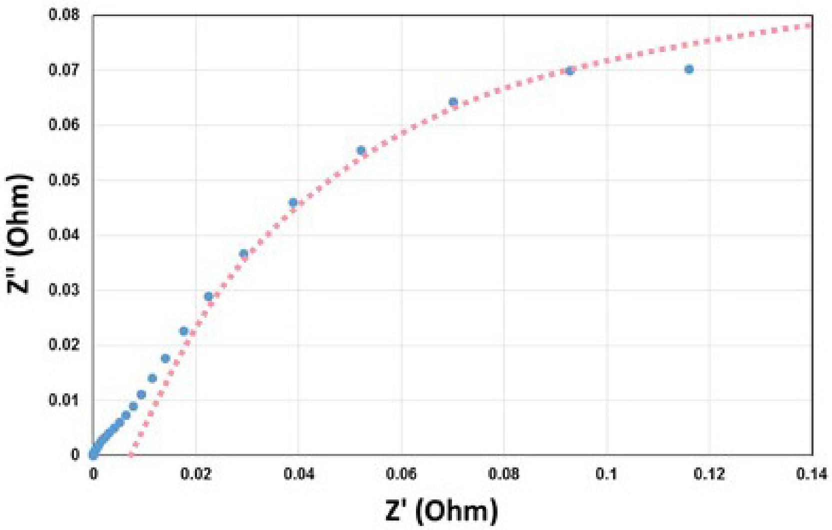

Fig. 86 Impedance plot of MoS_2

4. Future Work

Scoping and building a molecular plasmon with specific functionality and response to external stimuli is best achieved with a notional transition goal. Because of the complexity of the plasmon material synthesis, it becomes imperative to design functional response and durability around specific outcomes. This report discusses the author's strategy, built off his experience at the Republic of Korea Agency for Defense Development (ADD), for building a fuel system based upon the ability to create unique molecular systems capable of generating photonic response from external stimulations in the UV and visible frequencies coupled strongly to the synthetic capability at the US Army Research Laboratory (ARL)[*]. The diagrams of systems capable of generating energy from electromagnetic stimuli are shown in Figs. 87 and 88.

---

[*] The work outlined in this report was performed while the US Army Research Laboratory (ARL) was part of the US Army Research, Development, and Engineering Command (RDECOM). As of 31 January 2019, the organization is now part of the US Army Combat Capabilities Development Command (formerly RDECOM) and is now called CCDC Army Research Laboratory.

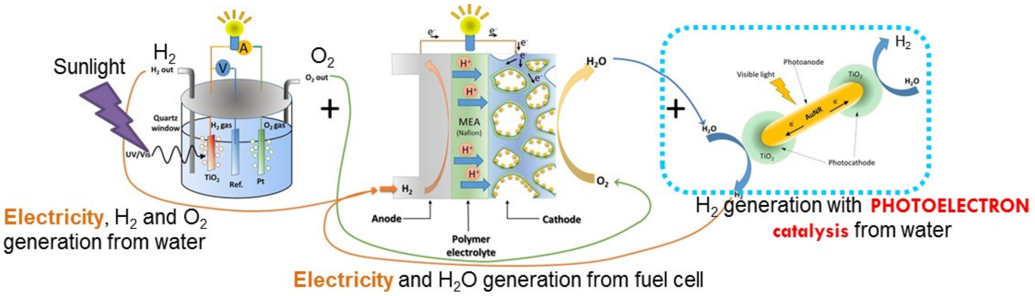

Fig. 87 Midterm goal of plasmonic reaction application for energy generation. Versatile robust electric power source from sun and water.

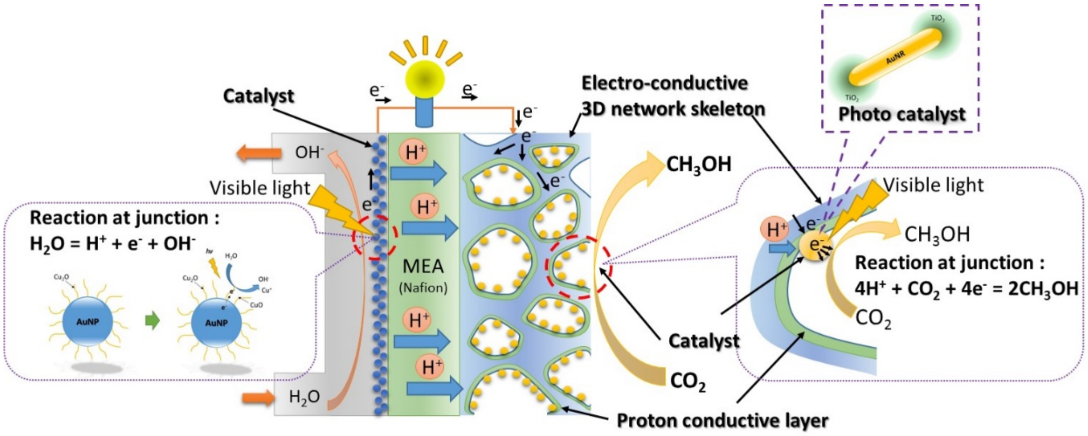

Fig. 88 Long-term goal of unit independent robust and dependable power source from sun and water (hydrocarbon synthesis with photoelectron catalyst)

Research and development of improvements in novel energy polymer electrolyte membrane fuel cell conversion requires basic and advanced research in bipolar plates for fuel cell technologies to advance fuel cell technologies toward further military applications. Developing bifunctional nonprecious catalysts for ORR and OER for polymer electrolyte membrane fuel cell and fabricating single cells utilizing the new bifunctional nonprecious electrocatalysts for evaluation and evaluation with single cell performance can be a potential collaboration project for ARL and ADD (Fig. 89).

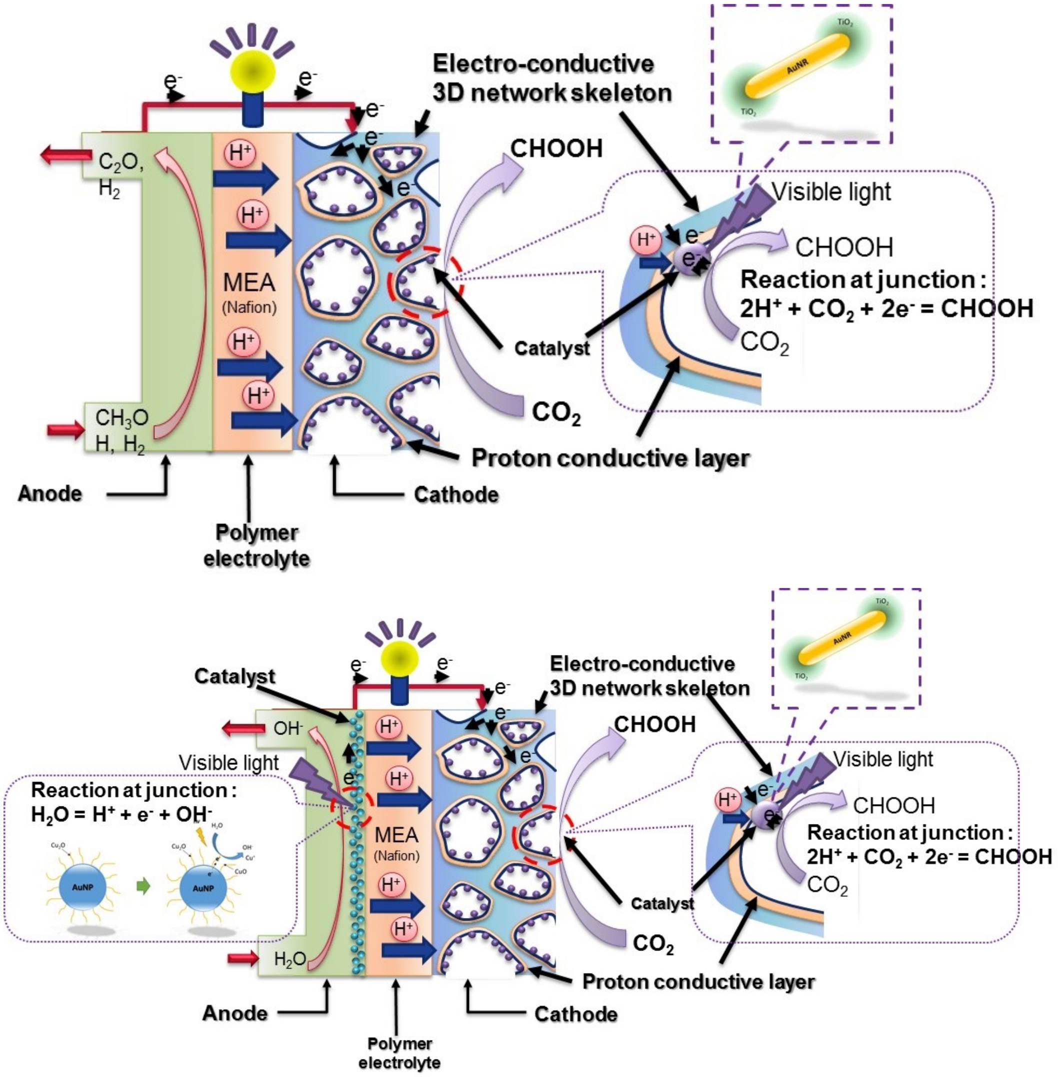

Fig. 89 Future collaboration work concepts on plasmonics for simultaneously generating electricity and hydrocarbon

5. Conclusions

The scheduled research on Plasmonically Enhanced Photocatalysts for CO_2 to Fuel Applications at the Composite and Hybrid Materials Branch of the Weapons and Materials Research Directorate (WMRD) at ARL was completed during the period from August 7, 2017 to August 5, 2018. The fulfilled topics are as follows:

- Lead execution of experiments for the design, synthesis, functionalization, and characterization of catalytic and photocatalytic nanomaterials.
- Support execution of performance testing as electrode materials in areas such as CO_2 reduction and oxygen evolution/reduction.

- Assist with the documentation of results toward technical report and/or journal publication.

During this study, the theoretically optimum multifunctional synergistic photoelectron catalyst design has been proposed and to successfully synthesize it, various kinds of experimental synthesis have been attempted. The representative results of this research are tunable as well as monodispersed AuNR synthesis, monodispersed nano-sized graphene oxide synthesis (GQD) and AuNR-TiO_2 dumbbell synthesis optimization. Unique and high-efficient photocatalysts have been designed and preliminary syntheses have been executed, such as AuNR-nGO-Cu_2O, AuNP-nGO-Cu_2O, AuNR-nGO-TiO_2 dumbbell, and AuNR-Cu_2O dumbbell. Also a one-cycle research procedure from design, synthesis, to photoelectrochemical property measurement has been set up at WMRD. Future collaboration areas have been established through a partnership agreement between ARL and ADD on plasmonic catalysts for unmanned aerial vehicle–applicable fuel cell research.

6. References

1. Li J, Griep M, Choi Y, Chu D. Photoelectrochemical overall water splitting with textured $CuBi_2O_4$ as a photocathode. Chem Commun. 2018;54:3331–3334. doi: 10.1039/c7cc09041b.
2. Ray C, Pal T. Recent advances of metal-metal oxide nanocomposites and their tailored nanostructures in numerous catalytic applications. J Mater Chem A. 2017;5:9465–9487.
3. Si Y, Cao S, Wu Z, Mi Y, Wu X, Liu X, Piao L. What is the predominant electron transfer process for Au NRs/TiO_2 nanodumbbell heterostructure under sunlight irradiation? Applied Catalysis B: Environmental. 2018;220:471–476.
4. Li H, Wang X, Wei Q, Liu X, Qian Z, Hou B. Enhanced photocathodic protection performance of Ag/graphene/TiO_2 composite for 304SS under visible light. Nanotechnology. 2017;28(22):225701. doi: 10.1088/1361-6528/aa6e5d.
5. Lang Q, Chen Y, Huang T, Yang L, Zhong S, Wu L, Chen J, Bai S. Graphene "bridge" in transferring hot electrons from plasmonic Ag nanocubes to TiO_2 nanosheets for enhanced visible light photocatalytic hydrogen evolution. Applied Catalysis B: Environmental. 2018;220:182–190.
6. Li A, Zhang P, Chang X, Cai W, Wang T, Gong J. Gold nanorod@TiO_2 yolk-shell nanostructures for visible-light-driven photocatalytic oxidation of benzyl alcohol. Small. 2015;11(16):1892–1899. doi: 10.1002/small.201403058.
7. Boyne D, Chipara A, Griep M. Transverse axis morphological control for tailored gold nanorod synthesis. RCS Advances. 2016;6:63634–63641.
8. Williams M, Boyne D, Griep M. Rapid synthesis of high purity gold nanorods via microwave irradiation. Materials Research Express. 2017;4(3):035040.
9. Wu B, Liu D, Mubeen S, Chuong TT, Moskovits M, Stucky GD. Anisotropic growth of TiO_2 onto gold nanorods for plasmon-enhanced hydrogen production from water reduction. J Am Chem Soc. 2016;138:1114–1117.
10. Lark K, Hsiao M-S, Yi Y-J, Izor S, Koerner H, Jawaid A, Vaia RA. Highly concentrated seed-mediated synthesis of monodispersed gold nanorods. ACS Appl Mater Interfaces. 2017;9:26363–26371.
11. Kim H, Moon G, Monllor-Satoca D, Park Y, Choi W. Solar photoconversion using graphene/TiO_2 composites: nanographene shell on TiO_2 core versus

TiO_2 nanoparticles on graphene sheet. The Journal of Physical Chemistry C. 2012;11(1)6:1535–1543.

12. Kim H, Kwon OS, Kim S, Choi W, Kim J-H. Harnessing low energy photons (635 nm) for the production of H_2O_2 using upconversion nanohybrid photocatalysts. Energy Environ Sci. 2016;9:1063–1073.
13. Lim D-K, Barhoumi A, Wylie RG, Reznor G, Langer RS, Kohane DS. Enhanced photothermal effect of plasmonic nanoparticles coated with reduced graphene oxide. Nano Lett. 2013;13:4075−4079.
14. Zhu S, Zhang J, Qiao C, Tang S, Li Y, Yuan W, Li B, Tian L, Liu F, Hu R, Gao H, Wei H, Zhang H, Sun H, Yang B. Strongly green-photoluminescent grapheme quantum dots for bioimaging applications. Chem Commun. 2011;47:6858–6860.
15. Khlebstov B, Khanadeev V, Yes J, Sukhorukovll G, Khlebtsov N. Overgrowth of gold nanorods by using a binary surfactant mixture. Langmuir. 2014;30(6):1696–1703.
16. Smith DK, Korgel BA. The importance of the CTAB surfactant on the colloidal seed-mediated synthesis of gold nanorods. Langmuir. 2008;24(3):644–649.
17. Choon HBN, Wai YF. Shape evolution of Cu2O nanostructures via kinetic and thermodynamic controlled growth. The Journal of Physical Chemistry B. 2006;110(42):20801–20807.
18. Lee H-S, Woo C-S, Youn B-K, Kim S-Y, Oh S-T, Sung Y-E, Lee H-I. Bandgap modulation of TiO_2 and its effect on the activity in photocatalytic oxidation of 2-isopropyl-6-methyl-4-pyrimidinol. Top Catal. 2005;35:255–260.
19. Ishizuka S, Maruyama T, Akimoto K. Thin-film deposition of Cu2O by reactive radio-frequency magnetron sputtering. Jpn J Appl Phys. 2000;39:L786–L788.
20. Zhang J, Liu J, Peng Q, Wang X, Li Y. Nearly monodisperse Cu_2O and CuO nanospheres: preparation and applications for sensitive gas sensors. Chem Mater. 2006;18:867–871.
21. Xu F, Deng M, Li G, Chen S, Wang L. Electrochemical behavior of cuprous oxide-reduced graphene oxide nanocomposites and their application in nonenzymatic hydrogen peroxide sensing. Electrochimica Acta. 2013;88:59–65.

22. Hara M, Kondo T, Komoda M, Ikeda S, Shinohara K, Tanaka A, Kondoa JN, Domen K. Cu_2O as a photocatalyst for overall water splitting under visible light irradiation. Chem Commun. 1998;3:357–358.

23. Lu B, Liu A, Wu H, Shen Q, Zhao T, Wang J. Hollow Au-Cu_2O core-shell nanoparticles with geometry-dependent optical properties as efficient plasmonic photocatalysts under visible light. Langmuir. 2016;32:3085–3094.

24. Zhang L, Jing H, Boisvert G, He JZ, Wang H. Geometry control and optical tunability of metal-cuprous oxide core-shell nanoparticles. ACS Nano. 2012;6(4):3514–3527.

25. Yu Y, Zhang L, Wang J, Yang Z, Long M, Hu N, Zhang Y. Preparation of hollow porous Cu_2O microspheres and photocatalytic activity under visible light irradiation. Nanoscale Research Letters. 2012 June;7(1):347.

26. Zhang L, Wang H. Cuprous oxide nanoshells with geometrically tunable optical properties. ACS Nano. 2011;5:3257–3267.

27. Zhang L, Wang H. Interior structural tailoring of Cu_2O shell-in-shell nanostructures through multistep Ostwald ripening. J Phys Chem C. 2011;115(38):18479–18485.

28. Kuo C-H, Hua T-E, Huang MH. Au nanocrystal-directed growth of Au-Cu_2O core-shell heterostructures with precise morphological control. J Am Chem Soc. 2009;131:17871–17878.

29. Mackay R, Giri L, Karna S, Griep M. Galvanic synthesis of hollow gold nanoshells. Aberdeen Proving Ground (MD): Army Research Laboratory (US); 2015 Jan. Report No.: ARL-TR-7219.

30. Gonçalves G, Vila M, Bdikin I, de Andres A, Emami N, Ferreira RAS, Carlos LD, Grácio J, Marques PAAP. Breakdown into nanoscale of graphene oxide: confined hot spot atomic reduction and fragmentation. Scientific Reports. 2014;4:6735. doi: 10.1038/srep06735.

31. Kumar D, Lee A, Lee T, Lim M, Lim D-K. Ultrafast and efficient transport of hot plasmonic electrons by graphene for Pt free, highly efficient visible-light responsive photocatalyst. Nano Lett. 2016;16(3):1760–1767.

32. Rajender G, Choudhury B, Giri PK. In situ decoration of plasmonic Au nanoparticles on graphene quantum dots-graphitic carbon nitride hybrid and evaluation of its visible light photocatalytic performance. Nanotechnology. 2017;28(39):395703.

33. Zhang L, Blom DA, Wang H. Au-Cu_2O core-shell nanocrystals: a hybrid metal-semiconductor heteronanostructure with geometrically tunable optical properties. Chem Mater. 2011;23:4587–4598.

34. Cassaignon S, Koelsch M, Jolivet J-P. From TiCl3 to TiO2 nanoparticles (anatase, brookite and rutile): thermohydrolysis and oxidation in aqueous medium. Journal of Physics and Chemistry of Solids. 2007;68(5):695–700.

35. Boyne D, Chipara A, Giri L, Griep M. Stabilization of gold nanorods (GNRs) in aqueous and organic environments by select surface functionalization. Aberdeen Proving Ground (MD): Army Research Laboratory (US); 2016 Jan. Report No.: ARL-TR-7581.

36. Volanti DP, Orlandi MO, Andres J, Longo E. Efficient microwave-assisted hydrothermal synthesis of CuO sea urchin-like architectures via a mesoscale self-assembly. CrystEngComm. 2010;12:1696–1699.

37. Yang C, Xiao F, Wang J, Su X. 3D flower- and 2D sheet-like CuO nanostructures: microwave-assisted synthesis and application in gas sensors. Sensors and Actuators B. 2015;207:177–185.

38. Boyne D, Orlicki J, Griep M. Plasmonic gold nanostars as optical nano-additives for injection molded polymer composites. Nanotechnology. 2017;28:405304.

39. Li T, Choi Y, Briep M. Single-particle SERS enhancement with optimized gold nanostar morphologies. Aberdeen Proving Ground (MD): Army Research Laboratory (US); 2018 June. Report No.: ARL-TR-8396.

40. Kim K, Thiyagarajan P, Ahn H-J, Kim S-I, Jang J-H. Optimization for visible light photocatalytic water splitting: gold-coated and surface-textured TiO_2 inverse opal nano-networks. Nanoscale. 2013;5(14):6254–6260. doi:10.1039/C3NR01552A.

41. Deng D, Novoselov KS, Fu Q, Zheng N, Tian Z, Bao X. Catalysis with two-dimensional materials and their heterostructures. Nature Nanotechnology. 2016;11:218–230.

42. Tahir M, Pan L, Idrees F, Zhang X, Wang L, Zou J-J, Wang L. Electrocatalytic oxygen evolution reaction for energy conversion and storage: a comprehensive review. Nano Energy. 2017;37:136–157. doi.org/10.1016/j.nanoen.2017.05.022.

List of Symbols, Abbreviations, and Acronyms

3-D	three-dimensional
AA	L-ascorbic acid
AC	alternating current
ADD	Republic of Korea Agency for Defense Development
AFM	atomic force microscopy
AgCl	silver chloride
$AgNO_3$	silver nitrate
Ag	silver
AR	aspect ratio
ARL	US Army Research Laboratory
Au	gold
AuNP	gold nanoparticle
AuNR	gold nanorod
BF-TEM	Bright field transmission electron microscopy
C	carbon
$C_{16}TAB$	hexadecyltrimethylammonium bromide
CTAB	cetyltrimethylammonium bromide
CO_2	carbon dioxide
$CuCl_2$	copper(II) chloride
Cu_2O	cuprous oxide
CYS	cysteamine
DDI	distilled deionized water
DLS	dynamic light scattering
DMF	dimethyl formamide
EFTEM	energy-filtered transmission electron microscopy

GQD	graphene quantum dot
H_2	hydrogen
HAADF	high-angle annular dark field
$HAuCl_4$	chloroauric acid
HCl	hydrochloric acid
HER	hydrogen evolution reaction
HQ	hydroquinone
ITO	indium tin oxide
LSPR	localized surface plasmon resonance
MO	molecular oxide
MoS_2	molybdenum disulfide
N_2	nitrogen
NaOL	sodium oleate
$NaBH_4$	sodium borohydride
$NaHCO_3$	sodium bicarbonate
$NH_2OH{\bullet}HCl$	hydroxylamine hydrochloride
NaOH	sodium hydroxide
nGO	nano-sized graphene oxide
NIR	near infrared
NM	noble metal
NR	nanorod
O	oxygen
OD	optical density
OER	oxygen evolution reaction
ORR	oxygen reduction reaction
PSS	polystyrene sulfonate
Pt	platinum

rGO	reduced graphene oxide
SAD	selected area diffraction
SEM	scanning electron microscopy
SDS	sodium dodecyl sulfate
SLGO	single-layer graphene oxide
Si	silicon
SPR	surface plasmon resonance
STEM	scanning transmission electron microscopy
TEM	transmission electron microscopy
$TiCl_3$	titanium trichloride
TiO_2	titanium dioxide
TSPR	transverse surface plasmon resonance
UV-Vis	ultraviolet-visible
WMRD	Weapons and Materials Research Directorate
XEDS	X-ray energy dispersive spectroscopy

1 (PDF)	DEFENSE TECHNICAL INFORMATION CTR DTIC OCA
2 (PDF)	CCDC ARL IMAL HRA RECORDS MGMT FCDD RLD CL TECH LIB
1 (PDF)	GOVT PRINTG OFC A MALHOTRA
4 (PDF)	CCDC ARL FCDD RLS DC D CHU FCDD RLW MA J SANDS FCDD RLW MC S WALCK FCDD RLW MG MH GRIEP